

Investigation of Mesopore Formation in Zeolites Catalysis using QM/MM Methods

Alec William Desmoutier

A dissertation submitted in partial fulfilment of the requirements for the degree of

Doctor of Philosophy of University College London.

Department of Chemistry
University College London

22nd November 2024

Declaration

I, Alec William Desmoutier, confirm that the work presented in this thesis is my own. Where information has been derived from other sources, I confirm that this has been indicated in the thesis.

Abstract

This thesis presents a comprehensive computational study on hydroxyl nest and mesopore formation in zeolitic frameworks through targeted T-site removals, utilizing hybrid quantum mechanics/molecular mechanics (QM/MM) calculations and density functional theory with def2-TZVP and def2-SVP basis sets. Zeolites ZSM-5, Chabazite, Faujasite, and α-Quartz were chosen for this investigation, offering a range of structural archetypes with varied channel systems and pore topologies. By selectively removing T-sites, we generated mesopores and analysed the stability, hydrogen-bonding networks, and structural changes within the framework to understand the energetics of mesopore generation. Our results indicate that the zeolites respond similarly to mesopore creation, with structural variations observed when comparing the adjacent and ring configurations. Mesopore formation is stabilized by threemembered silanol rings that form predictable and recurring hydrogen-bonded networks as Tsites are removed. Conversely, α-Quartz shows limited stable silanol ring formation, reflecting its more rigid crystalline structure leading to more hydrogen bonding between the silanols and the Si-O-Si oxygen atoms. Across all frameworks, the removal of additional T-sites beyond an optimal number was observed to introduce strain, and a less favourable energy for further pore expansion and occasionally leading to destabilized frameworks. The formation of Platinum nanoclusters are produced using Genetic Algorithms to produce results emulating ab initio techniques. These findings provide a new understanding of mesopore formation mechanisms in zeolitic structures and lay the groundwork for tailoring porous materials for catalytic applications.

Impact Statement

Research on hydroxyl nests within zeolite frameworks holds significant potential for advancing catalytic processes and material design in industrial chemistry. Hydroxyl nests defective sites populated by hydroxyl groups are shown to act as highly reactive centres that enhance the adsorption and activation of metal species, including platinum, thus improving catalytic efficiency. By promoting the formation of mesopores and increasing the overall surface area within zeolites, these hydroxyl nests facilitate the diffusion of larger molecules and improve reaction kinetics, particularly in dehydrogenation and hydrocarbon processing.

The insights gained into the controlled generation and optimization of hydroxyl nests pave the way for developing more efficient, selective, and sustainable catalysts. This work has applications in refining and petrochemical industries, where improved catalytic performance can lower energy demands and reduce by-product formation, thereby advancing greener chemical processes. Furthermore, this research establishes foundational knowledge that can be leveraged to design custom zeolite-based catalysts tailored for a variety of reactions, marking a crucial step toward innovative solutions in catalysis and materials science.

Acknowledgements

First and foremost, I would like to express my deepest gratitude to Professor Richard Catlow for his unwavering guidance, encouragement, and profound insights throughout this journey. His mentorship has been instrumental in shaping this work and my growth as a researcher.

I am immensely grateful to Dr. Scott Woodley and Dr. Alexey Sokol for their invaluable advice and support, which have greatly enriched both my research and understanding of the field. I also thank Dr. Jingcheng Guan for his vital guidance and collaboration as a postdoctoral mentor.

I extend my gratitude to Dr. Thomas Keal and Dr. You Lu for their assistance with large-scale calculations and the initial stages of my work on zeolites. I also thank Dr. Jamal Nazir, Dr. Xingfan Zhang, and Erze Gao for their invaluable support throughout this project.

I am grateful to UCL and the EPSRC for funding my research, and to the Materials Chemistry Consortium for access to the THOMAS, YOUNG, and ARCHER2 supercomputing clusters, which were critical to my work. I also acknowledge the pioneering research on TMI zeolite, which laid the groundwork for the discoveries presented in this thesis.

Finally, I am profoundly thankful to my family for their unconditional love, patience, and support. Their belief in me has been my greatest source of strength and motivation throughout this journey.

This work would not have been possible without the collective encouragement, mentorship, and inspiration provided by these extraordinary individuals and organizations.

Table of Contents

Chapter 1: Background: Zeolites and Platinum Dehydrogenation Reactions	15
1.1 Introduction	15
1.2 Zeolites	19
1.2.1 Shape Selectivity in Zeolites	31
1.3 Hydroxyl nest	34
1.4 Dehydrogenation reactions	41
1.4.1 Platinum Catalyst for Oxidative Dehydrogenation	42
1.5 Objectives	43
Chapter 2: Methodology	45
2.1 Computational Methods	45
2.2 Quantum Mechanics	46
2.2.1 Hartree-Fock Theory	49
2.2.2 Density Functional Theory	50
2.3 Implementation	53
2.3.1 Basis	53
2.3.2 Effective Core Potentials	55
2.3.3 Exchange Correlation Functionals	56
2.4 Molecular Mechanics	57
2.5 QM/MM Embedding	60
2.5.1 QM/MM Coupling	63
2.5.2 Cluster Formation	66
2.5.3 Geometry Optimisation	68
2.6 Resources	70
2.7 Justification of the Choice of Software	71
2.8 Benchmarking	71
Chapter 3: Formation of Hydroxyl nest in Zeolites	73
3.1 Introduction of Hydroxyl Nests	73
3.1.1 Computational Approach for ZSM-5	74
3.1.2 Choice of Model Cluster	75
3.2 Results and Discussion	77
3.2.1 Formation of the Hydroxyl Nest	79
3.2.2 Formation of Hydroxyl Nest in other Zeolites	79

3.3 Structure of Hydroxyl nest defects	82
3.3.1 Chabazite Triangular Hydroxyl Nest	82
3.3.2 ZSM-5 4 Membered ring Hydroxyl nest	84
3.3.3 α-quartz Double Hydrogen Bonds	86
3.4 Movement in Hydroxyl nest clusters	86
3.5 Summary and Conclusion	92
Chapter 4: Mesopore Formation	93
4.1 Introduction to Mesopore	93
4.1.1 Computational Approach for ZSM-5	94
4.2 Mesopore Formation in ZSM-5: A Computational Study	98
4.2.1 Mesopore Formation via T-site Removal in Adjacent Positions	102
4.2.2 Mesopore Formation via T-site Removal in Ring Positions	109
4.3 Mesopore Formation in Chabazite: A Computational Study	116
4.3.1 Mesopore Formation via T-site Removal in Adjacent Positions	117
4.3.2 Mesopore Formation via T-site Removal in Ring Positions	125
4.4 Mesopore Formation in Faujasite: A Computational Study	131
4.4.1 Mesopore Formation via T-site Removal in Adjacent Positions	132
4.4.2 Mesopore Formation via T-site Removal in Ring Positions	138
4.5 Mesopore Formation in α-Quartz: A Computational Perspective	143
4.5.1 Mesopore Formation via T-site Removal in Adjacent Positions	144
4.5.2 Mesopore Formation via T-site Removal in Ring Positions	151
4.6 Conclusion	157
Chapter 5: Formation of Platinum cluster with Genetic Algorithms	159
5.1 Introduction of Genetic Algorithms and Platinum clusters	159
5.1.1 Computational Approach	159
5.2 Results and Discussion	164
5.2.1 Pt ₄₋₆ clusters	165
5.2.2 Pt ₇ clusters	165
5.2.3 Pt ₁₀ clusters	166
5.3.4 Pt ₁₃ clusters	168
5.4 New Potentials for Platinum Clusters	171
5.5 Summary and Conclusion	173
Chapter 6: Summary and Conclusion	174

	6.1.1 Summary	.174
	6.1.2 Future Work	.176
Ref	erences	.177
	pendices	
A	.1 Resource Requirements	186
A	2 Computational Input files	187

List of Figures

Figure 1: Depiction of ZSM-5 and Mordenite's frameworks, with a focal point on the central channels
passing through the clusters.[2]
Figure 2: Depiction of tetrahedra SiO4/AlO4 units building up to a larger unit cell to create a full
zeolite structure. Finally depict the respective zeolite's pore structure and dimensions. [16]21
Figure 3: Depiction of the channels of the ZSM-5 zeolite. The first showing the straight channels. The
second showing the sinusoidal channels. [1]
Figure 4: Structure of channels of various zeolites. Going left to right: Faujasite, Mordenite and
Chabazite .[28-30]
Figure 5: Depicting of molecular traffic control promoting the removal of product through the straight channels in ZSM-5.[1]
Figure 6: Dialuminium process from aluminium silicates using water and acid. The hydroxyl nest
replaces the aluminium with the framework.[1]36
Figure 7: Comparison of modelling techniques based on the balance between the level of physical
detail and the computational cost. [67]
Figure 8: The QMMM embedding setup used within both Py and Tcl ChemShell. Progressing from
top to bottom: the quantum mechanical region all ab initio calculations; boundary region; the relaxed
MM ions; and the frozen MM ions. The outer most region (not displayed) contains point charges to
represent the bulk structure.[2]
Figure 9: Generation of finite cluster model for ChemShell applications. [60]67
Figure 10: Modified QM/MM cluster after the embedding setup process showing the entire QM
region utilised of ZSM-5 followed by a close up of the Hydroxyl nest defect site. Atom colour codes:
Si: yellow, O: red and H: white67
Figure 11: Benchmarking of Python ChemShell with NWCHEM calculations by varying nodes on
Archer2 machine. The cluster used to perform these calculations was a 5 atoms QM region of ZSM-5
using the def2-TZVP basis set
Figure 12: The QM/MM embedding setup: the full pure silicious ZSM-5 cluster without 3D
perspective (left) with the quantum mechanical region (right). The outermost region contains point
charges to ensure the Madelung potential in the central region of the cluster to accurately reproduce
bulk. Atoms colour codes: Si (RED) and Oxygen (GREEN). Cartesian axes directions aligned with
the crystallographic axes: X-axis (RED), Y-axis (GREEN) and Z-axis (BLUE)
Figure 13: The QM region of the full pure ZSM-5 cluster with the introduction of a single hydroxyl nest defect (left). A close-up of the hydroxyl nest defect site generated for the theoretical QM/MM calculations (right). Atoms colour codes: Si (RED), Oxygen (GREEN) and Hydrogen (WHITE)76
Figure 14: A singular hydroxyl nest defect within Chabazite zeolite after Python Chemshell
Optimization with a view from above to show the triangular hydrogen bonded ring (right). The
structural model of the hydrogen nest (left) defect (oxygen red, hydrogen white)83
Figure 15: The atomical structure of optimised ZSM-5 hydroxyl nest defect (right), and the atomical
structure of optimised α-quartz (left). (Oxygen red, hydrogen white)
Figure 16: Hydroxyl nest imagining of the transfer of proton mechanism within the nest structure of
ZMS-588
Figure 17: The energy of each image taken by the NEB calculations after optimisation to depict the
energy barrier of the process of proton transfer in hydroxyl nest in Chabazite cluster89
Figure 18: The energy of each image taken by the NEB calculations after optimisation to depict the
energy barrier of the process of proton rotation in hydroxyl nest in Chabazite cluster90
Figure 19: Figure 3.8: Plotting the average change in bond length and bond angle when undergoing
NEB calculation in ChemShell for Chabazite hydroxyl nest O-H bond when rotation around oxygen
atom

Figure 20: Figure 4.1: The atomical structure of optimised ZSM-5 hydroxyl nest defect with 2
hydroxyl nest defects surrounding a central Si(OH) ₂ to simulate the removal of 2 aluminium atoms
following the Loewenstein's rule96
Figure 21: Cumulative formation energy of ZSM-5 mesopores with respect to the number of silicon T-
sites remove to energy (eV) to remove an additional T-site. The blue line depicting the adjacent
configuration and comparing to the ring configuration in orange
Figure 22: Cumulative formation energy of ZSM-5 mesopores with respect to the number of silicon T-
sites remove to energy (eV) to remove an additional T-site. The blue line depicting the adjacent
configuration and comparing to the ring configuration in orange
Figure 23: Cumulative formation energy of ZSM-5 mesopores with respect to the number of silicon T-
sites remove to energy (eV) to remove an additional T-site. The blue line depicting the adjacent
configuration and comparing to the ring configuration in orange
Figure 24: Cumulative formation energy of α-Quartz mesopores with respect to the number of silicon
T-sites remove to energy (eV) to remove an additional T-site. The blue line depicting the adjacent
configuration and comparing to the ring configuration in orange145
Figure 25: Structural diagram of the 2 different layers of silanol groups observed in α-quartz with the
hydrogen bond lengths shown
Figure 26: Lowest energy Platinum clusters generated from GULP with the help of Genetic
Algorithms. Top left Pt ₅ , top right Pt ₆ , bottom left Pt ₇ and bottom right Pt ₁₀ 164
Figure 27: The energy difference between the lowest ranked cluster and higher Pt clusters energy
cluster. Comparing the Pt ₁₀ clusters difference between the KLMC and FHI-aims energies168
Figure 28: The energy difference between the lowest ranked cluster and higher energy Pt clusters.
Comparing the Pt ₁₃ clusters difference between the KLMC and FHI-aims energies170

List of Tables

Table 1: Defect formation energies for hydroxyl nest in sodalite produced with ab inito methods79
Table 2: The calculated reaction energies for reaction are based on the standard enthalpy of formation
of a singular hydroxyl nest by removing a silicon atom and protonating the new lose oxygens81
Table 3: The standard enthalpy of formation of ZSM-5 cluster in the adjacent configuration. ΔHf°
calculated relative to the pure silicious ZSM-5103
Table 4: The results from the optimisation of a singular hydroxyl nest in ZSM-5 showing the bond
length (Å) and bond angle (°) of each individual silanol within the mesopore
Table 5: The results from the optimisation of two adjacent hydroxyl nest in ZSM-5 showing the bond
length (Å) and bond angle (°) of each individual silanol within the mesopore
Table 6: The results from the optimisation of three adjacent hydroxyl nest in ZSM-5 showing the bond
length (Å) and bond angle (°) of each individual silanol within the mesopore
Table 7: The results from the optimisation of four adjacent hydroxyl nest in ZSM-5 showing the bond
length (Å) and bond angle (°) of each individual silanol within the mesopore
Table 8: The results from the optimisation of five adjacent hydroxyl nest in ZSM-5 showing the bond
length (Å) and bond angle (°) of each individual silanol within the mesopore
Table 9: The standard enthalpy of formation of ZSM-5 cluster in the ring configuration. $\Delta_f H^{\circ}$
calculated relative to the pure silicious ZSM-5 cluster
Table 10: The results from the optimisation of a singular hydroxyl nest in ZSM-5 showing the bond
length (Å) and bond angle (°) of each individual silanol within the mesopore
Table 11: The results from the optimisation of two hydroxyl nest in ZSM-5 in the ring configuration
showing the bond length (Å) and bond angle (°) of each individual silanol within the mesopore 111
Table 12: The results from the optimisation of three hydroxyl nest in ZSM-5 in the ring configuration
showing the bond length (Å) and bond angle (°) of each individual silanol within the mesopore 112
Table 13: The results from the optimisation of four hydroxyl nest in ZSM-5 in the ring configuration
showing the bond length (Å) and bond angle (°) of each individual silanol within the mesopore 113
Table 14: The results from the optimisation of five hydroxyl nest in ZSM-5 in the ring configuration
showing the bond length (Å) and bond angle (°) of each individual silanol within the mesopore 114
Table 15: The standard enthalpy of formation of Chabazite cluster in the adjacent configuration. ΔfH°
calculated relative to previous results
Table 16: The results from the optimisation of a singular hydroxyl nest in Chabazite showing the bond
length (Å) and bond angle (°) of each individual silanol within the mesopore
Table 17: The results from the optimisation of two adjacent hydroxyl nest in Chabazite showing the
bond length (Å) and bond angle (°) of each individual silanol within the mesopore
Table 18: The results from the optimisation of three adjacent hydroxyl nest in Chabazite showing the
bond length (Å) and bond angle (°) of each individual silanol within the mesopore
Table 19: The results from the optimisation of four adjacent hydroxyl nest in Chabazite showing the
bond length (Å) and bond angle (°) of each individual silanol within the mesopore124
Table 20: The results from the optimisation of five adjacent hydroxyl nest in Chabazite showing the
bond length (Å) and bond angle (°) of each individual silanol within the mesopore125
Table 21: The standard enthalpy of formation of Chabazite cluster in the ring configuration. ΔH_f°
calculated relative to previous results.
Table 22: The results from the optimisation of a singular hydroxyl nest in Chabazite in the ring
configuration showing the bond length (Å) and bond angle (°) of each individual silanol within the
mesopore
Table 23: The results from the optimisation of two hydroxyl nest in Chabazite in the ring
configuration showing the bond length (Å) and bond angle (°) of each individual silanol within the
mesopore

Table 24: The results from the optimisation of three hydroxyl nest in Chabazite in the ring
configuration showing the bond length (Å) and bond angle (°) of each individual silanol within the mesopore
Table 25: The results from the optimisation of four hydroxyl nest in Chabazite in the ring
configuration showing the bond length (Å) and bond angle (°) of each individual silanol within the
mesopore
Table 26: The standard enthalpy of formation of Faujasite cluster in the adjacent configuration. ΔH_f° calculated relative to previous results
Table 27: The results from the optimisation of a singular hydroxyl nest in Faujasite showing the bond length (Å) and bond angle (°) of each individual silanol within the mesopore
Table 28: The results from the optimisation of two adjacent hydroxyl nest in Faujasite showing the bond length (Å) and bond angle (°) of each individual silanol within the mesopore
Table 29: The results from the optimisation of three adjacent hydroxyl nest in Faujasite showing the
bond length (Å) and bond angle (°) of each individual silanol within the mesopore
Table 30: The results from the optimisation of four adjacent hydroxyl nest in Faujasite showing the
bond length (Å) and bond angle (°) of each individual silanol within the mesopore137
Table 31: The results from the optimisation of five adjacent hydroxyl nest in Faujasite showing the
bond length (Å) and bond angle (°) of each individual silanol within the mesopore
calculated relative to previous results
Table 33: The results from the optimisation of singular, two and three hydroxyl nests in Faujasite in the ring configuration showing the bond length (Å) and bond angle (°) of each individual silanol
within the mesopore
showing the bond length (Å) and bond angle (°) of each individual silanol within the mesopore 142
Table 35: The standard enthalpy of formation of α -Quartz cluster in the adjacent configuration. ΔHf°
calculated relative to previous results144
Table 36: The results from the optimisation of two adjacent hydroxyl nest in α-Quartz showing the
bond length (Å) and bond angle (°) of each individual silanol within the mesopore148
Table 37: The results from the optimisation of three adjacent hydroxyl nest in α -Quartz showing the
bond length (Å) and bond angle (°) of each individual silanol within the mesopore
Table 38: The results from the optimisation of four adjacent hydroxyl nest in α -Quartz showing the
bond length (Å) and bond angle (°) of each individual silanol within the mesopore
bond length (Å) and bond angle (°) of each individual silanol within the mesopore
Table 40: The standard enthalpy of formation of α -Quartz cluster in the adjacent configuration. ΔH_f°
calculated relative to previous results
Table 41: The results from the optimisation of singular, two and three hydroxyl nests in α -quartz in the
ring configuration showing the bond length (Å) and bond angle (°) of each individual silanol within
the mesopore
Table 42: The results from the optimisation of four hydroxyl nests in α -quartz in the ring configuration showing the bond length (Å) and bond angle (°) of each individual silanol within the
mesopore
Table 43: The results from the optimisation of six hydroxyl nests in α -quartz in the ring configuration
showing the bond length (Å) and bond angle (°) of each individual silanol within the mesopore 156
Table 44:Parameters of the IP used for Pt-Pt interactions provided
Table 45: Energy ranking of a single Pt atom in Pt ₇ per Pt clusters of KLMC and FHI-aims results as
well as bond length of KLMC clusters. The energy rankings are calculated with respect to the lowest energy cluster produced by KLMC
Cherry chaster produced by Kenyle

Table 46: Energy ranking of a single Pt atom in Pt ₁₀ per Pt clusters of KLMC and FHI-aims results as
well as bond length of KLMC clusters. The energy rankings are calculated with respect to the lowest
energy cluster produced by KLMC167
Table 47: Energy ranking of a single Pt atom in Pt ₁₃ clusters of KLMC and FHI-aims results as well
as bond length of KLMC clusters. The energy rankings are calculated with respect to the lowest
energy cluster produced by KLMC170
Table 48: New potentials generated by GA calculations for platinum when observing sum of squares
calculations
Table 49: The energy difference between the lowest ranked cluster and higher energy cluster.
Comparing the Pt ₁₃ clusters difference between the KLMC, AIMS and a set of new potentials
energies172

This table provides a detailed list of abbreviations used throughout the thesis, along with their full forms. These abbreviations are frequently utilized in the text and figures to succinctly represent various concepts, methodologies, and materials central to the research. By serving as a quick reference guide, the table aims to assist readers in navigating and understanding the key terms employed in the thesis.

Abbreviation	Full Term
AIMD	Ab Initio Molecular Dynamics
ALPO	Aluminophosphate molecular sieves
DFT	Density Functional Theory
GGA	Generalized Gradient Approximation
GTO	Gaussian-type orbitals
GULP	General Utility Lattice Program
HF	Hartree-Fock
HPC	High-performance computing
IR	Infrared
KLMC	Knowledge Led Master Code
LBFGS	Limited-memory Broyden-Fletcher-Goldfarb-Shanno
LDA	Local Density Approximation
MM	Molecular Mechanics
MOF	Metal-organic framework
MR	Member Ring
NMR	Nuclear Magnetic Resonance Spectroscopy
PET	Polyethylene terephthalate
Py	Python
QM	Quantum Mechanics
QM/MM	Quantum Mechanics/Molecular Mechanics
Raman	Raman Spectroscopy
SCF	Self-consistent field
STO	Slater-type orbitals
Tcl	Tool Command Language
TMI	Transition metal ions
XRD	X-ray powder diffraction

Chapter 1: Background: Zeolites and Platinum Dehydrogenation Reactions

1.1 Introduction

Zeolites are porous materials renowned for their exceptional chemical and physical properties, making them highly effective in ion exchange, gas separation and catalysis.[3] Particularly notable is their widespread application in the petrochemical industry.[4-6] The growing demand for diverse hydrocarbon chains has intensified the need to optimize catalysts for enhancing yield and accelerating the production process from finite fossil fuel resources. Consequently, there has been a rapid growth in both experimental and theoretical research aimed at unravelling the structure, dynamics and reactivity within zeolite frameworks.

This thesis will examine a range of zeolite species but with a strong focus on the characteristics of the extensively studied MFI framework zeolites, which serve as increasingly important catalysts in petrochemical processes. Our primary objective is to scrutinize the purely siliceous ZSM-5 structured silicalite, employing computational modelling techniques to elucidate the accommodation of Pt clusters within the material, particularly at defect sites, especially "hydroxyl nests." Additionally, we will explore other zeolites, including Faujasite and Sodalite for comparative analysis and we will contrast defect formation in zeolites with that in α -quartz.

The genesis of zeolite research traces back to the pioneering work of Swedish mineralogist Axel Fredrik Cronstedt [7], who in 1756 stumbled upon these unique minerals while examining volcanic rocks. Cronstedt astutely observed the significant release of steam when heating these rocks, a phenomenon attributed to water absorption into the pores and cavities of the mineral. It was during this period that zeolites began to manifest their key qualities, including adsorption, molecular sieving capabilities, and ion exchange properties. Despite their initial discovery, the field of zeolite study remained relatively small until the groundbreaking

synthesis of mordenite zeolite in the mid-1930s by Barrer [8], ushering in a new era of exploration and innovation in zeolite chemistry.

The 1960s and 1970s saw the systematic synthesis of zeolites with distinct framework structures, including the now well-known ZSM-5, developed by Mobil Research [9], which became the isomerization of xylenes in the production of para-xylene (p-xylene), a precursor for terephthalic acid and polyethylene terephthalate (PET) production [10]. Advances in hydrothermal synthesis allowed researchers to explore new framework types with varying pore sizes and shapes, broadening their applications in petrochemical and gas industries. By the 1980s, zeolites were being designed for specific industrial processes, and their role in hydrocarbon cracking and isomerization had become essential in petroleum refining [11]. The development of aluminophosphate molecular sieves (ALPOs) marked a significant extension of the field of microporous materials beyond traditional aluminosilicate-based zeolites. Researchers at Union Carbide, led by Flanigen, Wilson and their colleagues [12], pioneered this class of materials, which opened up new possibilities due to their distinct structural and chemical properties.

In the 1990s, the discovery of mesoporosity by creating larger pore networks within the microporous zeolite structures enabled access to larger molecules, significantly expanding the applicability of zeolites in catalysis. The further development of applications including ion exchange and post-synthetic modifications allowed for customized zeolite catalysts, enabling specific reactions in fine chemical and pharmaceutical industries [13, 14]. The 2000s marked a push toward creating nano zeolites and hierarchical zeolites, which combine microporous, mesoporous, and sometimes macroporous regions. These hierarchical structures enhanced molecular transport and minimized diffusion limitations. New synthesis techniques emerged to create zeolites with more complex frameworks and varying dimensionalities, which further increased the diversity of accessible zeolite materials. Tailoring the morphology and particle

size of zeolites at the nanoscale also enabled their application in environmental technologies, such as CO₂ capture and water purification. [15, 16]

The start of the 21st century has witnessed rapid growth in both computational power and the development of novel methods and algorithms. These developments in the field have changed the landscape for computational chemists, greatly expanding the range of possibilities. The exponential increase in computational capabilities, coupled with the refinement of methodologies, has propelled the field forward, enabling the generation of more accurate and reliable models.

The rise of high-performance computing (HPC) resources has played a pivotal role in catalysing these advances. The availability of robust HPC infrastructure has expedited the development of methodologies, facilitating the creation of sophisticated models that offer deeper insights into zeolite chemistry. As a result, computational chemistry has emerged as an indispensable tool in zeolite research, driving innovation and fuelling discoveries in this dynamic field.

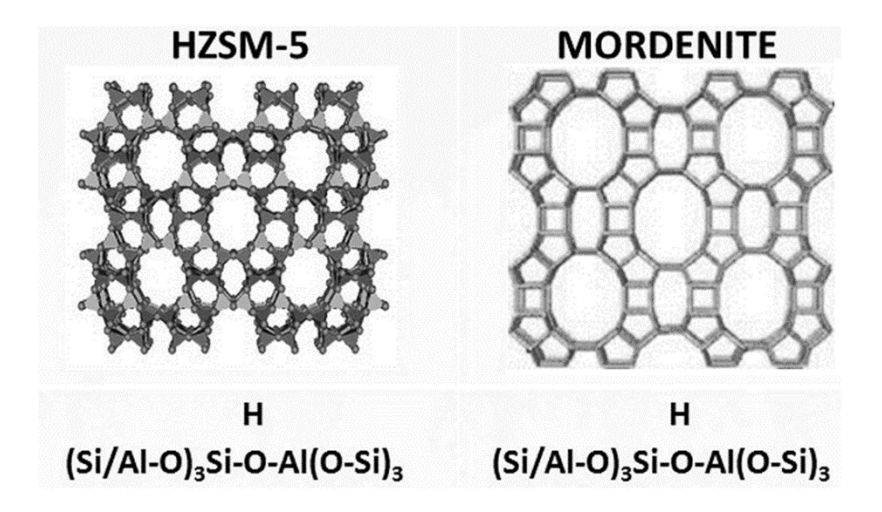


Figure 1: Depiction of ZSM-5 and Mordenite's frameworks, with a focal point on the central channels passing through the clusters.[2]

This research in this thesis was in part stimulated by the experimental investigations led by Professor Andrew Beale and his collaborators. Professor Beale's work [17] has utilised platinum (Pt) as a catalyst to facilitate the dehydrogenation of propane into propene within the pores of ZSM-5 zeolite. The study aimed to determine the specific chemical pathways traversed by the catalyst and its reagents to yield propene. Central to this investigation is the exploration of "hydroxyl nests," , *ie* hydrolysed Si vacancies, which are proposed to accommodate platinum clusters within the framework of ZSM-5 zeolite as shown in Figure 1. This integration is crucial for enabling the binding of propane molecules as they traverse the zeolite pores, ultimately leading to the formation of propene.

Moreover, the research in this thesis has helped to serve as a launchpad for the implementation of the novel Python ChemShell code [18]. This initiative aims to facilitate the development of innovative techniques and methodologies by our teams, further advancing the understanding and application of catalytic processes within zeolite frameworks.

A diverse array of quantum mechanical (QM) simulations has been conducted on zeolites, utilizing both finite cluster [19, 20] and periodic models [21, 22]. The latter have been very widely and successfully used in computational materials science but have the disadvantage when studying defects or sorption of the interaction of species in neighbouring unit cells inherent in infinitely repeating conventional QM periodic approaches. An alternative approach, employed in this thesis is the quantum mechanical/molecular mechanics (QM/MM) methodology. This approach involves embedding a QM region within an MM lattice, thereby enabling the modelling of a single defect site. The primary objective of employing the QM/MM methodology is to combine the precision of conventional QM techniques with an accurate representation of the longer-range interactions, while maintaining computational feasibility.

This technique provides a balance between accuracy and computational efficiency, allowing for investigations of zeolite properties and behaviour.

The new Python ChemShell [18], developed by a team at Daresbury Laboratory in collaboration with UCL, is designed to replicate the results obtained from the previous Tcl ChemShell [23] version concerning zeolites. However, Python ChemShell goes beyond mere replication by introducing a range of new functionalities which enhance the understanding of catalytic processes in zeolites. The stages of this endeavour reported in this thesis will involve modelling ZSM-5 zeolites with various forms of hydroxyl nest defects. This phase initially consisted of exploratory work, aimed at refining and perfecting the methodologies established using the beta version of Python ChemShell. Through iterative refinement to which I contributed, the team has advanced the capabilities of Python ChemShell, thus enabling more comprehensive and accurate simulations of zeolite behaviour and catalytic processes.

In this chapter, we next discuss the basics of zeolite science, and then discuss their chemical properties and how they interact with transition metal ions (TMI). We then discuss hydroxyl nests and their potential chemistry and location within the zeolite framework and how they are formed within the framework.

1.2 Zeolites

Zeolites are crystalline materials, with a robust structure composed of silicon, aluminium, and oxygen atoms together with hydrogen and/pr metal ions. These atoms interconnect to form a framework filled with cavities and channels, providing ample space for cations, water molecules, and other small entities. Often called "molecular sieves", zeolites owe this moniker

to their innate ability to selectively sieve molecules based on size and polarity within their natural voids and conduits. [24-26]

Over the past century, zeolites have grown in prominence, finding wide ranging applications across industries [27, 28] and in medical [29] settings alike. While traditionally sourced from natural deposits in the earth's crust, the landscape has undergone a notable shift with the advent of rapid synthetic methodologies. Today, the majority of zeolites are synthesized, both for commercial utilization and scientific investigation into their multifaceted properties.

Zeolite frameworks are denoted using a standardized three-letter code system, facilitating systematic classification and study. To date, a total of 258 distinct zeolite framework types have been identified in both natural and synthetic zeolites, with each framework uniquely classified and assigned a three-letter code by the International Zeolite Association (IZA) [30]. This rich diversity underscores the versatility and potential of zeolites in addressing a spectrum of technological, industrial, and scientific challenges.

The synthesis, structures, and properties of zeolites have unlocked a wide variety of applications, harnessing their unique attributes for processes ranging from gas separation and ion exchange [31] to catalysis [32]. The growing demand from the industrial sector to explore newly synthesized zeolites has fuelled a rapid expansion in our understanding of their properties and potential applications. Crucially, computational techniques have emerged as indispensable tools in understanding the chemistry of zeolites in modern landscape.

Zeolites are characterized by their crystalline framework structure, composed primarily of alumino-silicates, featuring a diverse array of pores and cages. These porous materials have natural or synthesized pores that permeate their extensive channels, offering significant potential for gas absorption and molecular sieving. Zeolite frameworks encompass a spectrum of dimensional complexities, ranging from one- to three-dimensional pore systems. The

micropore sizes of zeolites range from 0.3 up to 1.0 nm in the group of aluminosilicates zeolites but can be larger for other types of microporous materials that will not be discussed in this work. [33, 34]

The classification of zeolite pores typically hinges on their respective sizes, delineated as small (8 tetrahedral units), medium (10 tetrahedral units), and large (12 tetrahedral units) rings, as illustrated in Figure 2. This classification scheme provides an understanding of zeolite structures and aids in the characterization and exploration of their pore properties and applications. Zeolite surface area can be described as the total sum of both its external and internal surface areas. The first group is entirely comprised of micropores, and the latter is made up of the remaining surface area, including mesopores and macropores.[35]

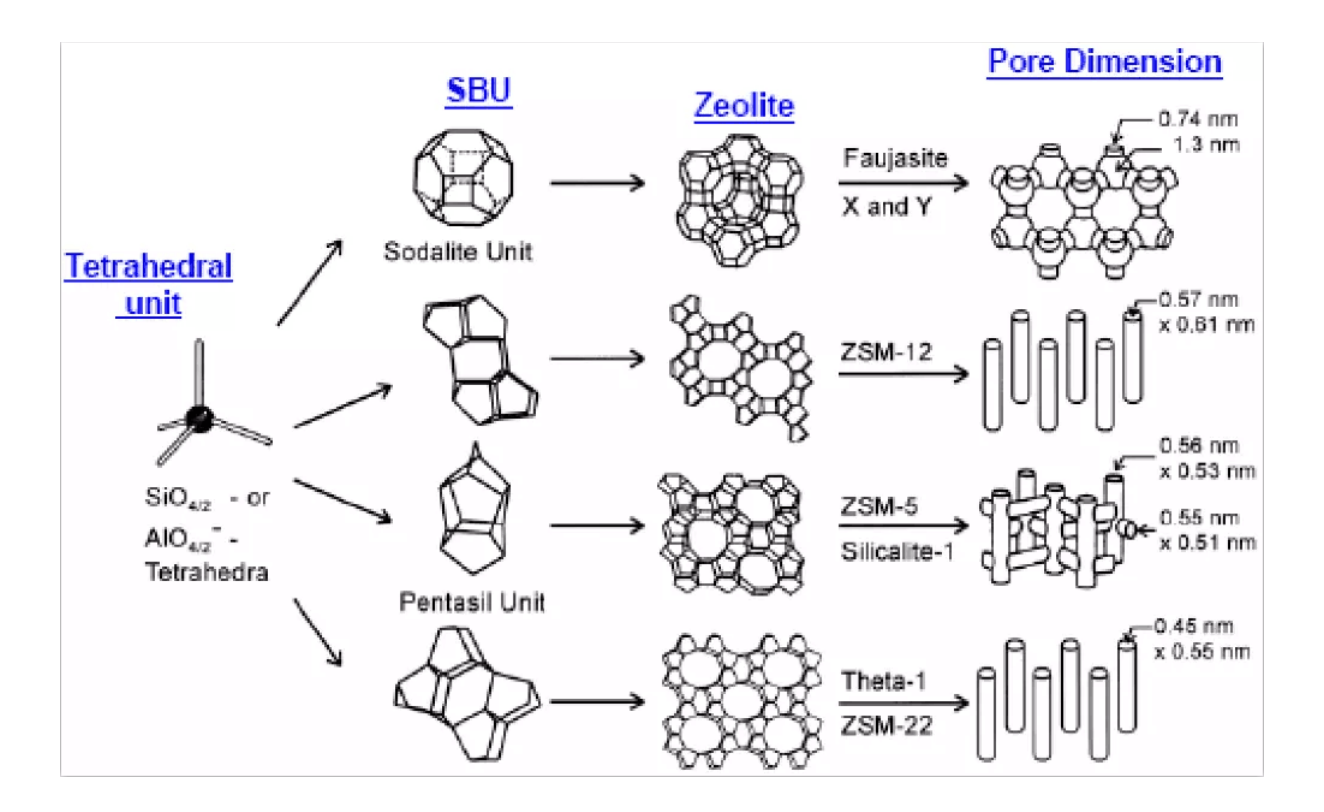


Figure 2: Depiction of tetrahedra SiO4/AlO4 units building up to a larger unit cell to create a full zeolite structure. Finally depict the respective zeolite's pore structure and dimensions. [16]

Micropores are defined as pores with diameters less than 2 nanometres. These small pores are intrinsic to the crystalline framework of zeolites, resulting in high surface areas and providing unique shape-selectivity for catalytic reactions and adsorption processes. Mesopores, with diameters ranging from 2 to 50 nanometres, can be introduced into zeolites through post-synthetic modifications such as desilication or dealumination. The presence of mesopores enhances the diffusion of larger molecules that cannot easily access the microporous network, thereby improving the efficiency and effectiveness of zeolite catalysts in reactions involving bulky reactants. Macropores, defined as pores larger than 50 nanometres, can be created through templating methods or by incorporating zeolites into a macroporous matrix. These large pores facilitate the transport of molecules within the material, reducing diffusion limitations and allowing for better mass transfer in processes such as catalysis, adsorption, and ion exchange. Understanding the distribution and integration of these pore types within zeolites is crucial for tailoring their properties for specific industrial applications, from refining petroleum to environmental remediation.[36-40]

Zeolites are remarkably versatile catalysts, owing largely to their porous framework, which possess many interaction sites for a diverse range of reactants to occur within their frameworks [41]. This inherent versatility stems from the intricate channels traversing the zeolite structure, facilitating the flow of various molecules to reach these interaction sites and introducing site selectivity. Faujasite-type zeolites, including synthetic types such as zeolite X and Y, have a three-dimensional framework with large super cages interconnected by smaller windows [42]. These super cages and the surrounding sodalite cages allow for different sites where cations can be placed. In catalytic cracking, lanthanum (La³+) ions are often introduced in FAU-type zeolites, creating stronger and more thermally stable Brønsted acid sites. This modification enhances selectivity for certain reactions, such as cracking of large hydrocarbons, by localizing

acidity and altering the pore environment. La-FAU catalysts are widely used in fluid catalytic cracking (FCC) processes to selectively crack heavy hydrocarbon molecules into lighter products.[43]

Another example of site selectivity can be found within ZSM-5 with its unique intersecting channel structure with medium-sized pores that are ideal for shape-selective catalysis. Selective desilication involves treating ZSM-5 with an alkaline solution (usually NaOH) to remove silicon atoms selectively from the framework, thereby creating additional mesopores. Desilication not only improves mass transport but can also expose specific acid sites within the framework, enhancing their accessibility and thus making them more effective for catalysis. This treatment has been shown to improve the selectivity in reactions such as methanol-to-hydrocarbon (MTH) conversions, where desilicated ZSM-5 shows increased selectivity for olefins and aromatics.[44-46]

Site selectivity plays a crucial role in catalysis, enabling the selective binding of specific atoms or molecules to particular active sites [47]. These selective sites exhibit a preference for binding with a distinct group of atoms sharing a common active group. Zeolite frameworks possess the requisite active sites that can be functionalized through impregnation with specific metal particles during the reaction process, often conducted at precise temperatures [48]. Zeolite catalysis is mainly acidic from exchanged protons or the redox from the framework of extra framework ions. [49]

Despite their crystalline nature, zeolites exhibit a propensity for containing a significant number of defects within their large lattice. These defects range from vacancies (missing atoms) to metallic impurities, further enriching the catalytic landscape of zeolites and contributing to their multifaceted reactivity. [50]

The open pores of zeolites facilitate the transfer of reactants to the internal acid or cation sites embedded within the lattice. The size of these pores serves as a natural means of sieving molecules or clusters, dictating which species can traverse through the zeolite framework. This inherent property, often referred to as "molecular sieving," was initially thought to be a distinctive characteristic exclusive to zeolites. [51]

However, recent advancements have revealed that metal-organic framework (MOF) materials also exhibit molecular sieving properties [52]. Despite this similarity, MOFs typically exhibit lower thermal and mechanical stability compared to zeolites. Thus, while MOFs offer promising alternatives in certain applications, zeolites remain unparalleled in their robustness and durability, making them indispensable materials in various catalytic and separation processes.

The screening of potential new zeolites has undergone significant advances, propelled by the proliferation of "libraries" or databases dedicated to cataloguing and categorizing various zeolite structures. These repositories serve as valuable resources for researchers seeking to explore and identify novel zeolite frameworks with tailored properties. [30]

In situ spectroscopic techniques, particularly in situ infrared (IR) [53] and optical methods [54], have been instrumental in elucidating the nature of active sites within zeolite catalysts. These techniques provide valuable insights into the mechanisms of catalytic reactions, shedding light on the intricate interplay between zeolite structure and catalytic performance.

While the capabilities of computational chemistry in elucidating zeolite chemistry have advanced significantly in recent decades [55], challenges remain, particularly in the generation of new, pre-defined zeolite structures from scratch [56]. The synthesis of previously unsynthesized zeolite frameworks is a complex endeavour that continues to be the focus of extensive research and development efforts spanning multiple years. Despite these challenges,

the progress made thus far underscores the immense potential of computational approaches in advancing our understanding of zeolite chemistry and guiding the design of novel zeolite materials.

Silicates are minerals characterized by the presence of silicon and oxygen arranged in tetrahedral structures, forming pure silica polymorphs of orthosilicate units (SiO₄₄-). These tetrahedral building blocks are intricately linked together in various patterns, typically through corner-sharing networks, to form larger clusters.[57] Orthosilicates, the most prevalent form of these clusters, exhibit strong conjugate bases of weak Ortho-silicic acid and are not stable in aqueous solutions. [58]

Silicates can manifest in other forms such as metasilicate (SiO₃₂-) and pyrosilicate (Si₂O₇₆). The corner-sharing networks of silicates give rise to infinite lattices, which serve as the foundation for the formation of larger zeolite structures. Notably, silicates demonstrate exceptional thermal stability, making them well-suited for high-temperature applications [59]. Additionally, silicates possess unique catalytic properties, further enhancing their utility in various industrial processes. [60-62]

The combination of high thermal stability and catalytic efficacy positions silicalities as one of the top five major zeolites utilized by industries worldwide. Their versatility and performance make them indispensable materials in a wide range of applications across numerous sectors.

ZSM-5, also known as Zeolite Socony Mobil–5, is an alumino-silicate zeolite distinguished by its pentasil units and MFI structure. These pentasil units, composed of interconnected SiO₄ tetrahedra, form extended chains within the zeolite framework. Subsequently, these chains interconnect to create larger sheets, giving rise to the unique structure of ZSM-5, illustrated in Figure 2.[63, 64]

The active sites within ZSM-5 exhibit strong Brønsted acidity and uniform micropores, making it exceptionally effective for acid catalysed chemical reactions and serving as selective catalysts [65]. ZSM-5 is isostructural with silicalite, with approximately 1% of its silicon sites replaced by aluminium atoms

When a silicon T-site within the zeolite framework is replaced by an aluminium atom, it introduces a negative charge on the framework. This charge imbalance disrupts the framework's charge neutrality, necessitating the introduction of compensating cations to restore equilibrium.

One of the distinguishing features of ZSM-5 is its pore structure, which combines large pores akin to those found in zeolites such as Faujasite, along with smaller pores comparable to Linde Type A and erionite. Within the ZSM-5 framework, the pentasil units form eight five-membered rings, contributing to the interconnected three-dimensional framework structure. [66]

The arrangement of linked sheets in the ZSM-5 framework gives rise to various ring and pore structures, leading to the space group Pnma and lattice constants of a = 20.1 Å, b = 19.9 Å, and c = 13.4 Å [67]. This structural organization confers unique catalytic and adsorption properties to ZSM-5, making it a highly sought-after material in industrial applications. [68-70]

MFI zeolites, including ZSM-5, exhibit three distinct sites for reactivity along a pair of channels integral to their structure. These channels play a crucial role in imparting key properties to the zeolite, including sorption, catalytic activity, and selectivity. Each channel features an elliptical opening, with the shape and dimensions varying depending on the ratio between silicon and aluminium atoms within the framework.

In the case of ZSM-5, the channel openings for the straight and sinusoidal channels measure approximately 0.54×0.56 nm² and 0.51×0.55 nm², respectively [71]. The straight channel traverses the centre of the framework in the 010 direction, while the sinusoidal channels exhibit

a zigzag-like pattern with near-circular cross-sections along the 100 directions, as depicted in

Figure 3. These distinct channel architectures contribute to the unique catalytic and adsorption

properties exhibited by ZSM-5 and other MFI zeolites, making them versatile materials in

various industrial applications. There are three key sites through in the channels of the ZSM-5

zeolite framework:

The site (I): in the straight channels, with opening of $0.51 \times 0.55 \times 0.66$ nm³.

The site (II): in the sinusoidal channels with opening of $0.54 \times 0.56 \times 0.45$ nm³.

The site (III): the intersection of the channels, with a volume of 0.9 nm3.

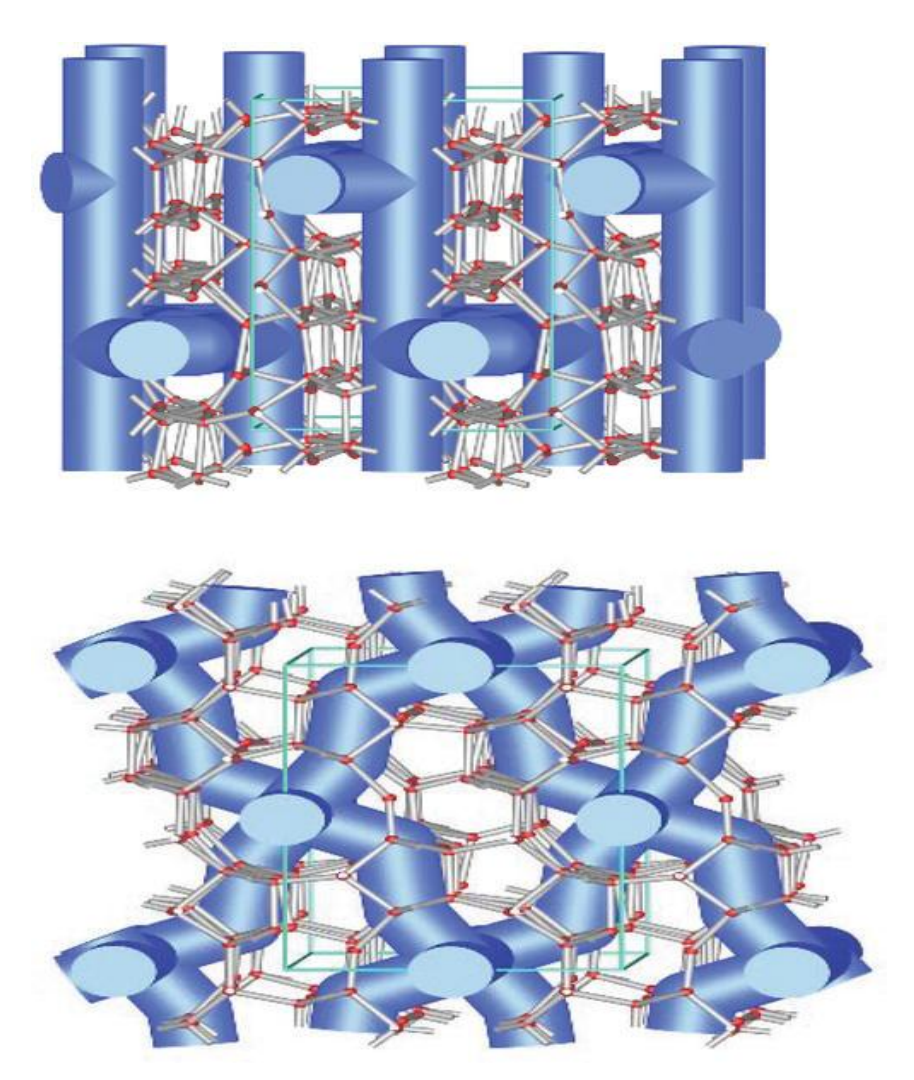


Figure 3: Depiction of the channels of the ZSM-5 zeolite. The first showing the straight channels. The second showing the sinusoidal channels. [1]

Other zeolite discussed in this thesis are Faujasite, mordenite, α -quartz and chabazite.

Chabazite (CHA) is a material that is of considerable interest as it has a wide use as a catalysis, adsorb selectively trap molecules and ion exchange properties. It has a three-dimensional framework structure composed of interconnected tetrahedra like ZSM-5. Chabazite, however, has a lower acidity compared to ZSM-5, making it suitable for reactions where milder acidic conditions are desired. Chabazite also does not have as complex system of channels compared to ZSM-5 which reduces its shape selectivity. [72, 73]

Faujasite (FAU) has a variable silica-to-alumina ratio, with the high silica material (referred to

as zeolite Y) being hydrophobic [74]. It has far large pores consisting of 12 T atoms with a

diameter of 7.4 Å compared with ZSM-5 5.5 Å with its 10 membered rings [75]. These large

pores can facilitate much larger molecules and facilitating diffusion within the zeolite structure.

Faujasite zeolites are very widely used in catalytic cracking of large hydrocarbons [76],

adsorption of bulky molecules [77], and as catalysts for other petrochemical processes. [78]

Mordenite is another key zeolite in the industrial application due to its high thermal stability

and adsorption capacity [79]. It is also commonly used for catalysis, adsorption, and ion

exchange processes [80, 81]. Mordenite exhibits moderate acidity, making it suitable for a wide

range of reactions requiring mild to moderate acidic conditions.

The structure of the channels are depicted in Figure 4 and the geometry sites through the

channels of Faujasite, mordenite, α -quartz and chabazite are as follows:

Faujasite channel: channels, with opening of $2.4 \times 2.4 \times 0.74$ nm3. [82]

Mordenite channel: channels, with opening of $1.8-2.0 \times 1.8-2.0 \times 0.7-0.8$ nm3. [83]

A-quartz channel: channels, with opening of $0.5 \times 0.5 \times 0.5$ nm³. [84]

Chabazite channel: channels, with opening of $1.0 \times 1.4 \times 0.7$ nm³. [85]

29

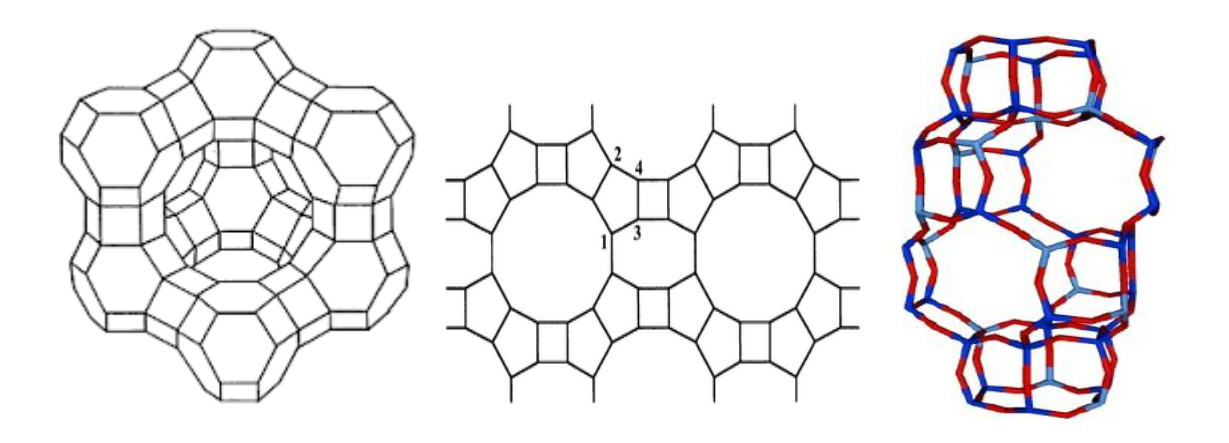


Figure 4: Structure of channels of various zeolites. Going left to right: Faujasite, Mordenite and Chabazite .[28-30]

One method of charge compensation involves the introduction of protons by adding metal ion such as Aluminium, which can bond to the framework oxygen atoms. These protons are relatively weakly bonded to the framework oxygen atoms, resulting in highly acidic sites known as Brønsted acid sites [86]. These Brønsted acid sites serve as the active sites for acidic catalysis in many petrochemical processes, facilitating numerous chemical transformations. The positioning and dispersion of aluminium (Al) atoms within zeolite frameworks are intricately linked to the arrangement of charge-compensating cations. The Si/Al ratio and the distribution of Al throughout the zeolite lattice play pivotal roles in shaping catalytic reactions. However, the type and placement of charge-compensating cations exert significant influence on the catalytic performance of zeolites [87]. Variations in the coordination environment surrounding these cations in extra framework sites can yield unique acid-base properties and heightened redox reactivity in cation-zeolite complexes. Moreover, the Si/Al ratio of the framework governs the density of cation exchange sites within zeolites, offering an additional dimension for tailoring active site specificity. These distinctive attributes underscore the potential for designing molecular catalysts exhibiting enzyme-like selectivity and activity.

Alternatively, other cations such as alkali metals, alkali earth metals, transition metals, or lanthanides can also compensate for the charge imbalance within the zeolite framework [88]. These cations may contribute to the overall catalytic activity of the zeolite and can influence the selectivity and efficiency of various chemical reactions occurring within the framework. They also enable the materials to be used in ion exchange processes – a major application of zeolites in water remediation and detergency. [89, 90]

Having introduced the structural and catalytic chemistry of zeolites, we now focus on the hydroxyl next defect which is the focus of much of this thesis.

1.2.1 Shape Selectivity in Zeolites

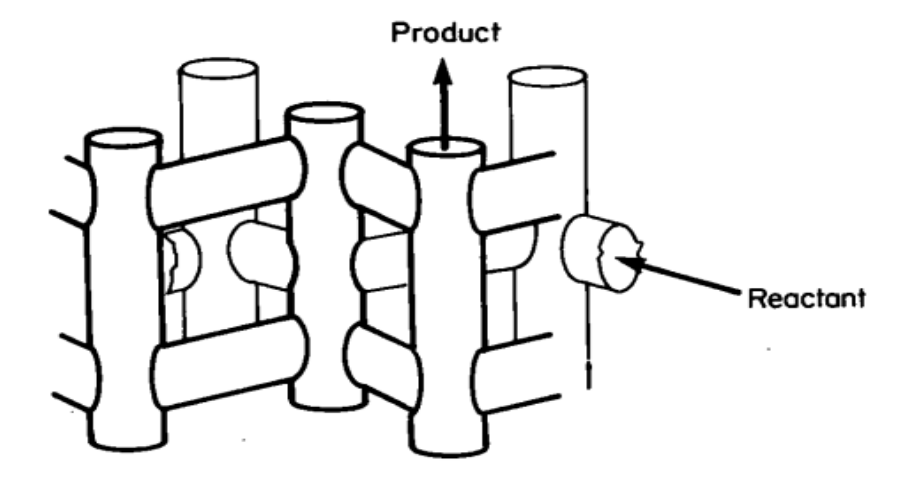
Zeolites have become indispensable in the field of heterogeneous catalysis owing to four key properties:

- 1. <u>Porous Structure</u>: Zeolites possess a highly porous structure with well-defined channels and cavities, allowing for the adsorption and diffusion of molecules. This property enables zeolites to act as molecular sieves, selectively adsorbing and separating molecules based on their size and shape. With the property of having pores of various size with a diameter smaller than 10 Å
- Shape Selectivity: The uniform pore size and shape of zeolites confer shape selectivity,
 allowing only molecules of certain sizes and shapes to access the active sites within the
 pores. This property enables zeolites to catalyse specific reactions with high precision
 and selectivity.
- 3. <u>Acidic or Basic Nature</u>: Zeolites can possess both acidic and basic sites within their framework, depending on the composition and structure. These acidic and basic sites

- play a crucial role in catalysing various chemical reactions by facilitating proton transfer, adsorption, desorption, and other surface interactions.
- 4. <u>High Surface Area</u>: Zeolites exhibit a large surface area per unit volume due to their intricate pore network. This high surface area provides ample active sites for catalytic reactions to occur, maximizing the efficiency of the catalyst.

The 1st and 2nd point are the properties that deal with the molecular sieving properties. The pore diameter of molecular sieves is intricately tied to both the number of tetrahedra forming the rings within the pores and the size of the cations contained within these structures. Given that almost all catalytic sites reside within the pore structures, the size of the pores profoundly influences the accessibility of reactant molecules and, consequently, the likelihood of reaction occurrence. Hence, smaller pores dictate the ability of reactant molecules to access catalytic sites, with the size of both the pores and starting molecules playing pivotal roles. Additionally, it's essential to consider that any resulting materials must be sufficiently small to exit the zeolite pores efficiently.

Various forms of shape selectivity arise based on factors such as pore size, reactant dimensions, product sizes, and the formation of specific transition states. Initially, selectivity manifests when only a portion of the reactant molecules is small enough to permeate the catalyst pores and reach the active sites see Figure 5. Shape-selective catalysis finds widespread application in acid-catalysed reactions like isomerization, dehydration, and cracking. Subsequently, the second stage of selectivity emerges when the products exceed the size of the initial reactants, posing challenges for diffusion out of the zeolite matrix.



Zig-zag channels = 5.4 x 5.6 Å Straight channels = 5.2 x 5.8 Å

Figure 5: Depicting of molecular traffic control promoting the removal of product through the straight channels in ZSM-5.[1]

The third form of selectivity involves constraining transition states, a challenge that arises when the resulting transition states exceed the available space within the cavities of the zeolite. To ensure the successful synthesis of products, it is crucial for transition states to remain unimpeded, facilitating the smooth diffusion of materials. This poses a significant barrier for reactions generating isomers with protruding groups, as exemplified by the conversion of meta-xylene to 1,3,5-trialkylbenzene. In such cases, the downward transition state becomes too wide for zeolites like mordenite, hindering the formation of the desired 1,3,5-isomer while allowing the formation of the 1,2,4-isomer. This blockage of transition states underscores the intricacies of shape-selective catalysis within zeolites.

The fourth approach to catalyst selectivity involves the concept of molecular traffic control, a phenomenon observed in zeolites possessing multiple pore systems. Here, reactants exhibit a preference for entering the framework via one of the pore systems, while products can diffuse out through another pore system. This strategy serves to minimize counter diffusion within the

cluster. Molecular traffic control represents a form of shape selectivity unique to zeolites with intricate pore architectures throughout the lattice, aimed at precisely enhancing reaction rates. In the case of ZSM-5, bulkier molecules tend to diffuse out through the straight pores with larger entrances, as depicted in Figure 5, illustrating the nuanced control exerted over molecular movement within these zeolitic structures.

1.3 Hydroxyl nest

The efficacy of zeolites as catalysts has been extensively documented [91-93]; however, the reactions mechanisms occurring at the active sites are often still not understood. A particular area of interest lies in understanding how metals are incorporated into zeolite structures.

As noted above, the exceptional acid catalytic properties of zeolites have been largely attributed to the presence of Brønsted acid centres. The microporous structure of zeolites not only facilitates catalytic activity but also imparts shape selectivity, thereby controlling the nature of the reactions and the resulting products. This unique characteristic of shape-selective acid catalysis has driven intensive research into the properties of Brønsted acid centres within these materials [94, 95]. Both theoretical and experimental techniques have been employed to gain deeper insights. For instance, Schroder et al. [96] utilized Mott-Littleton techniques to characterize the Al-OH centre in Zeolite Y, achieving vibrational frequency calculations of the OH group that aligned well with experimental data. Additionally, quantum mechanical methods have been extensively applied to model the behaviour of acid centres in zeolites and their interactions with small molecules, as demonstrated by the influential work of Sauer [97] and Gale et al [98]. These studies collectively enhance our understanding of the fundamental

mechanisms underlying zeolite catalysis and guide the development of more effective catalytic materials.

Current theories suggest that defects within the framework play an important role in determining the properties exhibited by zeolites including ZSM-5, although the underlying chemistry remains poorly understood. Within the zeolite community, there is a consensus regarding the formation of hydroxyl nests inside the framework. [99]

The formation of a hydroxyl nest typically arises from the loss of aluminium or silicon sites within the framework [100-103]. The resultant vacant sites are then hydrolysed, leading to the formation of four closely packed silanol groups (\equiv Si-OH), collectively known as a hydroxyl nest. The reaction involved can be represented as:

$$Si_{Si} + \frac{20_0}{} + 2H_2O \rightarrow [V_{Si}(OH)_4]$$

These theories are grounded in the seminal work of Barrer and Makki [8], wherein hydroxyl nests were proposed to be generated through the dealumination of zeolites using HCl, as illustrated by the reaction in Figure 5 as proposed by Sokol et al [36]. In other areas of mineralogy, hydroxyl nest is sometimes referred to as hydrogarnet species [104, 105]. The energy-minimized structure for this defect is close to that determined by crystallographic studies of hydrogarnet as discussed by Wright et al [106].

$$\Rightarrow_{\text{Si}} - 0 - \text{Ai} - \overline{0} - \text{Si} \leftarrow + \text{H}_{\text{y}}0^{+} + 3\text{HCI} \longrightarrow \Rightarrow_{\text{Si}} - 0 + \text{H}_{\text{H}}0 - \text{Si} \leftarrow + \text{H}_{\text{y}}0 + \text{AICI}_{\text{y}},$$

$$\Rightarrow_{\text{Si}} - 0 - \text{Ai} - \overline{0} - \text{Si} \leftarrow + \text{H}_{\text{y}}0^{+} + 3\text{HCI} \longrightarrow \Rightarrow_{\text{Si}} - 0 + \text{H}_{\text{H}}0 - \text{Si} \leftarrow + \text{H}_{\text{y}}0 + \text{AICI}_{\text{y}},$$

$$\Rightarrow_{\text{Si}} - 0 - \text{Ai} - \overline{0} - \text{Si} \leftarrow + \text{H}_{\text{y}}0^{+} + 3\text{HCI} \longrightarrow \Rightarrow_{\text{Si}} - 0 + \text{H}_{\text{H}}0 - \text{Si} \leftarrow + \text{H}_{\text{y}}0 + \text{AICI}_{\text{y}},$$

$$\Rightarrow_{\text{Si}} - 0 - \text{Ai} - \overline{0} - \text{Si} \leftarrow + \text{H}_{\text{y}}0^{+} + 3\text{HCI} \longrightarrow \Rightarrow_{\text{Si}} - 0 + \text{H}_{\text{H}}0 - \text{Si} \leftarrow + \text{H}_{\text{y}}0 + \text{AICI}_{\text{y}},$$

$$\Rightarrow_{\text{Si}} - 0 - \text{Ai} - \overline{0} - \text{Si} \leftarrow + \text{H}_{\text{y}}0^{+} + 3\text{HCI} \longrightarrow \Rightarrow_{\text{Si}} - 0 + \text{H}_{\text{H}}0 - \text{Si} \leftarrow + \text{H}_{\text{y}}0 + \text{AICI}_{\text{y}},$$

$$\Rightarrow_{\text{Si}} - 0 - \text{Ai} - \overline{0} - \text{Si} \leftarrow + \text{H}_{\text{y}}0^{+} + 3\text{HCI} \longrightarrow \Rightarrow_{\text{Si}} - 0 + \text{H}_{\text{H}}0 - \text{Si} \leftarrow + \text{H}_{\text{y}}0 + \text{AICI}_{\text{y}},$$

$$\Rightarrow_{\text{Si}} - 0 - \text{Ai} - \overline{0} - \text{Si} \leftarrow + \text{H}_{\text{y}}0 + \text{AICI}_{\text{y}},$$

$$\Rightarrow_{\text{Si}} - 0 - \text{Ai} - \overline{0} - \text{Si} \leftarrow + \text{H}_{\text{y}}0 + \text{AICI}_{\text{y}},$$

$$\Rightarrow_{\text{Si}} - 0 - \text{Ai} - \overline{0} - \text{Si} \leftarrow + \text{H}_{\text{y}}0 + \text{AICI}_{\text{y}},$$

$$\Rightarrow_{\text{Si}} - 0 - \text{Ai} - \overline{0} - \text{Si} \leftarrow + \text{H}_{\text{y}}0 + \text{AICI}_{\text{y}},$$

$$\Rightarrow_{\text{Si}} - 0 - \text{Ai} - \overline{0} - \text{Si} \leftarrow + \text{H}_{\text{y}}0 + \text{AICI}_{\text{y}},$$

$$\Rightarrow_{\text{Si}} - 0 - \text{Ai} - \overline{0} - \text{Si} \leftarrow + \text{H}_{\text{y}}0 + \text{AICI}_{\text{y}},$$

$$\Rightarrow_{\text{Si}} - 0 - \text{Ai} - \overline{0} - \text{Si} \leftarrow + \text{H}_{\text{y}}0 + \text{AICI}_{\text{y}},$$

$$\Rightarrow_{\text{Si}} - 0 - \text{Ai} - \overline{0} - \text{Si} \leftarrow + \text{H}_{\text{y}}0 + \text{AICI}_{\text{y}},$$

$$\Rightarrow_{\text{Si}} - 0 - \text{Ai} - \overline{0} - \text{Si} \leftarrow + \text{H}_{\text{y}}0 + \text{AICI}_{\text{y}},$$

$$\Rightarrow_{\text{Si}} - 0 - \text{Ai} - \overline{0} - \text{Si} \leftarrow + \text{H}_{\text{y}}0 + \text{AICI}_{\text{y}},$$

$$\Rightarrow_{\text{Si}} - 0 - \text{Ai} - \overline{0} - \text{Ai} - \overline{0} - \text{AiCI}_{\text{y}},$$

$$\Rightarrow_{\text{Si}} - 0 - \text{Ai} - \overline{0} - \text{AiCI}_{\text{y}},$$

$$\Rightarrow_{\text{Si}} - 0 - \text{Ai} - \overline{0} - \text{AiCI}_{\text{y}},$$

$$\Rightarrow_{\text{Si}} - 0 - \text{Ai} - \overline{0} - \text{AiCI}_{\text{y}},$$

$$\Rightarrow_{\text{Si}} - 0 - \text{Ai} - \overline{0} - \text{AiCI}_{\text{y}},$$

$$\Rightarrow_{\text{Si}} - 0 - \text{Ai} - \overline{0} - \text{AiCI}_{\text{y}},$$

$$\Rightarrow_{\text{Si}} - 0 - \text{Ai} - \overline{0} - \text{AiCI}_{\text{y}},$$

$$\Rightarrow_{\text{Si}} - 0 - \text{Ai} - \overline{0} - \text{AiCI}_{\text{y}},$$

$$\Rightarrow_{\text{Si}} - 0 - \text{AiCI}_{\text{y}},$$

Figure 6: Dialuminium process from aluminium silicates using water and acid. The hydroxyl nest replaces the aluminium with the framework.[1]

The reaction scheme depicted in Figure 6 represents the molecular level process in the method of successfully dealuminating zeolites, initially demonstrated by Barrer and Makki [8], who achieved dealumination on Na-clinoptilolite. Building upon this work, Kerr [101, 102] further expanded the concept, aiming to elucidate the nature of hydroxyl nests by removing all aluminium atoms to generate aluminium-free amorphous crystals of zeolite Y and ZSM-5.

Remarkably, the production of hydroxyl nests via dealumination no longer necessitates the use of acids to facilitate the removal of aluminium sites, which can be removed via the use of the steam de-alumination method [107]. and a wealth of evidence supporting the thermal and chemical stability of hydroxyl nests has accumulated over decades of research. [108]

Moreover, the new terminal silanol groups formed through the hydroxyl nest theory exhibit remarkable thermal stability, enduring temperatures of several hundred degrees Celsius without decomposition [109]. These findings underscore the robustness and enduring nature of hydroxyl nests within the zeolite framework, further establishing their significance in zeolite chemistry and catalysis.

Several characterisation techniques have been employed for the study of hydroxyl nests, of which infrared spectroscopy (IR) is one of the most commonly used. Infrared spectroscopy reveals a broad band in the range of 3200-3500 cm-1, typically indicative of the presence of OH groups following the dealumination of ZSM-5. Another valuable technique is nuclear magnetic resonance (NMR), which provides data on the Si chemical shift. NMR spectra often display two peaks assigned to Si bonded to hydroxyls: one corresponding to a tetrahedral silicon ion in the framework with only one attached OH group, and the other representing two bonded OH groups. The assignment of the NMR silanol signals presents challenges, as these signals may correspond to isolated terminal silanol groups on external surfaces, as well as to vicinal or geminal silanol pairs within the zeolite framework—often described as the zeolite's internal surface. Additionally, the interpretation of the 920–960 cm⁻¹ band is complicated by overlap with similar signals observed in heteroatom-substituted zeolites, such as Ti-silicalite, where heteroatom interactions generate comparable vibrational features. [110-118]

BET, or Brunauer-Emmett-Teller [119], is a technique used to measure the surface area of porous materials, including zeolites[120]. The BET method is based on the adsorption of gas molecules onto the surface of a solid material. When a gas (typically nitrogen) is exposed to the surface of a porous material like a zeolite at various pressures and temperatures, it forms a monolayer of adsorbed molecules. By analysing the amount of gas adsorbed at different pressures, the surface area of the material can be calculated. By fitting the experimental adsorption data to the BET equation, the specific surface area of the material can be determined. The specific surface area is defined as the total surface area per unit mass of the material and is expressed in square meters per gram (m²/g). BET analysis can also provide information about the pore size distribution of zeolites. By analysing the shape of the adsorption isotherm, researchers can infer the distribution of pore sizes within the zeolite sample, including micropores, mesopores, and macropores.

As noted earlier, over 250 distinct frameworks of zeolites have been catalogued to date, each characterized by a one-, two-, or three-dimensional pore system. The entrance of molecules into these porous structures occurs through the openings formed by oxygen atoms, known as windows, which are interconnected via a channel system facilitating access from the exterior to the internal cages. The size and structural characteristics of these windows and channels are determined by the arrangement of oxygen atoms, dictating the free diameter of the passages. Different ring configurations, denoted as nMR (where 'n' represents the number of oxygen atoms), such as 8-MR, 6-MR, and 4-MR, are prevalent in zeolite frameworks. Molecules can penetrate through the windows if their size matches or exceeds that of the rings, although zeolite structures exhibit flexibility, allowing molecules to 'squeeze' through the windows, particularly at elevated temperatures [121]. Notably, the actual free diameter is a dynamic property influenced by the inherent breathing motion of the zeolite framework.

Numerous pieces of evidence therefore support the occurrence of OH groups after the dealumination process in ZSM-5 zeolites. However, the precise mechanism underlying the formation of these OH groups remains a subject of inquiry. It is thought that the observation of the OH bond stretch may be initiated by hydrogen bonding between adjacent silanol groups within the hydroxyl nest.

Although the dealumination process increases the overall number of hydroxyl nest defects within the framework, it also leads to a decrease in the crystallinity of the zeolite [122]. This loss in crystallinity can result in the accumulation of debris such as aluminium oxide and hydroxide within the pores and possibly in the hydroxyl nest. To address this issue, acid leaching and streaming followed by annealing in an oxidizing environment are commonly employed methods. Acid leaching serves to dehydrate the affected defect areas and initiate the healing process, ultimately enhancing the overall crystallinity of the structure. [122-124]

Therefore, it is plausible that the observed IR stretch at 3200-3500 cm-1 may be attributed to the partial dehydroxylation of hydroxyl nests, underscoring the complexity of zeolite chemistry and the importance of characterisation techniques in identifying complex structural features.

The accumulation of small pieces of data has enabled the formulation of three major hypotheses to explain the existence of hydroxyl nests and their formation within zeolite frameworks. Each theory offers distinct advantages and drawbacks, yet none have emerged as definitively proven at this stage.

These hypotheses represent ongoing efforts to understand the complex processes occurring within zeolite frameworks. Continued research and experimentation are essential to further elucidate the mechanisms underlying the formation of hydroxyl nests and their significance in zeolite catalysis and materials science. The theories are as follows [125-132]:

- 1. The first hypothesis proposes that the generation of migrates leads to a rearrangement within the lattice structure of zeolites. According to this theory, new migrates are created when silicon atoms are removed by hydroxide at high temperatures within the channels of the zeolite. This mechanism assumes that the migrates directly influence the cluster, potentially affecting external factors such as the surface, mesopores, or amorphized areas of the zeolite crystal. While this theory effectively explains the production of hydroxyl nests, it fails to account for the reverse reaction. Specifically, the formation of hydroxyl nests is reversible when water passes through the mesopores, rendering the theory applicable only to one-way reactions. This limitation poses a significant challenge to the comprehensiveness and applicability of the first theory in explaining the dynamics of hydroxyl nest formation within zeolite frameworks.
- 2. The second hypothesis revolves around the study of bridging atoms and suggests that silicon/aluminium vacancies quickly form an oxide bridge (Si-O-Si) over the hydroxyl

nest to maintain the crystallinity of the cluster. According to this theory, the bridging silicon atoms would occupy positions between the first and second coordination shells. However, a major challenge with this theory arises from the significant energy requirement for the formation of the oxide bridges between the first and second coordination shells of silicon. The distance between these shells is too great to allow for the reaction to occur feasibly within the framework. Consequently, computational attempts to form these bridging atoms have been unsuccessful, as setting up the bridges during modelling results in the lattice contracting, causing the atoms to break apart rather than form stable bridges. The strain induced on the system during these computational simulations leads to the breaking of chemical bonds rather than the formation of the required bridging atoms. These computational results therefore cast doubts on the feasibility of the second hypothesis in explaining the formation of hydroxyl nests within zeolite frameworks.

3. The final hypothesis proposes that hydroxyl nests do not appear as single defects but rather through the aggregation of multiple defects, leading to the formation of larger pores within the zeolite framework. According to this hypothesis, the removal of a T-site initiates the removal of several adjacent Si sites, resulting in the creation of large pores. These newly formed large pores can accommodate large metallic clusters migrating through the zeolitic channels, providing surfaces for catalytic reactions. Furthermore, these pores lead to the formation of many secondary mesopores observed in various zeolites [133]. However, a challenge with this proposal lies in explaining the phenomenon observed when hydroxyl nests are rehydrated and reappear. This hypothesis, which this computational model aims to replicate, does, however, provide a framework for understanding the complex processes involved in the formation and reformation of hydroxyl nests within zeolite frameworks. By

simulating these processes computationally, we can gain insights into the underlying mechanisms driving the formation, stability, and reactivity of hydroxyl nests.

1.4 Dehydrogenation reactions

This field traces its origins to research on heterogeneous systems. Notably, in 1973, Burnett and Hughes [134] demonstrated that butane could be converted into both lower and higher alkanes using a combination of a dehydrogenation catalyst (platinum on alumina) and an olefin metathesis catalyst (tungsten oxide on silica). Selective dehydrogenative activation of alkanes poses a significant challenge due to the initial requirement of C–H activation in an inherently unreactive substrate to interact with metal species in the catalytic cycle. Once an alkene is formed, the alkane metathesis reaction efficiently rearranges alkylidene groups, resulting in the production of higher and lower hydrocarbons. [134]

The mechanism of dehydrogenative activation via homogeneous transition-metal complexes varies significantly depending on the substrate, catalyst, and reaction conditions [135]. The two extruded hydrogen atoms can be transferred to the metal complex or directly to a hydrogen acceptor. Stepwise mechanisms typically involve two components: the association of the substrate with the catalyst, followed by the cleavage of a C–H bond. For alkanes, alcohols, or amines, this requires the substrate to first coordinate to a transition-metal complex, which often necessitates the direct activation of a C–H bond or, in the case of alcohols and amines, an O–H or N–H bond. Binding of alcohol or amine to the metal catalyst is usually followed by deprotonation. The resulting metal alkoxide or amine complex then undergoes β C–H bond cleavage, forming a metal hydride and a dehydrogenated organic species.[17, 135-138]

1.4.1 Platinum Catalyst for Oxidative Dehydrogenation

The study of propane dehydrogenation has become an area of significant industrial interest, driven by the increasing demand for propene. Propane dehydrogenation is an endothermic reaction that requires high temperatures to achieve satisfactory propene yields [139, 140]. However, at elevated temperatures, undesired side reactions such as thermal cracking become predominant, breaking propane into smaller alkane fragments and thereby reducing the yield of propene. This challenge has motivated ongoing research into the development of catalysts that can minimize propane cracking while enhancing selectivity for propene formation.

Platinum-based catalysts are among the most promising in this regard, as they offer high activity, selectivity, and stability. However, platinum catalysts suffer from the drawback of deactivation over time due to the accumulation of carbon deposits (coke) on the catalyst surface[141, 142]. The incorporation of platinum into HZSM-5 zeolite has shown promise in mitigating coke formation during propane dehydrogenation. Grasselli and co-workers [143] demonstrated that a Pt–Sn–ZSM-5 catalyst achieved a 25% propene yield at 550 °C, close to the equilibrium yield. Their experimental results indicate that the platinum dispersion (DH₂) on this catalyst is 31.7%, as determined by hydrogen chemisorption, with a measured carbon deposition of 5.3%, according to thermogravimetric analysis. X-ray powder diffraction (XRD) patterns of Pt–ZSM-5 confirmed that the original ZSM-5 structure remains intact, suggesting that platinum doping does not significantly disrupt the zeolite framework.

Research by Lin et al. [144] has further shown that platinum on the ZSM-5 surface can form two distinct active species, depending on temperature. The first species is predominant at lower temperatures, facilitating H₂ adsorption, while the second species becomes more active at higher temperatures, enabling increased H₂ adsorption. This temperature-dependent behaviour

implies that hydrogen adsorption and desorption on platinum can be tuned by adjusting reaction conditions. The high desorption of hydrogen at elevated temperatures has been attributed to several factors: hydrogen spillover, strong hydrogen adsorption sites, and the formation of platinum–hydrogen species. These mechanisms collectively contribute to the efficient use of hydrogen in the dehydrogenation process, though they also require careful control to optimize catalytic performance. [145]

1.5 Objectives

Our study aims to firstly demonstrate the effectiveness of the new QM/MM embedding approach using the recently developed Python ChemShell. Validating the capability to replicate results obtained with the previous Tcl ChemShell is essential for confirming the accuracy of Python ChemShell. QM/MM embedding has established itself as a reliable and highly accurate tool for understanding zeolitic properties, progressively becoming a staple in the computational scientific community over the last few decades. Despite the inherent costliness associated with ChemShell, continual advances in computational capabilities and the availability of third-party modules have solidified its position as a widely accepted standard for modelling. Our objective is to conduct several case studies on zeolites, including ZSM-5, comparing results obtained from identical clusters using both versions of the software. This project aims to showcase the viability of the new ChemShell version and enhance the accessibility of ChemShell, as Python offers a more user-friendly programming language compared to its predecessor. The goal is to achieve identical results for both single-point and optimization calculations on zeolites, ensuring the correct implementation of ChemShell and associated data.

The second stage of the project requires the implementation of new vibrational techniques implemented into ChemShell. The ability to produce accurate Infra-red and Raman calculations

for the hydroxyl nest inside various zeolitic clusters to observe the similarity between new theoretical data and experimental data.

In the third stage of our study, we will generate a large ZSM-5 cluster and optimize it with a substantial QM region. Subsequently, we will introduce the hydroxyl nest defect, as well as the concept that this hydroxyl nest will grow from an original defect site to form larger mesopores. Hydroxyl nest and mesopore formation in other zeolites, ie chabazite and faujasite as well as α quartz will also be investigated. These calculations will be followed by calculations to produce platinum nanoclusters using the GULP method. The platinum cluster will be incorporated into the ZSM-5 framework enabling us to relate to experimental results conducted by Professor Andrew Beale, specifically the production of propene from propane using platinum-doped zeolite.

Chapter 2: Methodology

2.1 Computational Methods

The majority of the work presented here has made use of a hybrid quantum mechanical-molecular mechanical (QM/MM) methodology implemented within the Python ChemShell code. In the ever-evolving landscape of computational chemistry, the accurate representation of complex molecular systems presents a formidable challenge. The advent of Quantum Mechanics/Molecular Mechanics (QM/MM) methodologies has greatly extended our ability to model chemical processes, offering a synergistic blend of high-level quantum mechanical precision and computational efficiency. At the forefront of this computational frontier stands ChemShell, a powerful and versatile framework designed to orchestrate advanced hybrid calculations, seamlessly combining Quantum Mechanics (QM) and Molecular Mechanics (MM) methods. [146, 147]

ChemShell's strength lies in its adept handling of Hybrid QM/MM calculations, wherein the quantum mechanical treatment is applied selectively to a targeted region of interest within a larger molecular environment. This approach enables a nuanced examination of chemical phenomena, allowing for detailed insights into electronic structure changes, reaction mechanisms, and energetics, all while maintaining computational efficiency offered by MM techniques.[148-150]

The various aspects of ChemShell shall be described in this chapter and we shall examine the processes employed, providing an overview of the specific methods key to the undertaken work, with a further discussion about the importance of the combination of both techniques giving rise to the powerful Python and Tool Command Language (Tcl) ChemShell software.[18, 151]

2.2 Quantum Mechanics

Quantum mechanics is a fundamental theory that describes the behaviour of matter and energy at the smallest scales, typically at the level of atoms and subatomic particles. In the context of computational chemistry and tools like ChemShell, quantum mechanics plays a crucial role in understanding and predicting the electronic structure of molecules and solids. The main purpose of the QM calculations for electronic structure is to solve the time independent Schrödinger equation:

$$\widehat{H}\psi(\mathbf{r},\mathbf{R}) = E\psi(\mathbf{r},\mathbf{R})$$

where E is the energy of the system and \widehat{H} is the Hamiltonian operator acting on the unknown wavefunction ψ which describes electrons and nuclei at coordinates \mathbf{r} and \mathbf{R} , respectively. For a single particle, the Hamiltonian can be broken down into kinetic and potential energy components to give:

$$\left\{-\frac{\hbar^2}{2m}\nabla^2 + V\right\}\psi(\mathbf{r}) = E\psi(\mathbf{r}).$$

The symbol \hbar denotes the reduced Planck constant, defined as $\hbar = h / (2\pi)$, a fundamental constant in quantum mechanics with an approximate value of $1.054571 \cdot 10^{-34}$ J s. The constant m represents the particle's mass, and ∇^2 refers to the Laplacian operator, also recognized as the Laplace operator. A more practical representation, which is readily applicable to real many-particle systems, involves expressing the Hamiltonian in relation to the component interactions it characterizes:

$$\widehat{H} = \widehat{T}_{e} + \widehat{T}_{n} + \widehat{V}_{ee} + \widehat{V}_{nn} + \widehat{V}_{ne}.$$

 \hat{T}_e and \hat{T}_n , the kinetic energies of the electrons and nuclei are defined with respect to the total number of electrons N with mass m_e and the total number of nuclei M with respective masses M_i , as:

$$\widehat{T}_e = -\sum_{i}^{N} \frac{\hbar^2}{2m_e} \nabla^2(\mathbf{r}_i),$$

$$\hat{T}_n = -\sum_{i}^{M} \frac{\hbar^2}{2M_i} \nabla^2(\mathbf{R}_i).$$

 \hat{V}_{ee} and \hat{V}_{nn} describe the pairwise contributions of Coulombic electron-electron and nucleus-nucleus interactions respectively:

$$\hat{V}_{ee} = \sum_{i}^{N} \sum_{j>i}^{N} \frac{e^2}{4\pi\epsilon_0 |r_i - r_j|'}$$

$$\hat{V}_{nn} = \sum_{i}^{M} \sum_{j>i}^{M} \frac{Z_i Z_j e^2}{4\pi\epsilon_0 \left| R_i - R_j \right|};$$

 \hat{V}_{ne} represents the electron-nucleus interactions, and is defined as:

$$\hat{V}_{ne} = \sum_{i}^{M} \sum_{j}^{N} \frac{Z_{i}e^{2}}{4\pi\epsilon_{0} |R_{i} - r_{j}|}$$

where e denotes the electron charge, Z_i is the atomic number of nucleus i and the $^1/_{4\pi\epsilon_0} \approx 8.987552 \cdot 10^9 \, \text{N} \cdot \text{m}^2 \cdot \text{C}^{-2}$ pre-factor is the conventional SI Coulomb constant.

The solution of the exact Schrödinger equation poses a formidable challenge, and can only be solved exactly for one electron systems. Consequently, computational calculations necessitate the application of approximations, requiring the problem to be reformulated into a set of solvable equations. One pivotal initial step is the Born-Oppenheimer (BO) approximation, grounded in the assumption that the motion of atomic nuclei and electrons can be treated independently, primarily due to the significant disparities in their respective masses. The Born-Oppenheimer approximation serves as a crucial simplification, allowing for a substantial reduction in the computational time required for calculating molecular wavefunctions. Within this framework, the total energy of a system is treated as the sum of electron and nuclear energies. The electrons' energy is elegantly described as a function of kinetic and potential energies, influenced by the electrostatic field of the nuclear system. Simultaneously, at the classical level of theory, the nuclear energy arises from the electrostatic repulsion between nuclei. This strategic use of approximations not only facilitates computational tractability but also provides a rational and effective means to dissect and comprehend the complex interplay of electronic and nuclear components within molecular systems.

Upon eliminating nuclear motion from the Schrödinger equation, the challenge persists due to the complexity inherent in addressing an *N*-body problem. To overcome these difficulties, the Hartree approximation is applied to the calculation. This approximation represents the wavefunction of the entire electronic system as a product of individual single-particle wavefunctions. In this representation, each electron is characterized not by its individual potential but by an average potential generated by its neighbouring electrons. This approach simplifies the treatment of electron-electron interactions, facilitating a more manageable description of the quantum system.

2.2.1 Hartree-Fock Theory

The Hartree-Fock approach is built upon Hartree theory by introducing the effects of electron spin to a system to describe its behaviour more closely resembling experimental results. To implement the Hartree-Fock method for a practical system, it becomes imperative to introduce a finite set of basis functions that effectively capture the spatial distribution of each particle's coordinates. This set, denoted as k spatial functions, gives rise to 2k spin orbitals. The term "spin orbitals" signifies the quantum states associated with the electron's spin degree of freedom, with half allocated to each of the opposing electron spins, conventionally labelled as α and β .

During an actual calculation, these basis functions are precisely defined and form an integral part of what is known as a basis set. This basis set constitutes a crucial component of the computational framework, providing the necessary foundation to describe the spatial characteristics of electrons and facilitate the practical application of the Hartree-Fock method to real-world systems. As the number of spin orbitals increases, the solution to the Hartree-Fock equation converges toward the Hartree-Fock limit, an ideal state akin to utilizing an infinitely large basis set. This limit serves as a theoretical benchmark, but deviations from the exact solution to the Schrödinger equation persist due to the inherent approximations of the mean-field treatment applied to single-particle wavefunctions. This discrepancy is known as the correlation and the difference in the respective energy as the correlation energy. The correlation energy reflects the effects of electron-electron interactions beyond the simplified mean-field description incorporated in the Hartree-Fock method. To capture these correlation effects more accurately, one must resort to computationally demanding methods, and therefore not undertaken for this thesis. The alternative, although loses some of the accuracy, is density functional theory (DFT). DFT offers a simpler computational strategy. It becomes an appealing

compromise for addressing electron correlation effects in a more computationally efficient manner compared to the more rigorous but demanding methods not explored in this context.

2.2.2 Density Functional Theory

Density Functional Theory (DFT) has emerged as one of the most widely used computational methods for investigating the electronic structure of materials and molecules. Unlike wavefunction-based approaches, such as Hartree-Fock (HF) or post-HF methods, DFT relies on the electron density as the fundamental variable. This reformulation is based on the Hohenberg-Kohn theorems, which establish that the ground-state energy of a many-electron system is a unique functional of the electron density and that the true ground-state density minimizes this energy functional. Despite its success, the accuracy of DFT calculations depends critically on the choice of the exchange-correlation (XC) functional, which incorporates quantum many-body effects. This chapter provides an overview of DFT, details the XC functional, and discusses the various approximations used to model exchange and correlation effects, culminating in hybrid functionals that incorporate exact exchange.

In practical implementations, DFT is formulated within the Kohn-Sham (KS) framework, where a system of interacting electrons is mapped onto a system of non-interacting electrons moving in an effective potential. The total energy functional in KS-DFT is given by:

$$E[\rho] = T_s[\rho] + E_{ext}[\rho] + E_{Hartree}[\rho] + E_{XC}[\rho]$$

where $T_s[\rho]$ represents the kinetic energy of the non-interacting system, $E_{ext}[\rho]$ accounts for the external potential due to nuclei, $E_{Hartree}[\rho]$ describes the classical Coulomb repulsion, and $E_{XC}[\rho]$ is the exchange-correlation functional, which includes all many-body effects beyond classical electrostatics. Since $T_s[\rho]$ is known for a non-interacting system and the Hartree energy is straightforward to compute, the accuracy of a DFT calculation relies on the approximation used for $E_{XC}[\rho]$, which is not known exactly.

DFT is rooted in the premise that the properties of a system, including its ground-state wavefunction ψ_0 , can be derived directly from the spatially dependent electron density $\rho(r)$ characterizing the ground state. This relationship can be expressed explicitly as:

$$\psi_0 = \psi[\rho(r)].$$

At the core of DFT is the Hohenberg-Kohn theorem, which establishes that the ground-state electronic density uniquely determines the external potential of a system. The key challenge in DFT is the generation of reasonable representations for the electron exchange and correlation contributions.

The exchange-correlation functional, $E_{XC}[\rho]$, captures two essential quantum mechanical effects. The exchange energy originates from the antisymmetry of the electronic wavefunction, enforcing the Pauli exclusion principle, which leads to a lowering of energy due to Fermi correlations. The correlation energy accounts for additional electron-electron interactions beyond mean-field approximations, including dynamic correlation effects that influence electron localization. Since the exact form of $E_{XC}[\rho]$ is unknown, various approximations have been developed to model it.

The Local Density Approximation assumes that the exchange-correlation energy at each point in space depends only on the local electron density, as in a uniform electron gas:

$$E_{XC}^{LDA}[\rho] = \int p(\mathbf{r})\epsilon_{XC}(\rho)d\mathbf{r}$$

LDA provides reasonable accuracy for systems with slowly varying electron densities, such as bulk metals, but it struggles with molecular systems, surfaces, and strongly correlated materials due to its overbinding tendencies. LDA tends to favor electron densities that are more diffuse than the exact result, resulting in overestimated binding energies, underestimated phonon frequencies and elastic constants, and inadequate representations of band gaps. Consequently, predictions regarding the metallic, semiconducting, or insulating character of materials may fall short of accuracy.

To improve upon LDA, Generalized Gradient Approximation (GGA) functionals incorporate the gradient of the electron density, leading to functionals of the form:

$$E_{XC}^{GGA}[\rho] = \int f(\rho, \nabla \rho) d\mathbf{r}$$

Among the most commonly used GGA functionals, Perdew-Burke-Ernzerhof (PBE) is widely applied due to its balance between accuracy and efficiency. Another well-known functional is Becke-Lee-Yang-Parr (BLYP), which is frequently used in molecular simulations. While GGA improves chemical accuracy compared to LDA, it still suffers from self-interaction errors and underestimates band gaps. Additionally, DFT methods relying on LDA and GGA tend to favor solutions where electrons are artificially delocalized due to self-interaction errors, complicating the accurate representation of localized electronic states in materials.

Hybrid functionals incorporate a fraction of exact Hartree-Fock (HF) exchange to mitigate self-interaction errors:

$$E_{XC}^{Hybrid} = aE_X^{HF} + (1 - a)E_X^{DFT} + E_C^{DFT}$$

where a is a mixing parameter determined empirically or by fitting to experimental data. Some of the most commonly used hybrid functionals include Becke, 3-parameter, Lee-Yang-Parr (B3LYP), which is frequently used in computational chemistry, and PBE0, which is derived from PBE-GGA and improves band gap predictions. Another important hybrid functional is

the Heyd-Scuseria-Ernzerhof (HSE) functional, which is particularly useful for solid-state applications. A limitation of DFT in capturing dispersion forces is the inherent inability to accurately capture dispersion forces. To address this, a corrective energy term, typically a function of interatomic distances, is often introduced. While practical, this approach underscores the need for supplemental methods to account for these critical interactions.

2.3 Implementation

In quantum mechanical calculations, vital information is required to define atoms in the simulations. This dataset often comprises a basis set, effective core potential and the choice of exchange-correlation functional. These variables may alter the results and predictions of the DFT calculations. Each dataset has been pre-optimized for a specific group of target chemical species, selected based on the availability of high-quality experimental data for validation purposes and their capacity to capture a broad spectrum of chemical behaviour in electronic structure calculations.

2.3.1 Basis

In the context of quantum chemistry, a basis set is a set of functions used to represent the wavefunction of electrons in a molecule or solid [152]. The wavefunction is a mathematical function that describes the behaviour of electrons in the quantum mechanical framework by using a collection of functions that are linearly combined to produce molecular orbitals. The goal is to generate an approximation of the molecular orbitals as a linear combination of simpler functions that are known as basic functions. There are three distinct types of basis functions that are commonly utilized: Slater-type orbitals (STO), Gaussian-type orbitals (GTO), and

plane wave. STO are based on the solutions to the hydrogen atoms Schrödinger equation and provide a more accurate representation of electron behaviour compared to Gaussian-type orbitals but their integrals are more difficult to calculate. In hybrid QM/MM calculations, the choice of an appropriate basis set is crucial for accurately representing the electronic structure of the quantum mechanical region in a system of interest. All calculations in this thesis are performed using atom-centred GTO basis sets that excel in achieving this objective due to the application of the Gaussian Product Theorem. This theorem articulates that the multiplication of two Gaussian functions, centred at distinct points, results in a one new Gaussian positioned at a third point on the axis that connects them. The strategic utilization of the Gaussian Product Theorem yields a notable enhancement in computational efficiency when contrasted with calculations employing an equivalent quantity of Slater functions. The exploitation of this theorem facilitates a more expedient and resource-efficient approach, thereby underscoring the advantages of Gaussian-type orbital basis sets in quantum chemical calculations. Cartesian Gaussian functions have the general form:

$$\varphi^{GF}(r) = Nx^k y^l z^m e^{-\alpha r^2}$$

N is a normalisation factor and α is the orbital exponent, and x, y and z are the Cartesian coordinates of the Gaussian centre. The main problem with GTO basis set is that it requires multiple functions to be combined to reproduce the better results acquired from STO. Def2-TZVP (Triple-zeta valence polarization) [153] and def2-SVP (Split valence polarisation) [153] are the two primary basis sets utilized in this thesis. A dual basis set setup was implemented with the inner QM1 region treated with def2-TZVP while the outer QM2 region described using def2-SVP.

2.3.2 Effective Core Potentials

Effective Core Potentials (ECPs) [152] represent an advanced computational technique employed to streamline electronic structure calculations. ECPs are particularly beneficial in mitigating the computational demands associated with accurately modelling the behaviour of inner-core electrons in atoms. The fundamental concept underlying ECPs involves the replacement of the inner-core electrons, which are tightly bound and less involved in chemical interactions, with a simplified effective potential. This potential aims to encapsulate the influence of the inner-core electrons on the outer-shell electrons, allowing for a more efficient representation of the electronic structure. By employing Effective Core Potentials, computational resources are conserved, as the intricate details of the inner-core electron behaviour are approximated, while still preserving the accuracy of the outer-shell electron interactions. This method is especially advantageous in large molecular systems, where the inclusion of inner-core electrons in calculations could become computationally prohibitive. ECPs, therefore, stand as a strategic tool in achieving a balance between computational efficiency and accurate representation of electronic interactions in quantum chemical simulations.

The determination of fitting parameters for an ECP requires a diverse array of methodologies, which may include empirical fitting to experimental datasets, fitting procedures applied to *ab initio* calculations, or a synergistic combination of these approaches. Broadly, the overarching objective is to ascertain a set of fitted parameters that optimally reproduces the pertinent properties of valence electrons while simultaneously minimizing the deviation between the ECP and the authentic potential arising from the core electrons. Following the establishment of these fitting parameters, the resultant ECP stands poised for integration into quantum chemical computations, facilitating the examination of molecular behaviour featuring the designated atom or group of atoms. Particularly advantageous for heavy atoms, ECPs address

the computational challenges posed by a considerable number of inner core electrons in quantum chemical calculations.

2.3.3 Exchange Correlation Functionals

The exchange-correlation energy delineates the disparity between the exact energy and the energy derived from all other classical contributing factors. Within its purview, the exchange correlation encapsulates the exchange energy arising from wavefunction anti-symmetry and the nuances of electron movement correlation. Its value is well established, analytically and numerically, for a uniform electron gas, which is only a model system. When dealing with large and more structured realistic systems, an imperative need arises for an approximation, such as the local density approximation (LDA) pioneered by Kohn and Sham. [154]

The efficacy of LDA is evidenced by its ability to predict trends related to structures, bond lengths, and vibrational frequencies. However, its precision falters when faced with swiftly changing electron densities. LDA exhibits a proclivity for electron densities that are more diffuse than those inherent in the actual physical systems, leading to over-binding, the contraction of bond lengths, or an inadequate representation of hydrogen bonds. While it stands as a valuable tool, its limitations underscore the necessity for refined approaches in capturing the intricate dynamics of systems characterized by rapid electron density variations.

The improvement of this methodology is the addition of gradient corrections, known as the General Gradient Approximation (GGA), which for example for a closed-shell system results in:

$$E_{XC}^{GGA}[\rho(r)] = \int \rho(r) \varepsilon_{xc}(\rho, \nabla \rho) dr.$$

In this thesis, emphasis is placed on the consideration of the gradient and higher derivatives of the electron density rather than solely the local density. To enhance the empirical robustness, supplementary experimental results can be incorporated alongside the theoretical and computational *ab initio* data, leading to refined empirical parameters and consequently, improved molecular geometries. The self-interaction error inherent in the LDA and GGA calculations as mentioned above impairs the descriptive capabilities of both LDA and GGA in characterizing localized electronic states. In this respect hybrid functionals is a useful way forward which based on Becke's arguments [155] using the adiabatic connection method can take the general form of:

$$E_{XC}^{Hyb} = (1-a)E_X^{DFT} + aE_X^{HF} + E_C^{DFT}.$$

The value of "a" is the fraction of HF exchange included. The implementation of hybrid exchange-correlation functionals represents a notable advance over previous methods, enabling a higher degree of accuracy. However, this enhancement comes with a significant computational cost, posing a substantial downside to their practical exploitation.

2.4 Molecular Mechanics

As previously discussed, *ab initio* techniques are practical for smaller chemical systems, but their high computational cost makes them currently impossible to implement on the scale required for large systems as will be discussed in this thesis.

In molecular mechanics, molecules are treated as assemblies of interacting atoms, and their behaviour is described using empirical potential energy functions of nuclear coordinates. These functions typically involve terms for bond stretching, angle bending, torsional rotations, and non-bonded interactions (such as van der Waals forces and electrostatic interactions) [156]. The parameters in these functions are often derived from experimental data or high-level quantum mechanical calculations. When examining large dynamic systems where the movement of the atoms is more important than the movement and interactions of individual electrons molecular mechanical techniques are ideal. The scaling of the calculation is no longer with respect to the number of electrons but to the number of atoms within the system therefore the costs of calculating atoms will be reduced significantly when compared to ab initio techniques as shown in Figure 7. [157]

Several MM methods offer opportunities for simulating molecular systems, such as static lattice, molecular dynamics, Monte Carlo [158] simulation, and normal mode analysis. MM simulations provide enhanced scalability for system sizes compared to quantum mechanical simulations, enabling the seamless handling of calculations involving large cluster or models. Interatomic potential functions within MM simulations can be parameterized through fitting to empirical data or ab initio energy surfaces. In our QM/MM calculations, we employed the Hill-Sauer [159, 160] force field, which is derived from ab initio calculations and is extensively utilized for simulating zeolites. This potential is specifically parameterized to capture the key interactions within zeolitic materials. It has a short-range Buckingham potential which describes the van der Waals and Pauli repulsion interactions between the oxygen and silicon atoms. It also has a Coulombic interaction for models that have partial charges scheme to ensuring accurate electrostatic representation of the zeolite framework. Long-range electrostatics are typically handled using Ewald summation or electrostatic embedding in QM/MM calculations. The final component to the forcefield is the three-body angle bending terms to ensure the structural stability by maintaining the correct Si-O-Si and Al-O-Si bond angles. The Sauer-Hill potential has been validated against experimental data and high-level quantum mechanical calculations, making it a reliable choice for modelling zeolites. It plays a crucial role in QM/MM simulations by accurately describing the mechanical response of the framework while allowing computationally expensive QM calculations to be focused on the active site.

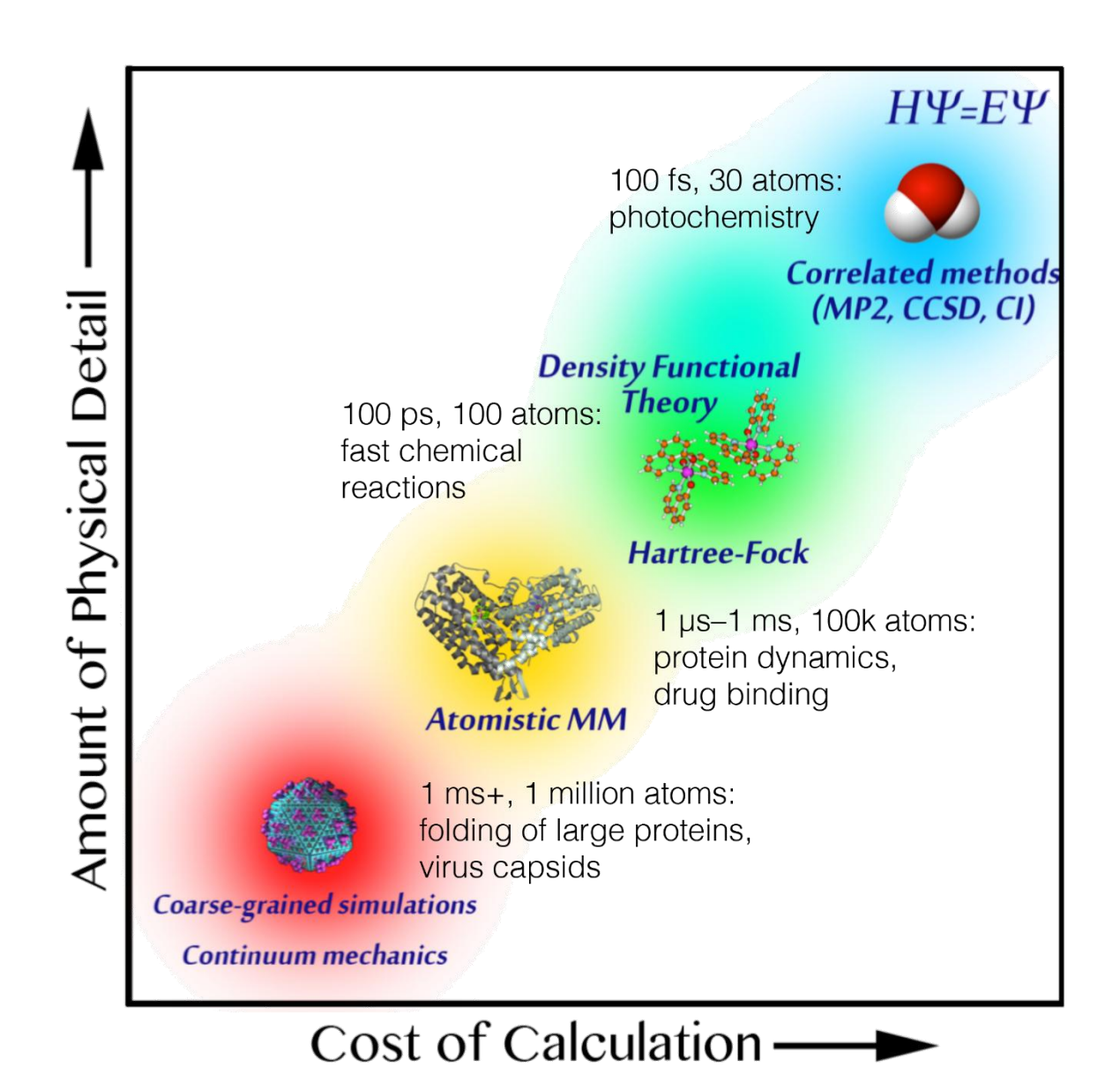


Figure 7: Comparison of modelling techniques based on the balance between the level of physical detail and the computational cost. [67]

Furthermore, the MM methods have been employed in the structure prediction work using the Knowledge Led Master Code [161] (also known as KLMC) as described in more detail in Chapter 5 of this thesis. This code implements a number of competing global optimisation as well as energy landscape sampling techniques based on traditional Monte Carlo approaches.

2.5 QM/MM Embedding

QM/MM embedding in hybrid mechanical calculations allows for the application of high-level electronic structure methods to a central set of atoms, maintaining accuracy, while employing molecular mechanics (MM) methodology for the surrounding system, providing an accurate depiction of the environment. This approach proves particularly advantageous for studying flexible structures. For zeolite chemists, the primary advantage of QM/MM embedding lies in its capacity to investigate defects and adsorption processes in isolation, circumventing the periodic boundary conditions imposed by competing software that relies solely on *ab initio* methods.

In most QM/MM calculations, the total energy of the system is additive, constituting the sum of the contributions from the QM, MM, and interface terms. ChemShell offers three distinct methods for QM/MM embedding [151]: Mechanical Embedding, Electrostatic Embedding, and Polarised Electrostatic Embedding. Mechanical Embedding is employed when the interaction between the QM and MM regions lacks electrostatic components, relying solely on interatomic potentials. In Electrostatic Embedding, charges from the MM centre polarize the QM region. Polarised Electrostatic Embedding follows similar principles but allows the QM charge density to induce polarization in the MM atoms. The breakdown of the layers found in QM/MM techniques can be observed in Figure 8.

The QM/MM methodology offers several key advantages:

 High Accuracy: QM/MM simulations can attain high accuracy by employing a sophisticated QM method, leveraging available computational resources effectively.

- Modelling Large Systems: QM/MM is particularly adept at modelling large systems
 with precision, making it well suited for studying complex structures like enzymes and
 zeolites. Achieving comparable accuracy with purely quantum mechanical methods can
 be challenging for such extensive systems.
- Studying Rare Events: QM/MM excels in investigating rare events such as conformational changes, chemical reactions, and other processes characterized by long timescales or low probabilities. This capability enables the exploration of dynamic phenomena that may be challenging with other methods.
- Flexibility: QM/MM is a versatile method that can be applied to simulate a diverse range of systems, spanning from small molecules to large macromolecules and condensed matter systems. This flexibility makes it a valuable tool across various scientific domains.

The boundary region, situated between the QM and MM regions, plays a crucial role. Two methods, dependent on whether covalent or ionic bonding predominate, have been developed for this purpose. For the chosen pure ZSM-5 clusters in this study, pseudo atoms are strategically placed on the bonds broken by the interface, coupling the region appropriately [162]. To prevent improper polarization in the QM calculation, charges on the atoms in the boundary region are adjusted, and the forces on linked atoms are relocated within the MM part of the simulation. This careful treatment ensures a robust and accurate representation of the interaction between the quantum and classical regions in the QM/MM embedding framework. The choice of larger QM regions leads to more accurate results at the cost of a significant increase in the computational cost, whereas, using too small QM regions can cause vital electronic and quantum effect to be incorrectly interpreted and therefore compromising the results. The selection of appropriate QM methods and force fields stands as a pivotal factor

with profound implications for the accuracy of results in QM/MM simulations. Managing electrostatic interactions across the QM/MM boundary introduces an additional layer of complexity. Approaches such as the electrostatic embedding scheme, although beneficial, have the potential to introduce artificial charge transfer between the QM and MM regions. This introduces a potential influence on the overall accuracy of the simulation, adding an additional complexity to the treatment of electrostatic interactions between the layers of the QM and MM regions.[22]

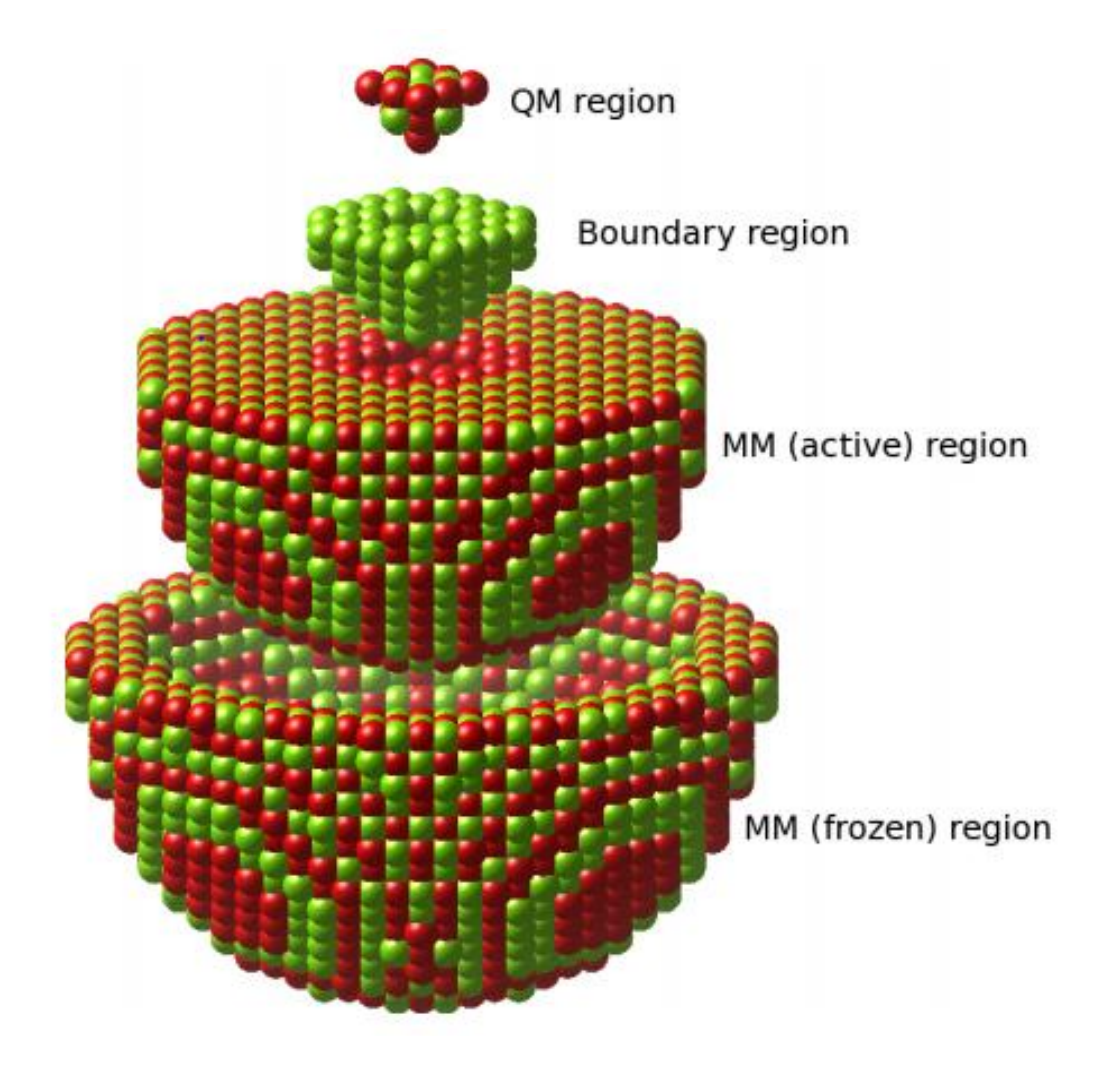


Figure 8: The QMMM embedding setup used within both Py and Tcl ChemShell. Progressing from top to bottom: the quantum mechanical region all ab initio calculations; boundary region; the relaxed MM ions; and the frozen MM ions. The outer most region (not displayed) contains point charges to represent the bulk structure.[2]

2.5.1 QM/MM Coupling

The core aspect of the work conducted is the density functional theory that is implemented with the QM/MM ChemShell package. This software package was originally developed by Sherwood et al. [22], where various additive and subtractive approaches used in both solid-state and biomolecular modelling are employed to provide energies for a wide range of systems.

The main group of approaches that is implemented in the ChemShell software is the additive scheme which expresses total energy as a sum of MM, QM, and additional coupling terms, as demonstrated by the following equation:

$$E = E (inner, QM) + E(outer, MM) + E(couple, QM/MM)$$

E is the value of the energy of the system, E (inner, QM) is the total energy of the QM region using DFT, E (outer, MM) the total energy of the region calculated with molecular mechanics and the E(couple, QM/MM) describes the interaction between QM and MM regions. The coupling interaction between the QM and MM regions is formed by cutting the cluster and the new terminating atoms are saturated with "link" (or pseudo) atoms. As discussed above, link atoms are virtual atoms with the purpose of smoothly transition between the QM and MM portions of the system, allowing for the calculation of accurate electronic structure properties in a specific region while efficiently modelling the rest of the system with a less computationally demanding classical force field. Link atoms stabilise the charges at terminal positions and function as a correction for bond dipoles, ensuring the accurate representation of the electrostatic potential. To prevent non-physical double counting, it is essential to exclude the corresponding MM terms when calculating the total energy.

An alternative method, not employed in this thesis, is the subtractive approach, which applies the MM scheme to the entire system and subtracts the MM energy of the inner system to remove the double counting of the QM region and the linking atoms. The subtractive approach is expressed as follows:

$$E = E (inner + Link, QM) + E(inner + outer, MM) - E(inner + link MM)$$

The final approach is known as intermediate approaches. In this approach, a transitional zone is introduced between the quantum and classical regions, aiming to achieve a smooth and accurate representation of the molecular system by typically containing a set of transition or buffer atoms that help bridge the two regions. Is expressed in the following equation:

$$E = E (inner + Link, QM) + E(inner + outer, MM) - E(couple QM/MM) - E(link, MM)$$

The distinctive feature setting the QM/MM hybrid method apart from other software lies in its energy calculation methods. This approach employs techniques within the Quantum Mechanics domain that do not necessitate periodic boundary conditions. The segmentation of the QM and Molecular Mechanics clusters is executed in a manner where all QM terminal atoms are designated as oxygen atoms, later saturated with hydrogen to form O-H groups. As previously discussed, our QM region is split into two smaller groups with differing basis sets. The most central atoms are treated with def2-TZVP [153] and the outer QM group with def2-SVP [153]. Any subsequent species added and/or removed from the full cluster are only taken from the central QM region that is undergoing the highest level of calculations. As the QM and MM regions are treated differently all classical charges normally present in the QM region are removed from the MM calculations.

When choosing among multiple candidates' sites of interest, calculations have been performed at the intersection of the channels present within some zeolites (most importantly for this work ZSM-5) as these are suspected place of formation of active sites for adsorption and stabilisation of various bulky species such as Pt cluster due to having the largest available space for cluster formation.

2.5.2 Cluster Formation

The formation, or set-up of a new cluster that is ready to perform QM/MM calculations onto is a long multistage process. It starts with the formation a large MM cluster that is first generated using a single unit cell of the target material, relaxed to its equilibrium geometry under periodic boundary conditions using an MM code (GULP [163]) with Hill-Sauer Molecular Mechanical force-field [164, 165]. The outcome is a starting point, which ChemShell then expands to the required size, enabling the cutting of a non-periodic cluster. For zeolites, the resulting cluster takes on an approximately spherical shape requested by users. In contrast, when studying surfaces, ChemShell cleaves a hemisphere from a 2D periodic slab. This streamlined process lays the foundation for subsequent QM/MM calculations, ensuring an effective representation of the desired system while accommodating the specific characteristics of different material types. The outer edges of the cluster are terminated with point charges. This is accomplished by sampling the electrostatic field of the interior of the cluster and placing these point charges with the aim of reproducing the effect of bulk within cluster as accurately as possible but cheaply as the effect of these outer point charges onto the target QM site is very small. This process is demonstrated within Figure 9:

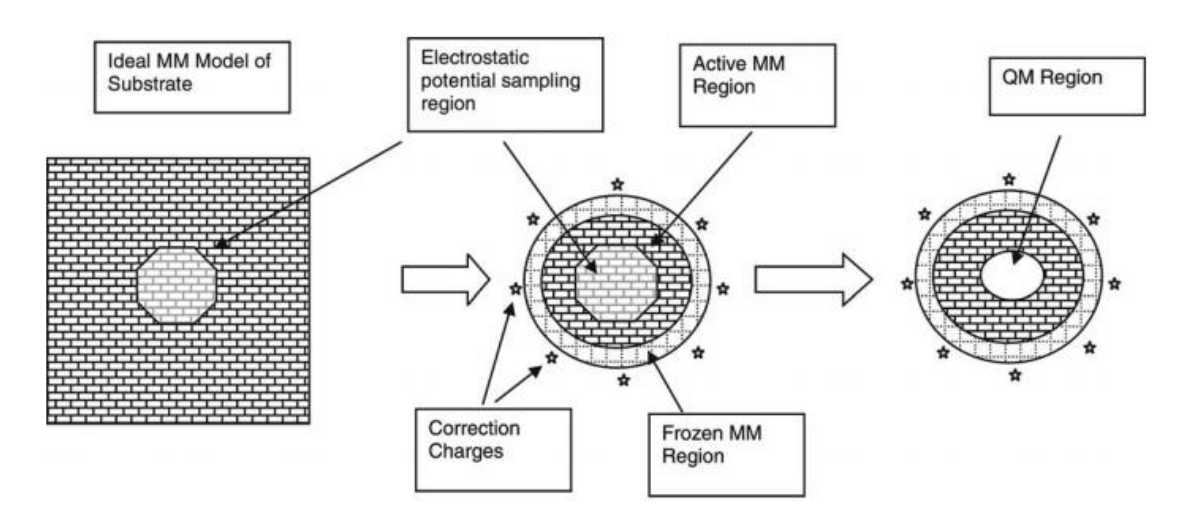


Figure 9: Generation of finite cluster model for ChemShell applications. [60]

Modifications of the cluster model, such as the introduction of Pt atom in the place of Si could now be introduced to the cluster model. Alternatively, the introduction of the hydroxyl nest as shown in Figure 10, can be achieved by removing the central Si atom and saturating the dangling oxygen atoms with hydrogen atoms.

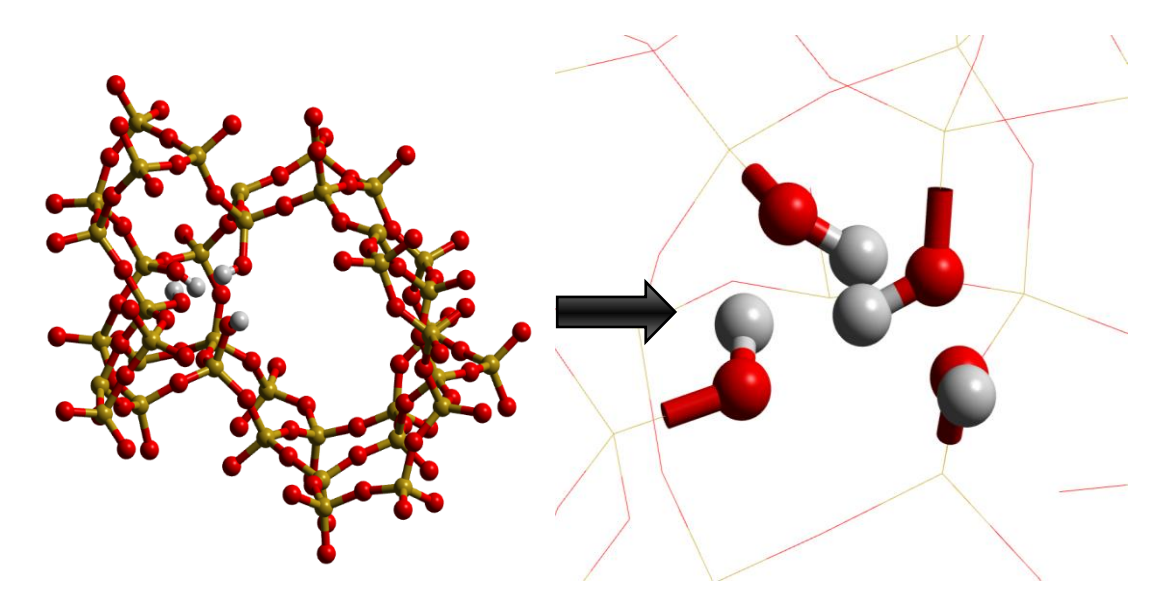


Figure 10: Modified QM/MM cluster after the embedding setup process showing the entire QM region utilised of ZSM-5 followed by a close up of the Hydroxyl nest defect site. Atom colour codes: Si: yellow, O: red and H: white.

2.5.3 Geometry Optimisation

The main form of calculation performed aim to find the lowest energy structure of the cluster generated, which can be achieved by iteratively adjusting the atomic coordinates of a molecular system to find the configuration that corresponds to the minimum energy or another specified criteria. The process seeks to identify the most stable and energetically favourable arrangement of atoms. In each step the Self-consistent field (SCF) method, also known as the iterative solution of the Kohn-Sham equations, is used to obtain a self-consistent charge density or Kohn-Sham molecular orbitals.

The process begins with the cluster that has been generated through the process described previously (Cluster Formation). Then, the electronic structure of the system is calculated using quantum mechanical methods at the DFT level or other higher-level *ab initio* approaches to determine the electronic energies and wavefunctions (Kohn-Sham orbitals). The forces acting on each atom in the system are computed based on the calculated electronic structure. Forces represent the gradient of the potential energy surface (but opposite in direction) and guide the movement of atoms toward the optimal geometry. The atomic coordinates are adjusted along the negative gradient of the potential energy surface, aiming to minimize the energy of the system. In ChemShell, the Limited-memory Broyden–Fletcher–Goldfarb–Shanno (BFGS) [166-169] optimization algorithm is the default option for geometry optimization and the method used for this thesis. This adjustment is done iteratively until specific convergence criteria are met. Once the optimization converges, the final optimized geometry, along with the corresponding electronic structure information, is recorded. Users can analyse the results, such as bond lengths, angles, and overall molecular stability.

Microiterative optimization techniques [170] have been integrated into the DL-FIND [171] optimization library, originally specifically tailored for combined QM/MM calculations within the Tcl ChemShell computational chemistry platform. In a traditional geometry optimization

process, each step necessitates evaluations of both quantum mechanical (QM) and molecular mechanical (MM) components at the updated geometry. This implies that the relaxation rates of the QM and MM regions must align. However, in a microiterative optimization approach, the system is partitioned into an inner region comprising, at minimum, the QM atoms, and an outer region encompassing the remaining system components. Following each optimization step of the inner region (referred to as the 'macroiterative' cycle), the outer region undergoes full optimization (known as the 'microiterative' cycle). By employing this optimization strategy, the number of QM evaluations is substantially reduced, albeit at the expense of increased MM evaluations for the outer region. To expedite this process, an electrostatic potential fit is employed to approximate the MM region during the environmental relaxation phase, enhancing efficiency without compromising accuracy. Microiterative optimisations are commonly utilized for large-scale heterogeneous catalysis simulations when running minimisation and transition state optimisation.

2.5.4 Nudge Elastic Band Calculations

The Nudged Elastic Band (NEB) method was employed to determine the minimum energy pathway (MEP) and activation barriers associated with reaction processes in zeolites. NEB is particularly useful for locating transition states in solid-state and heterogeneous catalytic systems, where reaction intermediates must traverse potential energy landscapes influenced by the surrounding framework. NEB calculations rely on a series of intermediate structures, or "images," that interpolate between the reactant and product states. These images are connected by virtual springs to maintain continuity along the reaction coordinate. The total force acting on each image consists of two components: (i) the true physical force derived from the potential energy surface (PES), which drives the system toward the MEP, and (ii) the spring force, which

preserves the smoothness of the path and prevents images from collapsing onto local minima. To refine the highest-energy image into a transition state, the Climbing Image NEB (CI-NEB) method was employed. In this approach, the highest-energy image is dynamically adjusted to move uphill in energy while eliminating the spring force, ensuring an accurate representation of the transition state. The NEB calculations yielded an energy profile along the reaction coordinate, allowing for determination of activation barriers and intermediate states. The energy of each image was extracted and plotted to visualize the MEP. The transition state was identified as the highest-energy image along the path and further refined using CI-NEB where necessary.

The results from NEB calculations provided crucial insights into the reaction energetics within the zeolite framework, particularly in understanding the role of hydroxyl nest clusters in catalytic processes. These findings were subsequently used to compare different zeolite structures and their influence on reaction kinetics.

2.6 Resources

The QM/MM simulations conducted in this thesis using the Python ChemShell version, optimization and energy calculations were executed with the QM code NWCHEM and the MM code GULP [163] (General Utility Lattice Program) within the ChemShell environment. In the Tcl ChemShell version, the QM code GAMESS-UK (General Atomic and Molecular Electronic Structure System) was utilized alongside the MM code DL-POLY [172].

The computational workload for these simulations was first handled by the Archer and then by its successor Archer 2¹ UK National High-Performance Computing Facility. The smaller

-

¹ https://www.archer2.ac.uk/

calculations were conducted on the UCL wide THOMAS, YOUNG², Katheleen³, and Grace⁴ supercomputers and UCL Chemistry Faraday⁵ cluster. Resources were also provided by STFC Scientific Computing Department's SCARF⁶ cluster to run tests for the new Python ChemShell updates. These cutting-edge computing resources played a crucial role in enabling the complex calculations required for the QM/MM simulations presented in this research, showcasing the significance of advanced computing infrastructure in pushing the boundaries of molecular modelling and simulation studies.

2.7 Justification of the Choice of Software

The work was performed primarily with the ChemShell packages integrating with the NWChem [173] or GAMESS-UK [174] as the QM drivers and DL-POLY [172] or GULP [163] as the MM drivers. ChemShell employs the embedded cluster hybrid QM/MM approach, which stands as our preferred methodology for studies, on massively parallel computing platforms, without feasible alternatives. ChemShell is in the unique position of providing the QM/MM packages as well as the vibrational calculations modules that allow for the following results.

2.8 Benchmarking

A benchmarking test was performed on our clusters using ChemShell for both Python and Tcl based [18, 149] calculations on the UK's National supercomputing machine ARCHER2 as

² https://www.rc.ucl.ac.uk/docs/Clusters/Young/

³ https://www.rc.ucl.ac.uk/docs/Clusters/Kathleen/

⁴ https://www.rc.ucl.ac.uk/docs/Clusters/Grace/

⁵ https://www.rc.ucl.ac.uk/docs/Clusters/Faraday/

⁶ https://www.scarf.rl.ac.uk/

shown in Figures 11. This study aims to explore the utilization of suitable computational nodes for the specific research to minimize unnecessary computational expenses.

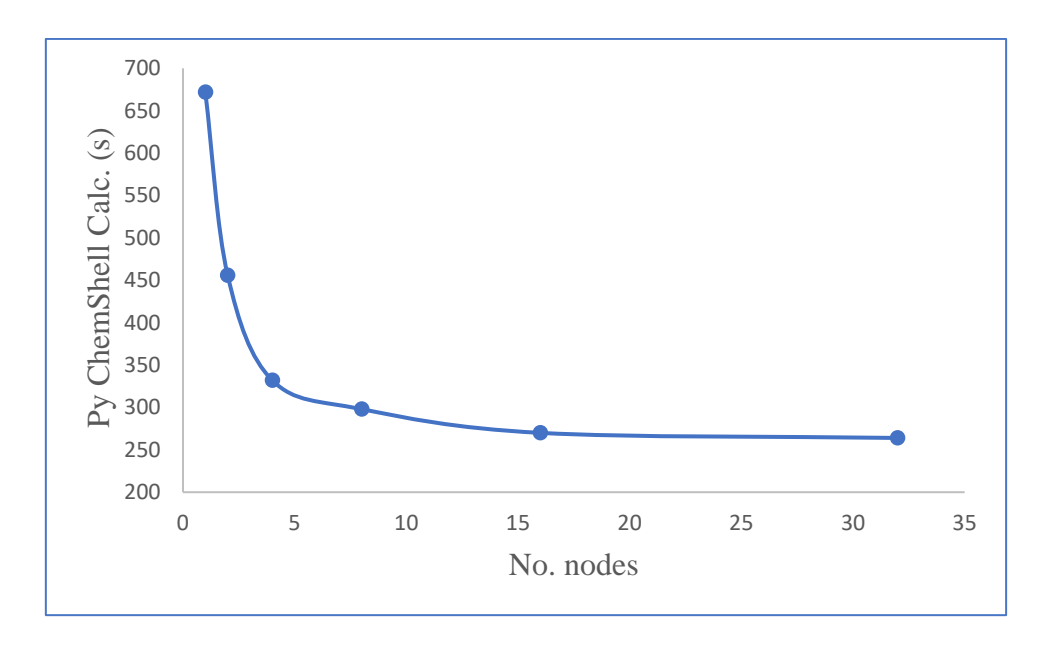


Figure 11: Benchmarking of Python ChemShell with NWCHEM calculations by varying nodes on Archer2 machine. The cluster used to perform these calculations was a 5 atoms QM region of ZSM-5 using the def2-TZVP basis set.

The results from the benchmarking shown in Figure 11 encourage the use of four nodes on the Archer2 machine as it has the reasonable usage of resources as increasing to eight nodes only provides

Chapter 3: Formation of Hydroxyl nest in Zeolites

3.1 Introduction of Hydroxyl Nests

As previously noted in Chapter 1, zeolites such as ZSM-5 are thought to contain defects when Si or metal ions are removed from the framework, and it has been proposed that this defect will then protonate leaving 4 OH groups called hydroxyl nest, or hydrogarnet defects. This chapter examines the structural and chemical characteristics of hydroxyl nests within zeolite frameworks, focusing on their formation, hydrogen bonding patterns, and the implications for catalytic activity. We investigate the geometry of defect sites, particularly in ZSM-5, Faujasite, Chabazite and α -quartz, revealing significant insights into the hydrogen-bonded ring structures and the associated bond lengths and angles. The flexibility of hydroxyl nests is highlighted, with two proposed mechanisms for proton movement: proton transfer between oxygen atoms and proton rotation around an oxygen centre. These mechanisms are crucial for understanding catalytic processes in zeolites. Additionally, the chapter addresses the Loewenstein rule, which precludes Al-O-Al linkages in zeolite frameworks and provides an overview of the current diversity in natural and synthetic zeolite species, emphasising the wide range of aluminium contents and their implications for zeolite structure and function. Building on this foundation, we will next explore strategies to increase the number of hydroxyl nests within the zeolite framework to generate mesopores, which will involve synthesising and characterising zeolite samples with an enhanced hydroxyl nest density, followed by a detailed study of their structural and catalytic properties.

3.1.1 Computational Approach for ZSM-5

All calculations use the QM/MM approach described in Chapter 2.5 to model hydroxyl nest defects. The full QM/MM cluster measured 60 Å in diameter and was centred on a Silicon atom which was to be used as the site for defect formation. In total, around 6500 atoms were free to undergo relaxation in each calculation. The outermost 5 Å of the cluster had all atoms frozen in their bulk positions (as determined by prior relaxation using GULP), whilst all other atoms within a radius of 25 Å of the cluster origin were allowed to relax.

The innermost QM region comprised those atoms described by the all-electron density functional theory calculation and ranged in size from 126-180 atoms depending on the presence of vacancies. This QM region size was chosen to minimise computational cost while providing a calculation that can most accurately describe the region without the effect from the MM region. The calculations for the QM clusters were performed using the NWCHEM package, while for the MM part, the GULP package was employed, with the Hill-Sauer Molecular Mechanical force-field with some modifications. All atoms within the effects of the forcefield are assumed to be between atoms binding to each other by polar covalent bonds. The modifications that have been made to the Hill and Sauer [159, 160] forcefield to prevent interaction between the outer most point charges represented as F atoms used to describe the bulk effects of the framework that occur within the GULP package. The modifications are designed to remove these effects to preserve the integrity of the cluster at reproducing the bulk structures. The following terms where added:

MOLMEC: Program locates molecules based on either an input connectivity or by automatically locating bonds based on covalent radii and subtracts Coulomb terms between bonded atoms and between atoms bonded to a common third atom [175]. Bond length tolerance was implemented with the command rtol set to 1.1 instead of the default 1.2.

ELEMENT: This option is designed to change an element's properties. In this thesis, the covalent radius of F was set to 0 Å.

All modifications are present in the forcefield as shown in Appendix.A.2.

The Becke97-2 [176] exchange-correlation functional was used throughout this study due to its good representation of both molecular species and oxides in previous work conducted in the literature.

A choice of the basis set discussed further below, allows us to employ intermediate quality basis sets in the QM region. These calculations employed a dual basis set as previously discussed in Chapter 2.3.1, with the combination of Def2 TZVP [153] polarization basis set for Si, O and H atoms in the inner most region of the QM atoms consisting of 21 atoms (1 central T-site (Si + 4 O) plus the 4 adjacent T-sites (Si + 3 O)). The outer most QM region was described using Def2 SVP [153] on all remaining Si, O and H link atoms.

3.1.2 Choice of Model Cluster

To perform the QM/MM calculation, we first created a spherical embedded-cluster model of ZSM-5 from a unit cell of silicious ZSM-5 pre-optimised at the MM level using the GULP package. After creating a pure ZSM-5 cluster model as shown in Figure 12, we construct various active sites. For example, for a hydroxyl nest we removed a Si and protonated the four adjacent O atoms. The QM region which is contained within the active part of the model is terminated with only oxygen atoms and as previously noted, we have added the hydrogen (link atoms) to saturate the terminal oxygen atoms. Link atoms compensate the charge at terminal positions and act as a bond-dipole correction to ensure an accurate electrostatic potential. The modified cluster with a single hydroxyl nest is depicted in Figure 13.

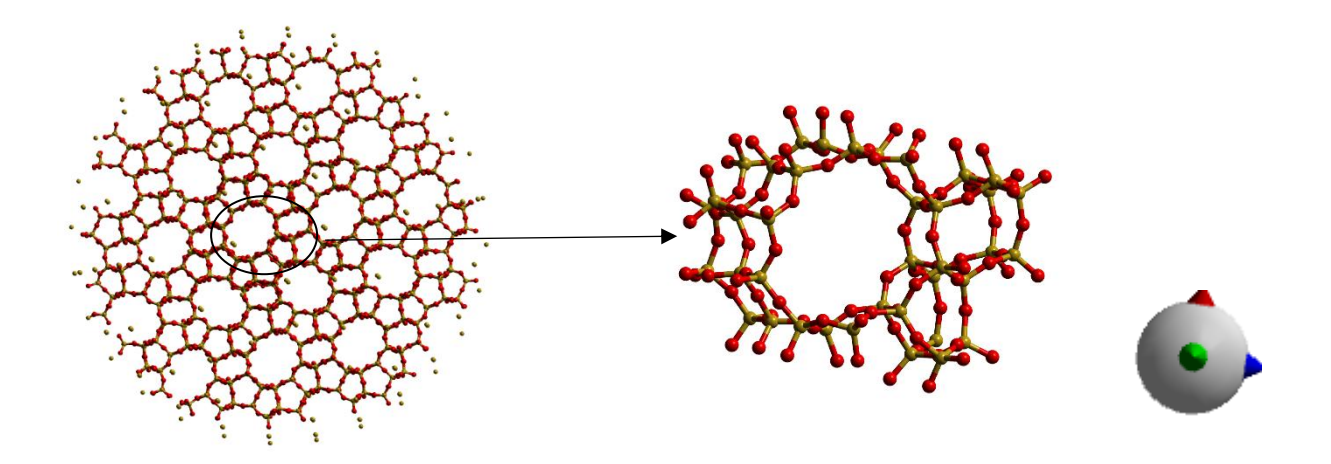


Figure 12: The QM/MM embedding setup: the full pure silicious ZSM-5 cluster without 3D perspective (left) with the quantum mechanical region (right). The outermost region contains point charges to ensure the Madelung potential in the central region of the cluster to accurately reproduce bulk. Atoms colour codes: Si (RED) and Oxygen (GREEN). Cartesian axes directions aligned with the crystallographic axes: X-axis (RED), Y-axis (GREEN) and Z-axis (BLUE).

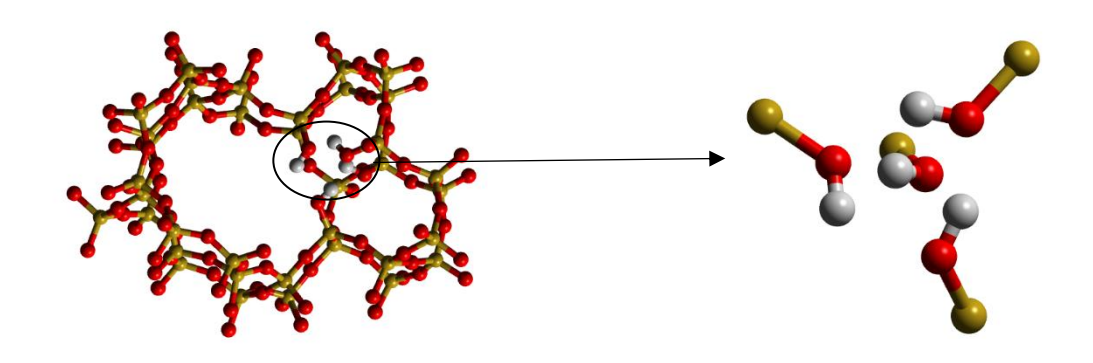


Figure 13: The QM region of the full pure ZSM-5 cluster with the introduction of a single hydroxyl nest defect (left). A close-up of the hydroxyl nest defect site generated for the theoretical QM/MM calculations (right). Atoms colour codes: Si (RED), Oxygen (GREEN) and Hydrogen (WHITE).

3.2 Results and Discussion

In this chapter, we investigate the formation of hydroxyl nest or hydrogarnet or [4H]_{Si} substitutional defects by creating a defect through the removal of a silicon atom and protonating the newly formed terminal oxygen atoms. This concept of the hydroxyl nest was originally proposed by Barrer and Makki [177] in 1964, who proposed that these defects contribute to the high hydrogen bonding properties observed in zeolites, specifically in H-ZSM-5[178]. However, our study goes beyond the formation of a singular hydroxyl nest (removal of a single silicon atom) to explore the aggregation of these defects, resulting in the formation of larger pores known as mesopores. This development was made possible by advances in computational tools, particularly hybrid QM/MM calculations, and the application of IR and Raman spectroscopy within the hybrid QM/MM ChemShell package. Our computational mechanistic study focuses on these findings, providing complementary insights into the experimental results. Additionally, we present a comprehensive analysis that offers a clear assignment of the main spectroscopic features associated with the growth of hydroxyl nests, extending up to 5 Tsites, that correlate to experimental results. The most common means of determining defect formation (E_f) energies is the reaction energy to form the defect from the pure silicious ZSM-5 as in:

$$E_f = E(defect) + E(byproduct) - E(pure) - E(reactants)$$

where E(defect) is the energy of the cluster with the introduced defect (ZSM-5 cluster with hydroxyl nest defect site included), E(byproduct) is the energy of the atoms removed from the zeolite cluster (the removal of silicon to form the biproduct which we take as Orthosilicic

acid – SiOH₄), *E (pure)* the energy of a pure silicious ZSM-5 cluster and the *E(reactants)* is the energy of the molecules used to protonate the defect site once silicon is removed (water molecules – H₂O). Zeolites hydroxyl nest defect has so far been studied using only semi-classical, semi-empirical techniques and *ab initio* periodic techniques however has not with QM/MM methods. The energies of these SiOH₄ and H₂O molecules in a vacuum using NWChem under Python ChemShell and def2-TZVP basis set are recorded as -593.115 eV for SiOH₄ and -76.446 eV to 3 decimal places.

While the semiclassical models tend to overestimate the energy of the defect formation, 1.02 eV being the lowest value reported for grossular by K. Wright, R. Freer et al 1994 [106], the local density approximation applied in the periodical model of this defect in α -quartz seems to over bind it. In particular J.C. Lin, M.C. Payne et al. (1995) [179] have reported the negative defect formation energy of \sim -2.4 eV with respect to an interstitial water and of \sim -0.5 eV with respect to free water. Defect formation energies for the hydroxyl nest are given in Table 3.1 with results from previous work for comparison [36, 106, 180]. The results presented in this thesis and those already published show a clear discord between different techniques and cluster model chosen with a range of various both positive and negative values when observing the formation of hydroxyl nest defects. The results obtained with reference 1 are DFT calculations at the PW91 level with periodic boundary conditions and a Γ -point approximation applied to the structure of siliceous sodalite. Reference 2 are also obtained through DFT calculations employing periodic boundary conditions as implemented in the DSOLID/Dmol ³ code. The exchange and correlation functionals used include the local density (LD) and generalized gradient (GG) terms of Perdew and Wang 1991 [181]. As these various results show, there is a clear uncertainty about whether the formation of hydroxyl nest defect occurs through an exothermic or endothermic reaction. These results from previous calculations are a

product of their time, where the lack of computer resources has significantly reduced the scope of these simulations.

3.2.1 Formation of the Hydroxyl Nest

When we consider the defect formation as a process in which four isolated water molecules are brought to a defect site within a sodalite framework, from the vacuum we calculate the energy of formation to be -0.367 eV (-35.4 kJ/mol) for a single defect in sodalite. To compare results with previous theoretical calculations, we calculated the reaction energy for the equation in Chapter 3.2, with the extraction of an orthosilic acid molecule to form a hydroxyl nest in sodalite. The calculated theoretical value is similar to some of the previous work done as shown in Table 1 lying within the range of previous calculations but still did not fully agree with an energy difference in case of reference 4 being over 2 eV.

Table 1: Defect formation energies for hydroxyl nest in sodalite produced with ab inito methods.

Defects	Reference	1	Reference	2	Reference	3	Reference	4
	[179]		[182]		[180]		[106]	
Hydroxyl nest	1.8 eV		-0.5 eV		1.02 eV		-2.4 eV	

3.2.2 Formation of Hydroxyl Nest in other Zeolites

In the previous section, we thoroughly examined hydroxyl nest formation in sodalite, making comparisons from multiple studies to gain a deeper understanding of this defect's behaviour.

While sodalite, with its distinctive cage-like structure, has provided crucial insights into the mechanisms of hydroxyl nest formation, it is only one representative of the diverse family of zeolites. To fully understand the scope and implications of these defects, it is essential to extend our exploration to other zeolite frameworks, each characterized by unique structural and chemical properties.

This chapter transitions to investigating hydroxyl nest formation in several other key zeolites, including Chabazite (CHA), ZSM-5 (MFI), Mordenite (MOR), and Faujasite (FAU). These materials, while of intrinsic interest, are also widely utilised in industry for applications in catalysis, gas separation, and molecular sieving. By analysing hydroxyl nest formation within these frameworks, we aim to identify both commonalities and distinctions in defect chemistry across different zeolite structures. This comparative analysis will not only build upon the insights gained from sodalite but also provide a more comprehensive perspective on the role of hydroxyl nests in zeolite chemistry and their impact on material performance in practical applications.

The results for the formation of hydroxyl nest are shown in Table 2, all results were calculated with the energy of $Si(OH)_4$ and H_2O being calculated in Python ChemShell using Def2-TZVP with the values of -593.115 eV and -76.446 eV respectively as discussed in Chapter 3.2.

Table 2: The calculated reaction energies for reaction are based on the standard enthalpy of formation of a singular hydroxyl nest by removing a silicon atom and protonating the new lose oxygens.

Zeolites	Product (a.u.)	Reactant (a.u.)	$\Delta_{\rm f}{ m H}^{\circ}$ (a.u.)	$\Delta_{\rm f} { m H^{\circ}} \ ({ m eV})$
cluster				
ZSM-5	-19167.0522	-18879.7315	-0.00904	-0.246
СНА	-19823.4020	-19536.0709	0.00136	0.037
FAU	-15109.15685	-14821.84957	-0.0225	-0.612
MOR	-15749.4994	-16036.8447	-0.0147	-0.399
α -Quartz	-16175.9675	-15888.6455	-0.00806	-0.219

When analysing the results for hydroxyl nest formation using purely Python-based Chemshell calculations, a clear pattern emerges: most zeolites exhibit a negative energy change, with the notable exception of Chabazite. As shown in Table 2, the results vary, probably due to the diversity of framework types, each exhibiting different enthalpy of formation ($\Delta_f H^\circ$) for its respective clusters. For instance, zeolites like Chabazite, which consists of sodalite cages interconnected by hexagonal prisms, exhibit a relatively high degree of symmetry, featuring a singular T site. This increased symmetry enhances the structural stability of Faujasite, making the formation of hydroxyl nest defect sites more challenging within its framework.

In contrast, Faujasite and Mordenite, while also possessing a single T site, show considerably lower formation energies compared to Chabazite. Chabazite consists of single or double six-membered rings of tetrahedra (6mR) as secondary building units, while α -quartz features a three-dimensional network of interconnecting channels. The calculations presented in Table 2

were all performed on purely siliceous zeolites under identical temperature conditions, with no influence from acidic or basic environments.

The porosity and framework strength of each zeolite provide clear indications of how hydroxyl nest defects impact structural integrity. In general, the formation of hydroxyl nests introduces points of weakness, destabilizing the framework. However, some zeolites exhibit a degree of structural flexibility, allowing their frameworks to adjust to external changes such as temperature, pressure, or chemical environment without collapsing. This adaptability is a key factor contributing to the stability of certain zeolites in dynamic conditions.

3.3 Structure of Hydroxyl nest defects

The formation of a hydroxyl nest defect through the removal of a silicon atom marks the initial step in the creation of mesopores. In our model (see Figure 14), the removal of silicon leads to the formation of four silanol (Si-OH) groups situated at the defect site. The structure of the hydroxyl nest is clearly defined: three of the silanol groups are hydrogen-bonded to one another, forming a triangular arrangement, while the fourth silanol group remains loosely hydrogen-bonded to this triangular ring within the defect site. This configuration reflects the dynamic nature of the hydrogen bonding network in the hydroxyl nest.

3.3.1 Chabazite Triangular Hydroxyl Nest

The O-H bond lengths, as detailed in Figure 14, provide insight into the geometric structure of the nest. The precise arrangement and bonding within the nest suggest a degree of flexibility in the defect site, which may contribute to further structural transformations, such as the formation of larger mesopores. Understanding the factors controlling bond lengths and their

relationship to the overall structure is crucial for elucidating the role of hydroxyl nests in the mesopore formation process. Their O-H bond lengths for Chabazite are as follows:

Hydrogen 1 - 1.728 Å Oxygen 5 - 0.957 Å

Hydrogen 2 - 2.360 Å Oxygen 6 - 0.978 Å

Hydrogen 3 - 1.768 Å Oxygen 7 - 0.968 Å

Hydrogen 4 - 2.188 Å Oxygen 8 - 0.947 Å

The distance between the oxygen and the nearest hydrogen bonded proton atom as shown in Figure 14:

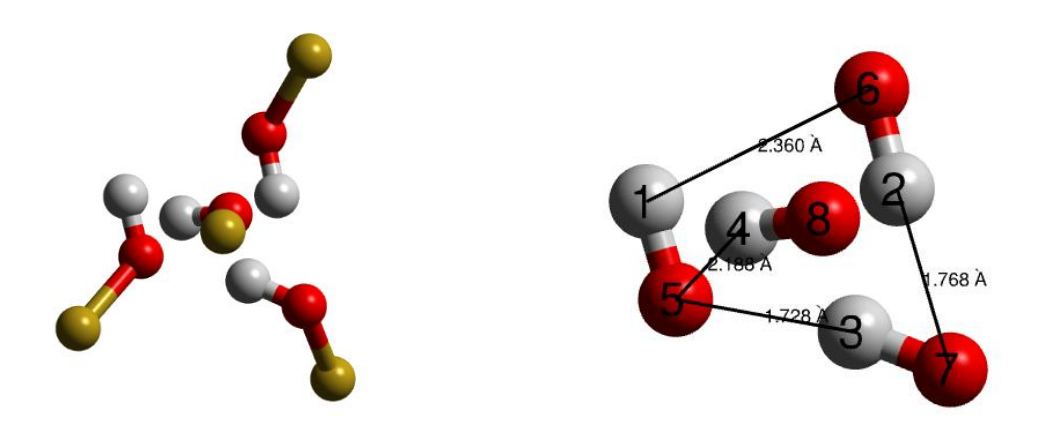


Figure 14: A singular hydroxyl nest defect within Chabazite zeolite after Python Chemshell Optimization with a view from above to show the triangular hydrogen bonded ring (right). The structural model of the hydrogen nest (left) defect (oxygen red, hydrogen white).

The geometry of the defect site suggests, as corroborated by numerous calculations [180], including our own, the presence of extensive hydrogen bonding interactions. Specifically, up to five hydrogen bonds are predicted to form in the ground state within hydroxyl nests. The fifth hydrogen bond occurs between oxygen-5 and hydrogen-2, with a bond length of 2.332 Å,

creating a pseudo double hydrogen-bonded ring involving hydrogen-1, oxygen-6, hydrogen-2, and oxygen-5. The bond lengths for these interactions are similar, measuring 2.332 Å and 2.360 Å. Based on these measurements, we can categorize the hydrogen bonds into two distinct types. The first type involves bonds between O-H and H, with bond lengths ranging from 1.7 to 1.8 Å, participating in a triangular ring formation. Conversely, hydrogen bonds involving hydroxyl groups outside this ring formation are not constrained spatially to participate in ring bonding and therefore are positioned outside the defect, resulting in an atypical hydrogen bonding pattern. These types of hydroxyl nests formations can be observed in Figure 14.

The defect's generic structure aligns closely with results from semi-classical simulations (e.g., K. Wright, R. Freer et al., 1994 [106]) and early ab initio LDA molecular cluster calculations (e.g., J. Purton, R. Jones et al., 1992 [183]). The Si-O-H bond angles vary between 113° and 125°, which is consistent with findings from various *ab initio* and molecular cluster calculations. Notably, the Si-O bond length in the silanols ranges from 1.61 to 1.65 Å, which is in close proximity to the 1.6 to 1.63 Å Si-O bond distances observed in the immediate vicinity of the defect. This bond elongation is more pronounced in molecular cluster calculations, likely due to artificial effects stemming from unrealistic boundary conditions. Nevertheless, the slight polarising effect induced by the defects in the zeolite framework contributes to bond elongation and may also account for the observed expansion of the zeolite structure.

3.3.2 ZSM-5 4 Membered ring Hydroxyl nest

The ZSM-5 hydroxyl nest cluster features a framework with 12 distinct T-sites in the orthorhombic phase. The selected site for this investigation is located at the intersection of the two channels running through the cluster, as this location provides ample space around the

defect site and a higher likelihood of interaction with adsorbates or reactants involved in catalysis traversing the channels. The hydrogen-bonded ring observed bears some resemblance to the cluster studied by A. Sokol [36] or K. Wright and R. Freer [106]. However, instead of the triangular ring plane, our system exhibits a four-membered ring of hydrogen-bonded silanol groups. The bond lengths of the ring's sides range from 1.7 to 2 Å, indicating a notable elongation of the hydrogen bond lengths due to the presence of the fourth silanol group. As demonstrated in Table 2, the defect formation enthalpy ($\Delta_f H^o$) of ZSM-5 is more exothermic than that of Chabazite, with an energy difference of approximately 0.3 eV, resulting in a transition from endothermic to exothermic behaviour. The Si-O-H bond angles in this configuration are more consistent, ranging between 120° and 122°, while the Si-O bond lengths remain stable at 1.6-1.63 Å in the vicinity of the defect. This type of hydroxyl nests formation can be observed in Figure 15.

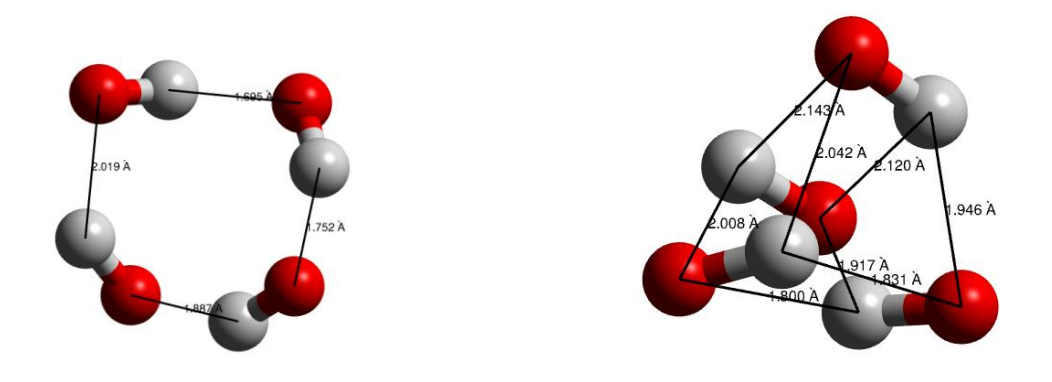


Figure 15: The atomical structure of optimised ZSM-5 hydroxyl nest defect (right), and the atomical structure of optimised α -quartz (left). (Oxygen red, hydrogen white).

3.3.3 α-quartz Double Hydrogen Bonds

In contrast, the hydroxyl nest defect observed in α -quartz (see Figure 15) is notably more compact. The hydrogen bonds are tightly packed, with all hydrogen atoms situated between 1.8 to 2.1 Å from two different oxygen atoms. Unlike the ZSM-5 cluster, α -quartz lacks the extensive channel system, resulting in greater framework strain exerted on the defect. This strain forces the silanol groups in the cluster to remain in close proximity, giving the cluster a more cuboid appearance due to the constrained arrangement of hydrogen bonds. This led to the formation of hydrogen bonding between oxygen and the two closest hydrogen atoms.

3.4 Movement in Hydroxyl nest clusters

As discussed in the previous subsection, clusters of hydrogen bonds in hydroxyl nest defects exhibit significant variability in the arrangement of atoms within the defect site. This flexibility suggests that the formation of these clusters involves a complex process. Two primary mechanisms are proposed to facilitate the movement of silanol groups within the hydroxyl nest defects:

1. **Proton Transfer Mechanism**: This method involves the transfer of protons between oxygen atoms within the hydroxyl nest. Known as proton hopping, proton transfer, or, in the context of cyclic systems, proton tautomerism or proton shuttling, this phenomenon is essential for catalytic activity in zeolites. Proton hopping between

acidic sites, such as Brønsted acid sites, significantly influences reaction mechanisms including cracking, isomerization, and dehydration. [184]

2. **Proton Rotation Mechanism**: Alternatively, the proton can exhibit rotational movement around an oxygen centre.

These two process could proceed classically over a potential energy barrier or through tunnelling, which involve the proton transitioning between equivalent positions. This phenomenon, known as proton exchange or proton dynamics, are proposed to play a crucial role in the behaviour of protons within the zeolite framework.

To further investigate the dynamic behaviour of hydroxyl nest clusters of hydrogen bonds, we employed Nudged Elastic Band (NEB) [185] simulations within the Chabazite zeolite framework. These simulations were conducted using the ChemShell software package [18] as discussed in Chapter 2. The NEB calculations find the minimum energy pathway (MEP) for a transition between two known states of a system, typically an initial reactant state and a final product state. The MEP represents the most energetically favourable path a system takes when transitioning between two states. It includes the highest-energy point along the path, called the transition state, which corresponds to the activation energy of the process. This technique is particularly useful for studying chemical reactions, diffusion processes, and other transitions where knowing the reaction mechanism and energy barrier is critical. The NEB simulations allowed us to capture the temporal evolution of proton transfer and rotation within the hydroxyl nests, providing insight into both the energetics and the structural rearrangements occurring in hedroxyl nests using images. The images are connected by virtual springs, forming an elastic band between the initial and final states. These springs prevent the images from collapsing onto each other or spreading too far apart, ensuring they are well-distributed along the reaction pathway. The flexibility of the Chabazite framework facilitated these proton dynamics, as subtle distortions in the Si-O bond angles and bond lengths at the defect sites created favourable conditions for proton movement within the hydroxyl nest site.

Before running an NEB simulation, an initial geometry of the system is determined, based upon the work completed in the previous section acquired after optimization via energy minimization, and another set of results, where the hydrogen in the QM region have been optimized with the silanol groups hydrogen bonded to a different oxygen atom in the 3membered hydrogen bonded ring and the fourth silanol group left untouched. Once the simulation runs, ChemShell generates a trajectory file containing the positions of all atoms over time. These data can be analysed to observe structural changes, dynamic behaviour, and reaction mechanisms.

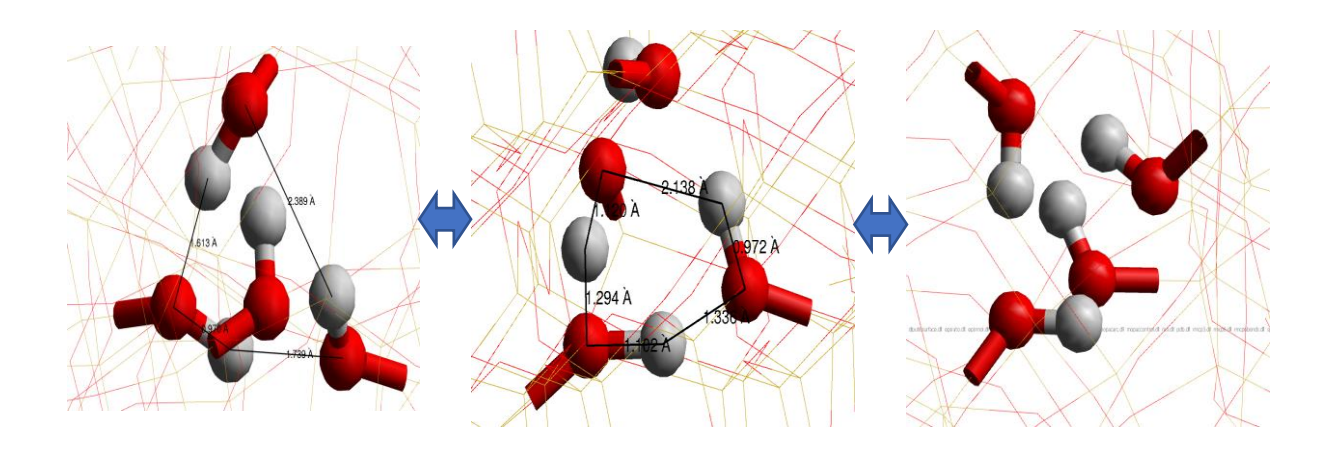


Figure 16: Hydroxyl nest imagining of the transfer of proton mechanism within the nest structure of ZMS-5.

To investigate the rotation or transfer mechanisms as shown in Figure 16 different images (excluding the starting and final images) were introduced showing the motion of proton around or between oxygen centres. The most relevant steps in the process are when the proton switches

which oxygen it is hydrogen bonded to the process of the bond breaking induced by the framework reorganization for the transfer of proton and the rotation of the proton to the opposite oxygen atom in rotation mechanisms.

When observing the transfer process through quantum tunnelling using NEB calculation we observed the elongation of the O-H bonds the energy profiles of which are shown in Figures 17 and 18. Taking a single O-H bond as an example it starts at a bond length of 0.970 Å within its normal expected range. The proton transfers away over time to 1.792 Å from the original oxygen atom therefore dissociating from the host oxygen to settle into a new bond distance of 0.968 Å to the opposing oxygen. Now looking at the reaction energy of the system we observe that the 5th image is the energy barrier when the bond distance stretches to 1.320 Å, the furthest point between both oxygens. The energy barrier required to overcome is 1.287 eV breaking an O-H bond within the triangularly bonded hydroxyl nest.

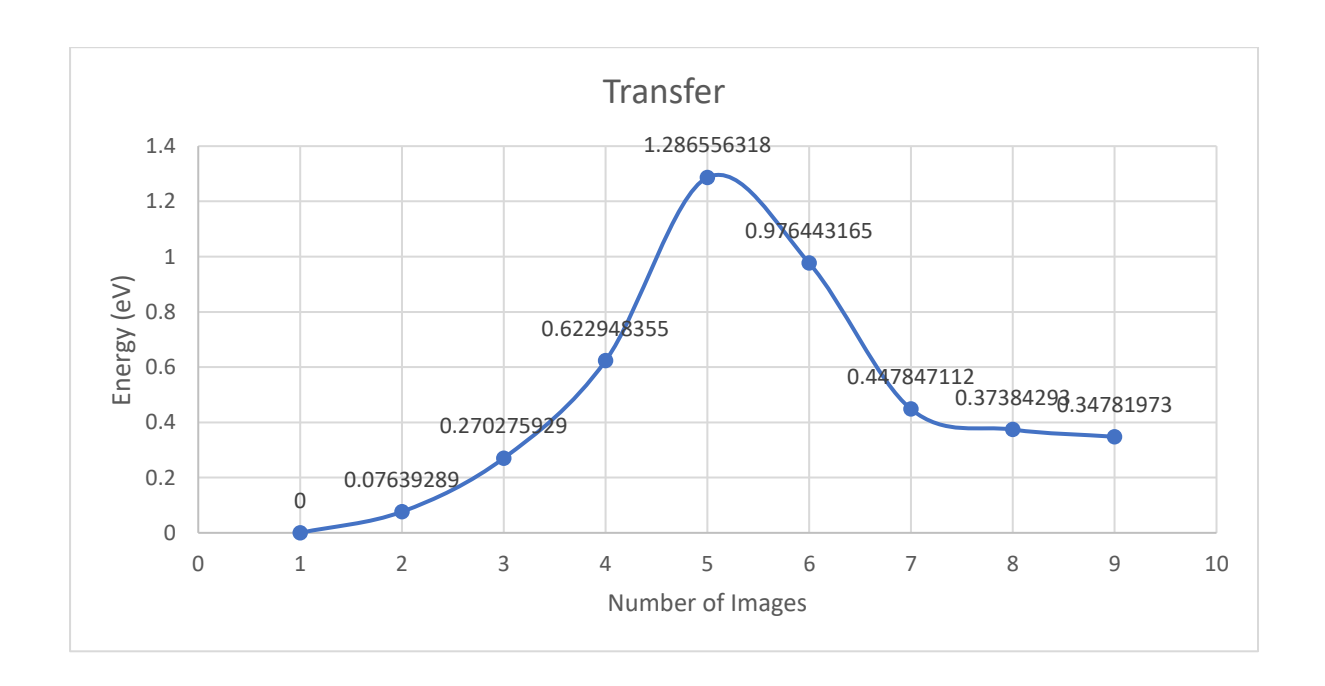


Figure 17: The energy of each image taken by the NEB calculations after optimisation to depict the energy barrier of the process of proton transfer in hydroxyl nest in Chabazite cluster.

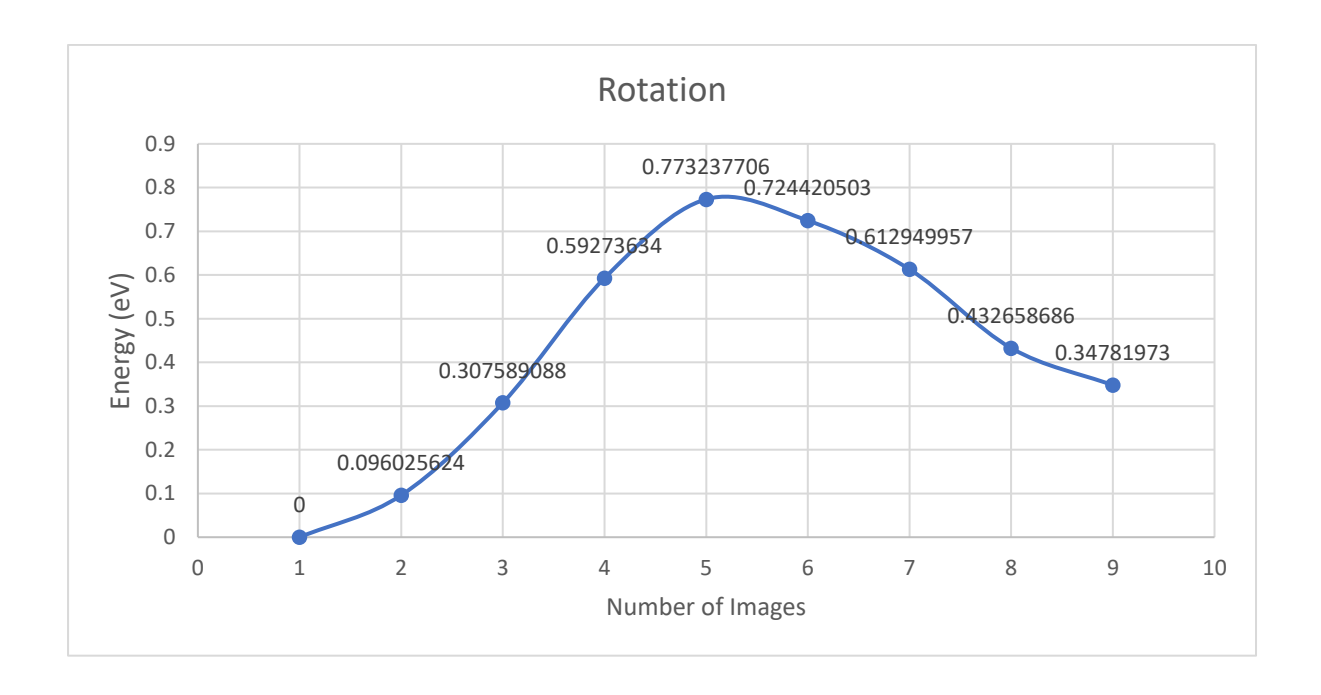


Figure 18: The energy of each image taken by the NEB calculations after optimisation to depict the energy barrier of the process of proton rotation in hydroxyl nest in Chabazite cluster.

For the process of rotation in the hydroxyl nest there is no dissociation required to move the proton to its new position. Therefore, the bond length and energetic reflect the fact as energy and stretching effect is lowered to echo the change. Figure 19 shows the correlation between the bond angles Si-O-H and O-H bond lengths. All bond lengths remained in the expected bond lengths of O-H in zeolites, but a clear pattern is observed that occurs as the proton rotates around the oxygen atom the bond is compressed to facilitate the process. The 5th image once again shows the point when the O-H bond is compressed the most with the sharpest bond angle of 113.63° and smallest bond length of 0.9595 Å. The energy barrier required for the rotation of a proton around a central oxygen is 0.773 eV which is ~40% of the energy barrier of the transfer process.

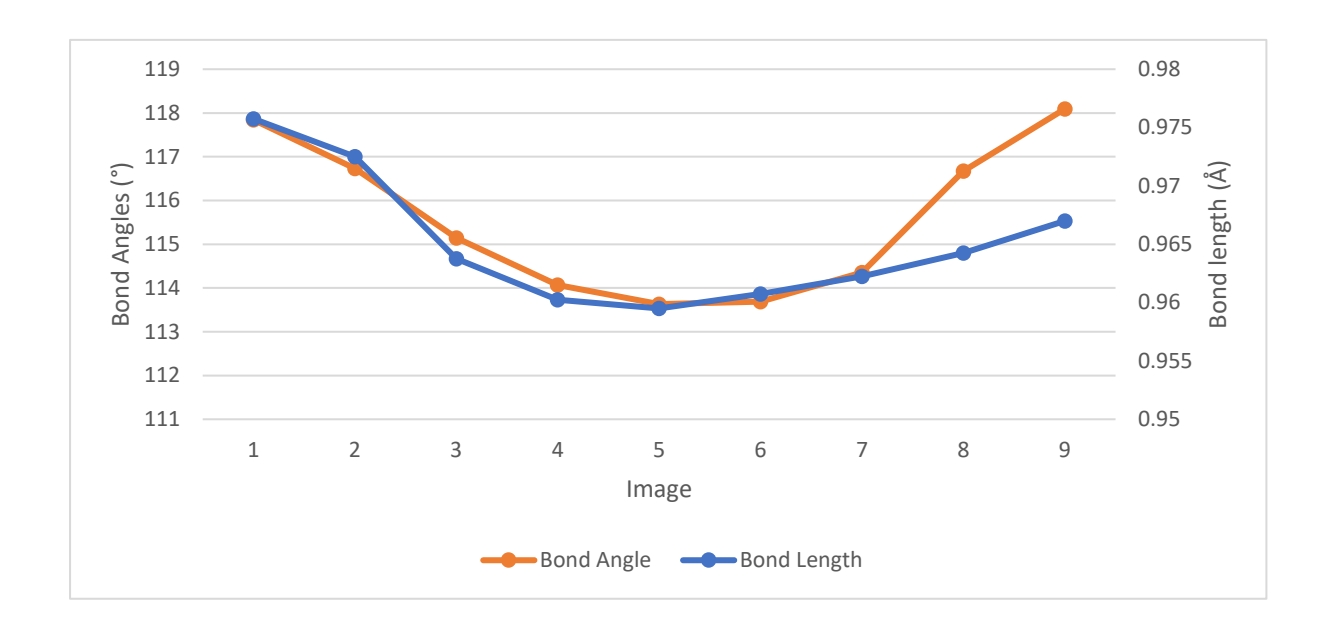


Figure 19: Figure 3.8: Plotting the average change in bond length and bond angle when undergoing NEB calculation in ChemShell for Chabazite hydroxyl nest O-H bond when rotation around oxygen atom.

Our NEB simulations in ChemShell not only confirmed the possible existence of both proton transfer and proton rotation mechanisms within the hydroxyl nest clusters of ZSM-5 but also provided quantitative insights into the energy barriers associated with these processes. These findings are critical for understanding the role of hydroxyl nests in catalytic reactions and ion exchange processes as well as for optimizing zeolite structures for enhanced catalytic performance. The NEB calculation in Python ChemShell have shown a clear preference for the rotation mechanism is Chabazite, however more tests on other frameworks should be undertaken to make more definitive conclusions.

3.5 Summary and Conclusion

The results of the hydroxyl nest defect calculations reveal a general trend of negative energies of formation varying across different zeolite frameworks, with the notable exception of chabazite, which shows a unique behaviour. The energies are negative suggesting that the clusters would dissolve in the presence of water, however the solvation energies of the molecules in water are expected to move this numbers to being the expected exothermic reaction that are observed in experimental. The bond length of the newly formed hydroxyl nest can be interpreted to understand the acidity of the newly formed zeolite with defect. As stronger acids have weaker O-H bonds (longer bonds), as the release of proton can be facilitated more easily. These energy variations are attributed to the structural differences in the hydroxyl nest, particularly the mechanical stability and symmetry of their frameworks. For instance, Faujasite, with its high degree of symmetry and sodalite cages connected by hexagonal prisms, exhibits a lower $\Delta_f H^{\circ}$ compared to other zeolites like Chabazite and α -quartz, both of which have singular T sites but higher energy of defect formation. Our NEB calculations provided an insight into the possibility of movement within the hydroxyl nest through proton transfer or more likely rotation. These results underscore the influence of porosity, framework strength, and structural adaptability on the formation and stability of hydroxyl nests, highlighting how defects can introduce points of weakness in the zeolite structure.

Chapter 4: Mesopore Formation

4.1 Introduction to Mesopore

As previously discussed in Chapters 1 and 3, the main aim of this project is not only to introduce hydroxyl nest into zeolites but to investigate the formation of larger mesopores., which are the hollow spaces or cavities within a solid material, such as zeolites. These pores create a network of channels or voids within the material, allowing molecules, atoms or ions such as platinum to enter, move through, and interact with the zeolite's internal surface. Mesopores are pores with diameters ranging between 2 and 50 nanometres. Additionally, the chapter addresses the Loewenstein rule, which precludes Al-O-Al linkages in zeolite frameworks and provides an overview of the current diversity in natural and synthetic zeolite species, emphasizing the wide range of aluminium contents and their implications for zeolite structure and function.

We shall observe the formation of the mesopores by two mechanisms, the first being the removal of atoms around a central site, using a single location acting as a seed from where the pore will grow out. The second shall involve removing a building block from the framework more specifically the ring within various zeolites. The main clusters observed in the chapter are the same as in chapter 3, ZSM-5, Faujasite, Mordenite, α -quartz and Chabazite.

4.1.1 Computational Approach for ZSM-5

All calculations use the QM/MM approach described in Section 2.X have been selected to show the best possible representation of the growth of mesopores in clusters within the available computer resources the full QM/MM clusters are all 60 Å in diameter and are centred on a Silicon atom which was to be used as the site for the initial defect formation. The outermost 5 Å of the cluster had all atoms frozen in their bulk positions (as determined by prior relaxation using GULP), whilst all other atoms within a radius of 25 Å of the cluster origin were allowed to relax. The size of the clusters are as following X (ZSM-5), X (Faujasite), X (α-quartz) and X (Chabazite). The innermost QM region comprised those atoms described by the all-electron density functional theory calculation and with the QM region of size X (ZSM-5), X (Faujasite), X (α-quartz) and X (Chabazite). Once the first defect site is added the number of atoms in the QM region is increased by 3 atoms (removal of 1 silicon atom and the protonation of oxygen with 4 new hydrogen atoms). The calculations for the QM clusters were performed using the NWCHEM package, while for the MM part, the GULP package was employed, with the Hill-Sauer Molecular Mechanical force-field with some modifications. All modifications to the forcefield are described in detail in section 3.2.

The becke97-2 exchange-correlation functional was used throughout this study due to its good representation of both molecular species and oxides in previous work conducted in the literature.[186, 187] These calculations employed a dual basis set as previously discussed in Section 2.X, with the combination of Def2 triple-zeta valence plus polarization (TZVP) basis set for Si, O and H atoms in the inner most region of the QM atoms. These inner most regions size varies from cluster to cluster however the following was maintained that the most outer T-site layer of atoms was to employ using the weaker Def2 Split valence polarization (SVP).

Loewenstein's rule and Consequences for Mesopore Formation

The calculations presented in the following sections will assume that the QM regions expand progressively from a singular point within the framework. All clusters discussed here, and in subsequent sections, are based on pure silica zeolites. However, in most natural zeolite systems, hydroxyl nests are typically introduced through the removal of aluminium atoms from the framework.[187] According to Loewenstein's Rule, a fundamental principle in zeolite chemistry, aluminium (Al) atoms should not be directly bonded to one another via oxygen atoms. This means that Al-O-Al linkages are avoided in favour of Al-O-Si linkages. The rationale behind this rule is that adjacent aluminium atoms create an energetically unfavourable structure due to the charge imbalance, due to the energetics of small clusters from which zeolites nucleate.

To simulate more realistic conditions, a ZSM-5 cluster was designed to include two hydroxyl nests, ensuring a silicon T-site remains between them, in accordance with Loewenstein's Rule. This model closely approximates natural conditions, where the formation of hydroxyl nests occurs through aluminium extraction and allows for more accurate calculations of defect behaviour within the zeolite framework (see Figure 20). The calculation will once again be with respect to the removal of orthosilic acid (Si(OH)₄) with four water molecules in a vacuum.

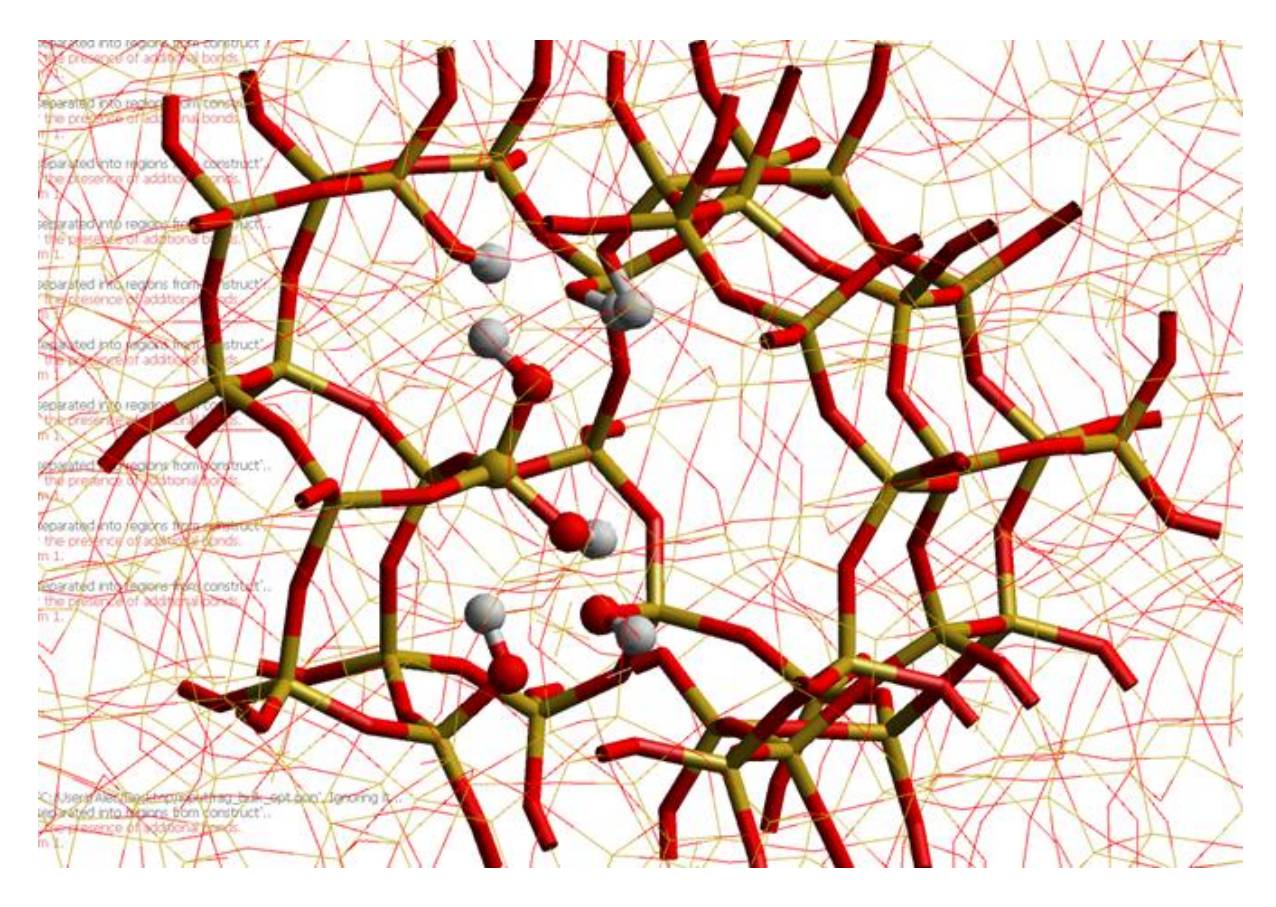


Figure 20: Figure 4.1: The atomical structure of optimised ZSM-5 hydroxyl nest defect with 2 hydroxyl nest defects surrounding a central Si(OH)₂ to simulate the removal of 2 aluminium atoms following the Loewenstein's rule.

Beginning with the central silicon atom and its two coordinating oxygen atoms, the Si–O bond lengths are measured at 1.618 Å and 1.610 Å, respectively. The corresponding O–H bond lengths are both identical at 1.080 Å, with the hydrogen atoms forming hydrogen bonds to a single oxygen atom, which is part of the four-membered ring system described in Chapter 3.1 The bond angles are 111.23° and 109.55° which remain within the expected range for this cluster. Despite the framework providing significant 'free' space within the channels, the hydrogen atoms preferentially remain within the hydrogen-bonded ring. This configuration enhances the structural stability of the framework, preventing collapse at the defect sites.

Upon examining the energy of the system, we compared the current cluster, which adheres to Loewensteinian structures, with a theoretical cluster where the adjacent T-site is removed which will be discussed in more detail in the next section. Our results indicate that the cluster following Loewenstein's rule exhibits a higher energy by 0.3144 eV compared to the alternative. This suggests that the cluster adhering to Loewenstein's rule is thermodynamically less stable than the theoretical counterpart, which will be discussed in greater detail in the following section. The higher energy of the Loewenstein-compliant cluster implies that the system favours a lower-energy configuration, raising the possibility that this cluster could undergo rearrangement to form a structure with two adjacent defect sites.

The additional strain and distortion within the catalytic site, introduced by the increased defect size, probably contribute to the destabilization of the cluster compared to the cluster with adjacent removed T-sites. However, due to the current limitations in the ChemShell code and computational resources available for this work, conducting a comprehensive molecular dynamics study to explore the rearrangement process is beyond the scope of this thesis. Such a study might be helpful in revealing the mechanisms of hydroxyl nest and mesopore formation, as well as identifying the key transition states and kinetic barriers that must be overcome for the system to reach its more thermodynamically stable state; although if the barriers are significantly great than thermal energies metadynamical methods would probably be necessary. Future research in this area is crucial for understanding the dynamic behaviour of these defects and their role in zeolite frameworks.

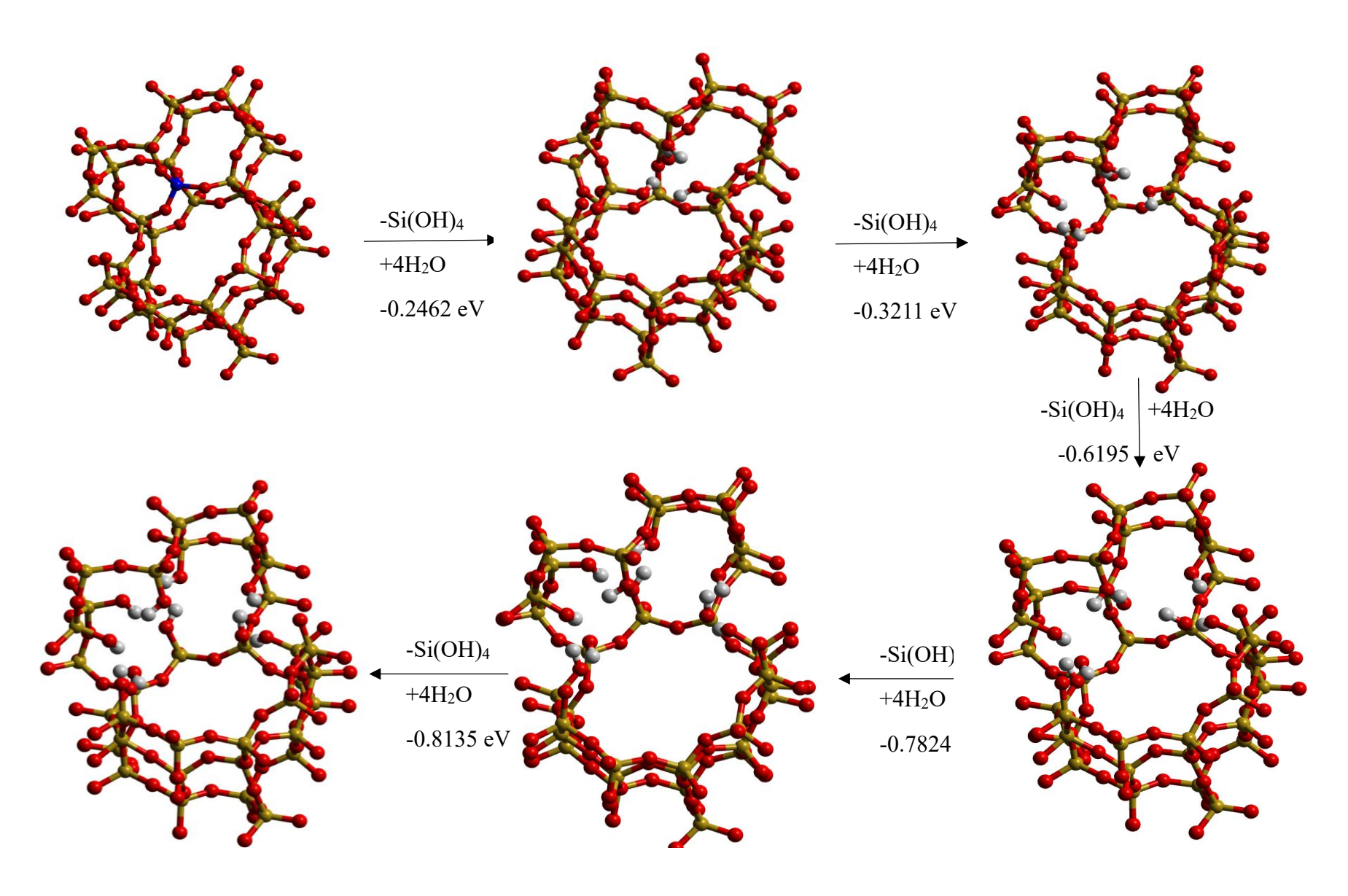
4.2 Mesopore Formation in ZSM-5: A Computational Study

Having previously explored the fundamental aspects of hydroxyl nest formation and the underlying mechanisms within different zeolite frameworks, we now turn our focus to ZSM-5. Unlike other zeolites, ZSM-5 has a unique system of intersecting microporous channels, which makes it an ideal candidate for processes requiring both shape selectivity and diffusion control. However, the inherent limitations of its microporous structure can restrict access to larger molecules, leading to the need for mesopore formation. We will discuss the strategies and mechanisms involved in inducing mesoporosity in ZSM-5, focusing on the role of hydroxyl nest defects and the controlled systematic removal of framework atoms. Additionally, we will explore how the introduction of mesopores enhances the material's catalytic performance with the increased size of the channels allowing for larger catalyst to embed themselves in the framework.

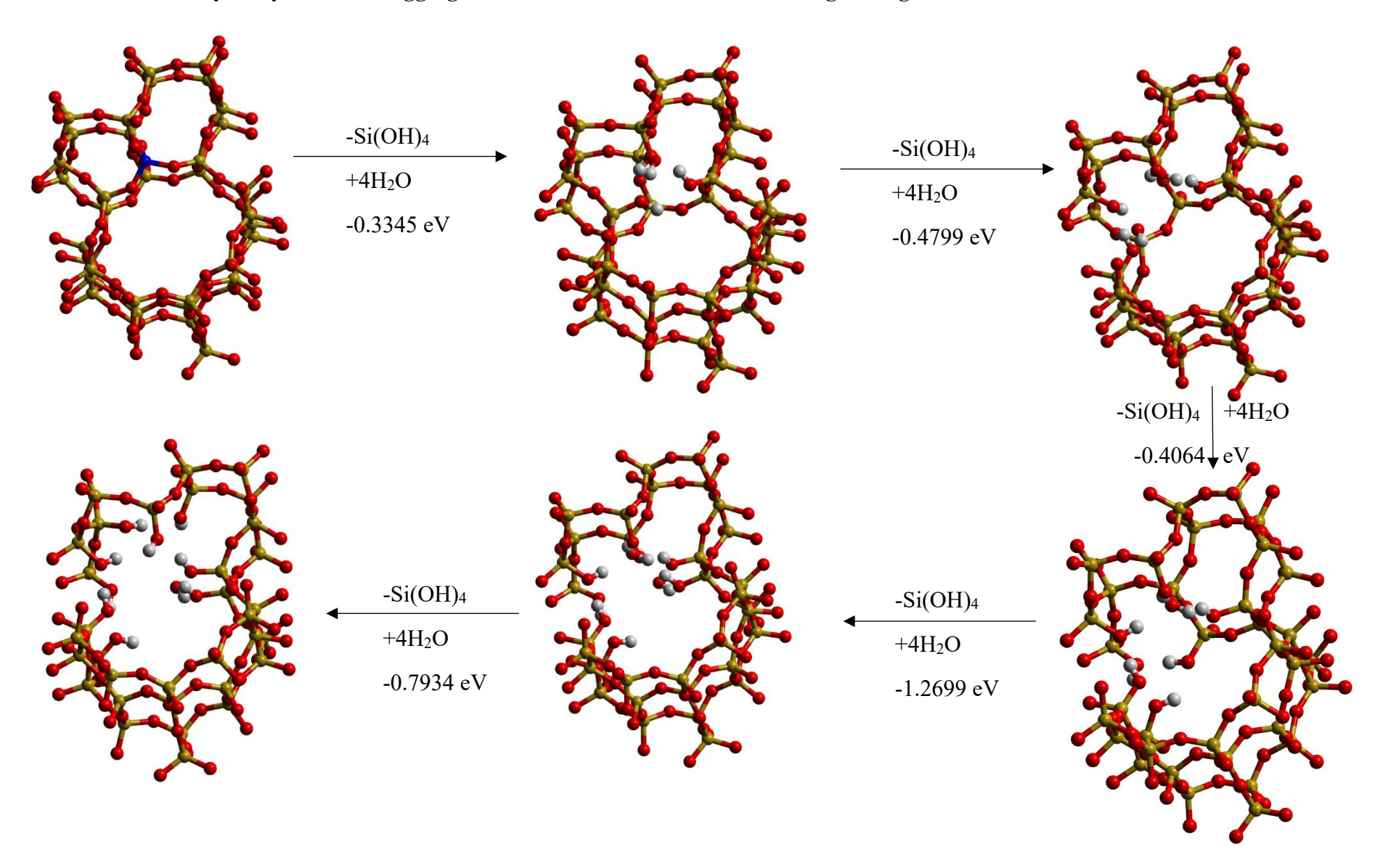
By examining the formation of mesopores in ZSM-5, we aim to provide a comprehensive understanding of how structural modifications can be engineered to overcome the intrinsic limitations of microporous frameworks while maintaining the stability, functionality and viability of ZSM-5.

The formation of the can be achieved by using two differing paths as depicted below:

Hydroxyl Nest Site Aggregation Formation in ZSM-5 in the Adjacent Configuration



Hydroxyl Nest Site Aggregation Formation in ZSM-5 in the Ring Configuration



The visualized atomic configurations of optimised ZSM-5 cluster illustrated above show the mechanisms that will be explored in this chapter.

- 1. The removal of adjacent sites; the selective removal of framework atoms from adjacent tetrahedral sites creates larger voids in the structure.
- 2. The Removal of a five membered ring structures from the ZSM-5 framework. By eliminating these rings, the integrity of the framework is modified, leading to the creation of larger pores by opening the zeolitic cages in the framework.

The generation of mesopores in ZSM-5, ranging from 3 to 8 nm, has been successfully achieved using the organic structure-directing agent 3-(trimethoxysilyl)-propylhexadecyldimethylammonium chloride during the synthesis of MFI zeolite [188]. However, from a theoretical and, more crucially, computational perspective, the mechanisms underlying the formation of these mesopores have not been thoroughly investigated, leaving the precise reaction pathways poorly understood.

In this study, we computationally modelled the formation of ZSM-5 clusters with varying mesopore sizes by removing specific T-sites, utilizing hybrid functionals with def2-TZVP and def2-SVP basis sets. Starting from an unmodified parent ZSM-5 framework, we generated distinct embedded clusters centred on a tetrahedral silicon atom (T-site), which is located within an active site at the intersection of the straight and sinusoidal channels. All relevant active site components, including neighbouring Si atoms and linking oxygen atoms within the first and second coordination spheres, were incorporated into the QM zone surrounding the central T-site, as depicted in visualized atomic configurations. To preserve the structural integrity of the channels, a large ring around the straight channels was included in the model, as understanding the framework's stability during pore expansion was a primary objective. The cluster size was carefully maintained to include a sufficient layer of T-sites neighbouring the mesopore after the

removal of five T-sites. The QM region of cluster contained 155-158 atoms previously discussed in the computational approach section.

4.2.1 Mesopore Formation via T-site Removal in Adjacent Positions

The results from the optimization of ZSM-5 mesopores are presented in Table 3. Our calculations indicate that all reactions are exothermic, with energy release increasing as the mesopore size expands. As discussed in the previous section, when the hydroxyl nest is expanded to include two T-sites, the formation energy is -0.32 eV, corresponding to an approximate 30% increase in energy release. The original T-site adopts a configuration resembling a three-membered hydrogen-bonded ring, as shown in Section 3.2. The removal of the fourth silanol group results in the hydroxyl nest adopting the second most stable structural configuration to maintain mesopore stability. However, the newly formed secondary hydroxyl nest within the mesopore does not conform to the typical structure of isolated nest sites. Instead, two silanol groups form a hydrogen-bonded chain, linking all three silanol groups in the nest, with the final silanol extending into the channel at an angle of 115.08°. This is an unexpected result, as prior observations with more constrained space consistently showed the hydrogen atoms preferring to remain bonded to oxygen atoms within the framework. The O-H bond lengths are within the range of 0.957-0.986 Å, and the Si-O-H bond angles fall between 115.08° and 121.74°, all within expected values for these bonds as shown in Table 4 and 5.

Table 3: The standard enthalpy of formation of ZSM-5 cluster in the adjacent configuration. ΔHf° calculated relative to the pure silicious ZSM-5.

ZSM-5 cluster	Reactant (a.u.)	ΔH_{f}° (eV)
Normal	-19167.0522	N/A
1 Hydroxyl nest	-18879.7315	-0.24617953
2 Hydroxyl nest	-18515.9673	-0.32113549
3 Hydroxyl nest	-18152.2140	-0.61948814
4 Hydroxyl nest	-17788.4524	-0.78243443
5 Hydroxyl nest	-17424.6908	-0.81354241

Table 4: The results from the optimisation of a singular hydroxyl nest in ZSM-5 showing the bond length (Å) and bond angle (°) of each individual silanol within the mesopore.

Singular Hydroxyl nest	Bond Length (Å)	Bond Angles (°)	Hydrogen Bond Length (Å)
Silanol A	0.965	120.108	2.873
Silanol B	0.981	110.643	2.019
Silanol C	0.969	122.088	1.887
Silanol D	0.975	119.726	1.752

Table 5: The results from the optimisation of two adjacent hydroxyl nest in ZSM-5 showing the bond length (\mathring{A}) and bond angle $(^{\circ})$ of each individual silanol within the mesopore.

Two Hydroxyl nest	Bond Length (Å)	Bond Angles (°)	Hydrogen Bond Length (Å)
Silanol Ring 1			
Silanol A	0.966	119.877	1.846
Silanol B	0.969	121.739	1.819
Silanol C	0.957	115.082	1.872
Silanol Ring 2			
Silanol A	0.986	119.733	1.702
Silanol B	0.972	115.779	1.767
Silanol C	0.967	116.101	1.895

Introducing a third defect results in a substantial increase in energy release, approximately 40%. This significant energy change may be attributed to the improper formation of the two-hydroxyl nest cluster. Upon examining the three-hydroxyl nest structure, the hydrogen-bonded chain is replaced by the reformation of a three-membered hydrogen-bonded ring. This configuration could represent a local energy minimum, as re-optimisation of the two-hydroxyl nest cluster with the three-membered ring still resulted in the structure adopting the chain configuration, as previously described. Based on the cumulative energy changes for mesopore formation, shown in Figure 21, we observed that the energy for the two-hydroxyl nest cluster is more exothermic in the ring configuration when compared to the adjacent formation.

Additional testing with improved basis sets is required to determine if the observed behaviour is an anomaly due to the limitations of the current model.

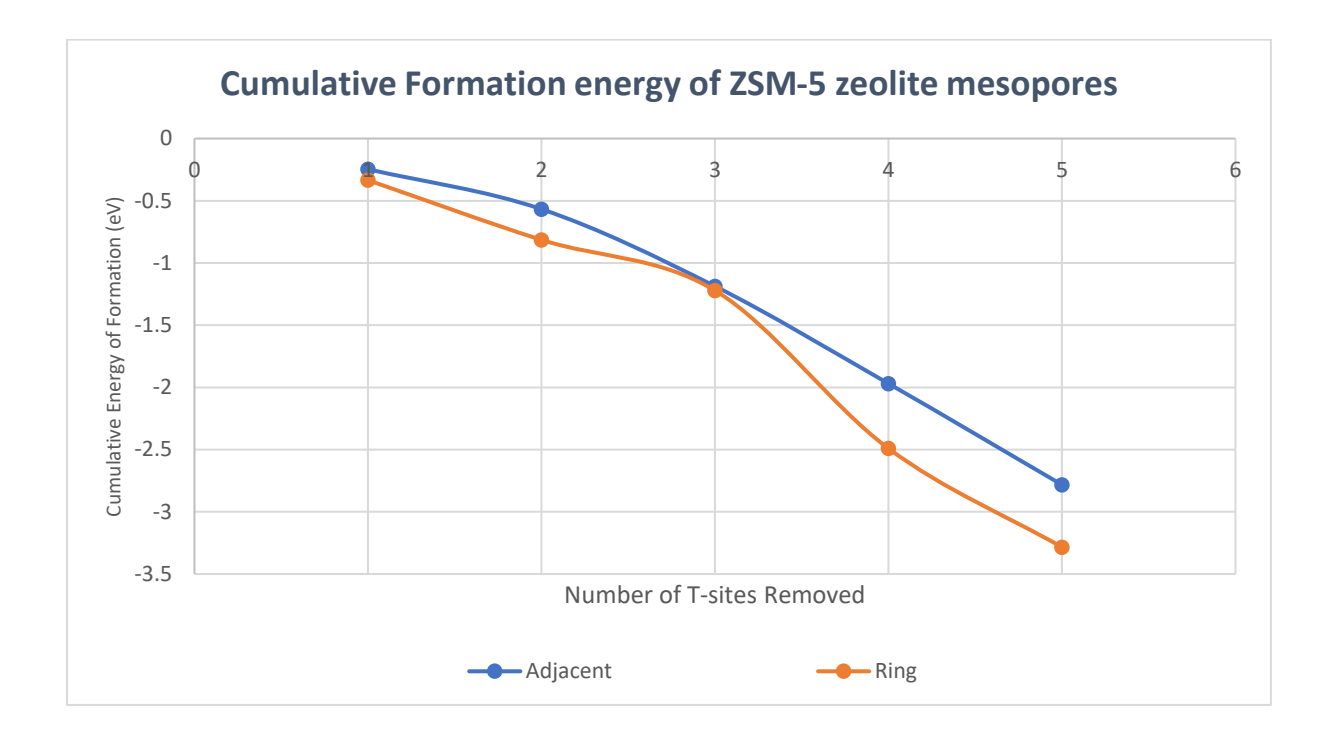


Figure 21: Cumulative formation energy of ZSM-5 mesopores with respect to the number of silicon T-sites remove to energy (eV) to remove an additional T-site. The blue line depicting the adjacent configuration and comparing to the ring configuration in orange.

On the other hand, the original central T-site now has only two silanol groups. One of these silanol groups forms a hydrogen bond with the other; however, they do not adopt the configuration typically observed in α-quartz, where two silanol groups bond to create a small square ring. Instead, due to the increased spatial availability, the secondary hydrogen bond occurs between one of the other three-membered hydrogen-bonded rings. The hydrogen bond length is notably longer compared to the ringed members, measuring 2.541 Å. This ample space permits this interaction, allowing the remaining hydrogen bond to adopt a more optimal bond length, similar to other bonds of this type, at 1.879 Å. All O-H bond lengths within the new

mesopore fall between 0.960 Å and 0.986 Å, and the bond angles range from 113.70° to 120.14° as shown in Table 6.

Table 6: The results from the optimisation of three adjacent hydroxyl nest in ZSM-5 showing the bond length (\mathring{A}) and bond angle $(^{\circ})$ of each individual silanol within the mesopore.

Three Hydroxyl nest	Bond Length (Å)	Bond Angles (°)	Hydrogen Bond Length (Å)
Silanol Ring 1			
Silanol A	0.975	113.697	1.768
Silanol B	0.968	114.724	1.885
Silanol C	0.980	118.894	1.756
Silanol Ring 2			
Silanol A	0.966	119.233	1.832
Silanol B	0.972	115.093	1.643
Silanol C	0.987	117.402	1.993
Silanol Pair			
Silanol A	0.960	117.244	2.541
Silanol B	0.969	120.136	1.879

This lone silanol group hydrogen bonds to the nearest three-membered hydrogen-bonded ring with a bond length of 2.317 Å, which is shorter than the distance observed in the cluster with three hydroxyl nests. The absence of the influence from a secondary silanol group allows this remaining group to shift closer to another silanol ring within the framework. The rest of the framework consists of three stable three-membered hydrogen-bonded rings. Consequently, the energy of the framework decreases by 0.7824 eV, indicating that the stability of the framework is maintained with the introduction of additional hydrogen-bonded rings. All O-H bond lengths are between 0.963 Å and 0.981 Å, with bond angles ranging from 110.07° to 118.56° as shown in Table 7.

Table 7: The results from the optimisation of four adjacent hydroxyl nest in ZSM-5 showing the bond length (\mathring{A}) and bond angle (°) of each individual silanol within the mesopore.

Four Hydroxyl nest	Bond Length (Å)	Bond Angles (°)	Hydrogen Bond Length (Å)
Silanol Ring 1			
Silanol A	0.974	114.778	1.774
Silanol B	0.968	115.498	1.849
Silanol C	0.978	119.651	1.802
Silanol Ring 2			
Silanol A	0.963	112.326	2.146
Silanol B	0.969	121.115	1.914
Silanol C	0.973	110.074	1.871
Silanol Ring 3			
Silanol A	0.967	118.326	1.956
Silanol B	0.972	118.558	1.814
Silanol C	0.981	114.715	1.682
Lone Silanol			
Silanol A	0.960	117.877	2.317

The removal of the final hydroxyl nest completely eliminates the silanol groups associated with the original hydroxyl defect, allowing the framework to stabilize with four three-membered hydrogen-bonded rings. The final energy change results in a further reduction of 0.8135 eV, facilitated by the formation of additional silanol rings. O-H bond lengths in the final structure range from 0.966 Å to 0.987 Å, with bond angles between 112.43° and 119.76° as shown in Table 8.

Table 8: The results from the optimisation of five adjacent hydroxyl nest in ZSM-5 showing the bond length (\mathring{A}) and bond angle $(^{\circ})$ of each individual silanol within the mesopore.

Five Hydroxyl nest	Bond Length (Å)	Bond Angles (°)	Hydrogen Bond Length (Å)
Silanol Ring 1			
Silanol A	0.972	114.742	1.762
Silanol B	0.970	115.528	1.889
Silanol C	0.980	119.699	1.812
Silanol Ring 2			
Silanol A	0.963	110.546	2.151
Silanol B	0.967	122.246	1.909
Silanol C	0.983	112.674	1.864
Silanol Ring 3			
Silanol A	0.967	118.326	1.956
Silanol B	0.972	118.558	1.814
Silanol C	0.981	114.715	1.682
Silanol Ring 4			
Silanol A	0.959	110.673	1.975
Silanol B	0.967	121.832	1.748
Silanol C	0.982	118.123	1.834

To conclude, our computational study on the formation of ZSM-5 clusters with varying mesopore sizes, based on the removal of adjacent T-sites, has shown that the formation energies are exothermic and increase with the expansion of the mesopores. The structural analysis reveals that the stability of the framework is maintained through the formation of hydrogen-bonded silanol groups, especially as more T-sites are removed. As mesopores grow, new hydrogen-bonding arrangements emerge, with the system adopting different configurations to preserve framework integrity as much as possible. The observed shifts in energy are likely tied to these structural changes, and while our results align with expectations, further optimisation with improved basis sets is needed to confirm the behaviour of some defects and their potential stability.

4.2.2 Mesopore Formation via T-site Removal in Ring Positions

Moving on to the formation of mesopores through the removal of T-sites from a five-membered silicon ring, the process involves the sequential removal of adjacent T-sites around the ring, beginning with the T-site closest to the original central T-site. The cluster remains consistent with the previously discussed adjacent ZSM-5 cluster; however, in this case, the atoms in the QM1 region (described with the def2-TZVP basis set) are selected around a five-membered ring, rather than adjacent to the starting T-site.

The results from the optimisation are shown in Table 9 shown below:

Table 9: The standard enthalpy of formation of ZSM-5 cluster in the ring configuration. $\Delta_f H^{\circ}$ calculated relative to the pure silicious ZSM-5 cluster.

ZSM-5 cluster	Reactant (a.u.)	ΔH _f ° (eV)
Normal	-19167.2609	N/A
1 Hydroxyl nest	-18879.9323	-0.33448986
2 Hydroxyl nest	-18516.1740	-0.47992077
3 Hydroxyl nest	-18152.4129	-0.40635479
4 Hydroxyl nest	-17788.6835	-1.26990514
5 Hydroxyl nest	-17424.9367	-0.79343753

The formation of the first hydroxyl nest once again yields similar results to the adjacent cluster, with no significant deviations. The energy of cluster formation is lower, measured at -0.3345 eV. While the system's energy differs due to the altered QM1 region, a similar trend is observed.

The O-H bond lengths fall within the range of 0.959–0.972 Å, and the bond angles are between 118.72° and 129.06° as shown in Table 10.

Table 10: The results from the optimisation of a singular hydroxyl nest in ZSM-5 showing the bond length (\mathring{A}) and bond angle (°) of each individual silanol within the mesopore.

Singular Hydroxyl nest	Bond Length (Å)	Bond Angles (°)	Hydrogen Bond Length (Å)
Silanol A	0.972	120.307	1.798
Silanol B	0.959	129.064	2.188
Silanol C	0.961	118.722	1.945
Silanol D	0.960	120.516	1.995

Upon introducing a second hydroxyl nest, the cluster configuration results in the formation of two perfect three-membered hydrogen-bonded rings. This further supports the need for additional investigation into the defects observed in the adjacent model. However, the energy required to remove an additional T-site is higher than previously recorded, with the energy jump increasing by a comparable factor to that observed in the adjacent cluster. The energy change associated with the removal of the second T-site is -0.4799 eV, representing an ~40% increase, similar to the adjacent cluster. The energy increase required to remove the second T-site is -0.1454 eV more than that for the first T-site, compared with 0.0749 eV for the adjacent cluster. This doubling in energy between the clusters can be attributed to two potential factors: firstly, the distinct nature of the cluster due to the different QM1 region, and secondly, the possibility of a local minimum being discovered during optimization of the two adjacent hydroxyl nest clusters. The correct energy difference should align with the expected values for the ring ZSM-5 cluster as they have the same structure however have different QM regions in the calculations. The O-H bond lengths range from 0.966 to 0.983 Å, with bond angles between 117.36° and 123.69° as shown in Table 11.

Table 11: The results from the optimisation of two hydroxyl nest in ZSM-5 in the ring configuration showing the bond length (\mathring{A}) and bond angle $(^{\circ})$ of each individual silanol within the mesopore.

			Hydrogen Bond Length
Two Hydroxyl nest	Bond Length (Å)	Bond Angles (°)	(Å)
Silanol Ring 1			
Silanol A	0.984	119.841	1.725
Silanol B	0.966	117.363	1.865
Silanol C	0.972	114.516	1.787
Silanol Ring 2			
Silanol A	0.967	123.692	1.998
Silanol B	0.969	123.132	1.765
Silanol C	0.968	112.055	1.983

The removal of the third T-site results in a framework that closely resembles the adjacent cluster, featuring two three-membered hydrogen-bonded rings, with the two central silanol groups forming a chain to the nearest hydrogen-bonded ring. The energy change associated with this removal is -0.4063 eV, marking the first notable deviation in energy compared to the adjacent clusters. It becomes more challenging to remove an additional T-site from the ring, even though the mesopore structure remains consistent. This increased difficulty can be attributed to the strain on the framework, as atoms are now being removed from the sinusoidal channel rather than one of the rings in the straight channel. Despite this strain, the O-H bond lengths remain consistent between 0.964 and 0.981 Å, and the bond angles are within the range of 110.84° to 123.06° as shown in Table 12.

Table 12: The results from the optimisation of three hydroxyl nest in ZSM-5 in the ring configuration showing the bond length (\mathring{A}) and bond angle $(^{\circ})$ of each individual silanol within the mesopore.

			Hydrogen Bond Length (Å)
Three Hydroxyl nest	Bond Length (Å)	Bond Angles (°)	
Silanol Ring 1			2.051
Q'1 1 1	0.064	101 (51	2.051
Silanol A	0.964	121.654	1 002
G'1 1 D	0.064	100.055	1.883
Silanol B	0.964	123.057	1 (20
Silanol C	0.001	112 470	1.638
Silanoi C	0.981	112.478	
Silanol Ring 2			
Shahoi King 2			2.006
Silanol A	0.968	119.178	2.000
Situation 14	0.700	117.170	1.813
Silanol B	0.971	110.840	
	V.2 (2		1.790
Silanol C	0.975	119.297	
Silanol Pair			
			1.690
Silanol A	0.978	120.651	
			2.065
Silanol B	0.967	116.366	

When the fourth T-site is removed, the cluster's structure changes significantly. The energy change for this T-site removal is considerable: 1.270 eV, representing a sharp increase. The new cluster consists of two three-membered hydrogen-bonded rings and two silanol chains. One of these silanol chains forms a hydrogen bond with the nearest hydrogen-bonded ring, with a bond length of 2.024 Å. In contrast, the other silanol chain is not hydrogen-bonded to the closest ring, and its distance from the nearest oxygen atom is 4.088 Å—beyond the maximum range for a typical hydrogen bond in zeolites. As a result, this interaction is negligible, primarily governed by van der Waals forces. Despite these changes, the O-H bond lengths remain within

0.960–0.980 Å, and the bond angles are within the acceptable range of 110.33° to 124.72° as shown in Table 13.

Table 13: The results from the optimisation of four hydroxyl nest in ZSM-5 in the ring configuration showing the bond length (\mathring{A}) and bond angle $(^{\circ})$ of each individual silanol within the mesopore.

Four Hydroxyl nest	Bond Length (Å)	Bond Angles (°)	Hydrogen Bond Length (Å)
Silanol Ring 1			
Silanol A	0.969	119.649	1.979
Silanol B	0.975	119.540	1.781
Silanol C	0.969	110.332	1.861
Silanol Ring 2			
Silanol A	0.977	119.024	1.782
Silanol B	0.974	115.870	1.884
Silanol C	0.960	123.890	2.287
Silanol Pair 1			
Silanol A	0.965	124.723	1.758
Silanol B	0.960	115.831	4.088
Silanol Pair 2			
Silanol A	0.980	121.000	1.682
Silanol B	0.967	116.633	2.024

The removal of the fifth and final T-site results in the loss of the stable three-membered hydrogen-bonded rings, leading to the formation of five pairs of silanol groups surrounding the mesopore. Both types of silanol pairs observed in previous clusters are present in this new configuration. All silanol groups attempt to form hydrogen bonds with oxygen atoms that were part of the removed T-site (with close interactions characterized by hydrogen bonds less than 2 Å), while secondary hydrogen bonds form between silanol groups within the same pentasil units, involving longer-range interactions over 2 Å. Any remaining silanol groups that do not have defects in their rings are located beyond 3.6 Å from other groups, as the structure of the

framework allows these silanol groups to extend into the straight channels without any interactions pulling them back into the framework. The results all the bond lengths and bond angles are tabulated in Table 14.

Table 14: The results from the optimisation of five hydroxyl nest in ZSM-5 in the ring configuration showing the bond length (\mathring{A}) and bond angle $(^{\circ})$ of each individual silanol within the mesopore.

Five Hydroxyl nest	Bond Length (Å)	Bond Angles (°)	Hydrogen Bond Length (Å)
Silanol Pair 1			
Silanol A	0.969	122.658	2.025
Silanol B	0.959	117.593	2.705
Silanol Pair 2			
Silanol A	0.964	121.046	2.167
Silanol B	0.962	113.295	2.726
Silanol Pair 3			
Silanol A	0.964	123.649	1.765
Silanol B	0.961	115.028	4.216
Silanol Pair 4			
Silanol A	0.979	122.488	1.715
Silanol B	0.964	112.295	2.252
Silanol Pair 5			
Silanol A	0.968	121.223	1.895
Silanol B	0.959	115.254	2.705

The formation energy of this cluster is -0.7934 eV, indicating an increase in the energy required for the removal of additional hydroxyl nests. We can speculate that as more rings are removed, the energy demand will continue to rise will removing subsequent T-site, as the framework will experience increasing strain with the removal of additional atoms. However, due to the high computational cost associated with larger quantum mechanical (QM) regions, extending these calculations beyond this point is not feasible in this thesis. We can further speculate that

continued removal of rings will eventually lead to the collapse of the framework, rendering it structurally unstable as the zeolite framework isn't known to dissolve in the presence of water.

To summarise, we have investigated the formation of mesopores in ZSM-5 by removing T-sites from two distinct configurations: adjacent sites and a five-membered ring. Both methods revealed exothermic formation energies, though the magnitude and structural adaptations differed. In the adjacent configuration, the formation of stable three-membered hydrogen-bonded rings played a crucial role in maintaining the structural integrity of the mesopores. The five-membered ring configuration, show that the pair of silanol group have a produce lower in energy clusters. The largest energy jump occurred when four T-sites were removed from the five-membered ring, reflecting a critical point in framework stability where non-hydrogen-bonding interactions began to increase.

Interestingly, while the energy trends were like those observed in the adjacent cluster model, the deviations seen in the ring structure, particularly with the formation of silanol chains and weakening of hydrogen-bond interactions, suggest that different pore formation pathways impose varying structural strains, which is especially evident when comparing the jump in energy between the third and fourth defects, where the ring structure displayed significantly less strain.

Overall, the study suggests that increasing mesopore size by removing T-sites leads to higher energy demands and slowly destabilises the framework because of the loss of T-sites, particularly in the five-membered ring configuration reduce the energy of formation. This stability decrease will arise from the lack of strong covalent bond and replacing them with weaker hydrogen bond. However, all results remain exothermic in nature encouraging the formation of more pores. These findings highlight the need for further refinement and testing

with larger QM regions to capture the strain effects and potential collapse of the framework at larger pore sizes.

4.3 Mesopore Formation in Chabazite: A Computational Study

In this section, we transition from the study of ZSM-5 to chabazite (CHA), another important zeolite framework with distinct structural characteristics. While ZSM-5 features a complex interconnection of straight and sinusoidal channels, chabazite has a more compact structure with large cages interconnected by small windows, resulting in a different pore architecture and diffusion behaviour. These differences can have a significant impact on the formation of mesopores and the stability of hydroxyl nest defects. As with ZSM-5, understanding the removal of T-sites and the resulting mesopore formation in chabazite is crucial for tailoring its catalytic properties. Here, we will investigate mesopore formation in chabazite, focusing on the energetic and structural changes upon the removal of T-sites, and comparing the results to those obtained for ZSM-5.

We computationally modelled the formation of mesopores in chabazite by selectively removing specific T-sites, using hybrid functionals with def2-TZVP and def2-SVP basis sets. Beginning with the unmodified parent chabazite framework, we generated distinct embedded clusters cantered around a tetrahedral silicon atom (T-site) positioned at a key active site within the framework. This T-site is located at the intersection of chabazite's characteristic large cages and small windows, which plays a critical role in the structural evolution during mesopore formation.

All relevant components of the active site, including the neighbouring silicon atoms and the linking oxygen atoms in both the first and second coordination spheres, were incorporated into

the quantum mechanical (QM) zone surrounding the central T-site, as illustrated in depiction pathways displayed in section 4.3.1. To ensure the structural integrity of the model during mesopore expansion, a large ring encircling the chabazite's cage windows was included, which allowed us to examine the stability of the framework as mesopores expanded due to the systematic removal of T-sites. The cluster size was carefully calibrated to maintain a sufficient number of neighbouring T-sites (1 complete layer of adjacent T site for each atom T site planned to be removed) around the mesopore, particularly after the removal of five T-sites, ensuring a realistic representation of the framework's stability. The quantum mechanical region (QM1) of the cluster, comprising 144 atoms, was selected following the approach outlined in the earlier methodology methods section to balance computational efficiency with the accuracy required for capturing the effects of pore expansion on the structural and energetic properties of the chabazite framework.

4.3.1 Mesopore Formation via T-site Removal in Adjacent Positions

The visualized atomic configurations of optimised CHA cluster illustrated below show the methods that will be explored during this section. Removal of five adjacent T-sites in chabazite opens up the cages present in the framework proving a large open area to allow catalytic species to sit within the framework. These cages with a diameter of ~7.3 Å are the key building blocks for the chabazite framework.

The results for the optimisation of chabazite with different size mesopores are displayed in Table 15. The results from optimisation paint a similar picture to that observed with ZSM-5 clusters: the first removed T-sites are the less exothermic, the initial cost of breaking the framework is endothermic rather than exothermic as shown in subsequent removal of orthosilic

acid. As the subsequent T-sites are removed from the cluster the energy changes are more exothermic leading to the formation larger and larger mesopores. The energy suggests that once the hurdle of the first T-site is removed that the system will more favourably expand the clusters leading to the large mesopores observed in the literature as discussed in our introduction. The cumulative energies of the mesopores formation show a similar energetic pattern between the energies of both the adjacent and the ring configuration as depicted in Figure 22.

Hydroxyl Nest Site Aggregation Formation in Chabazite in the Adjacent Configuration

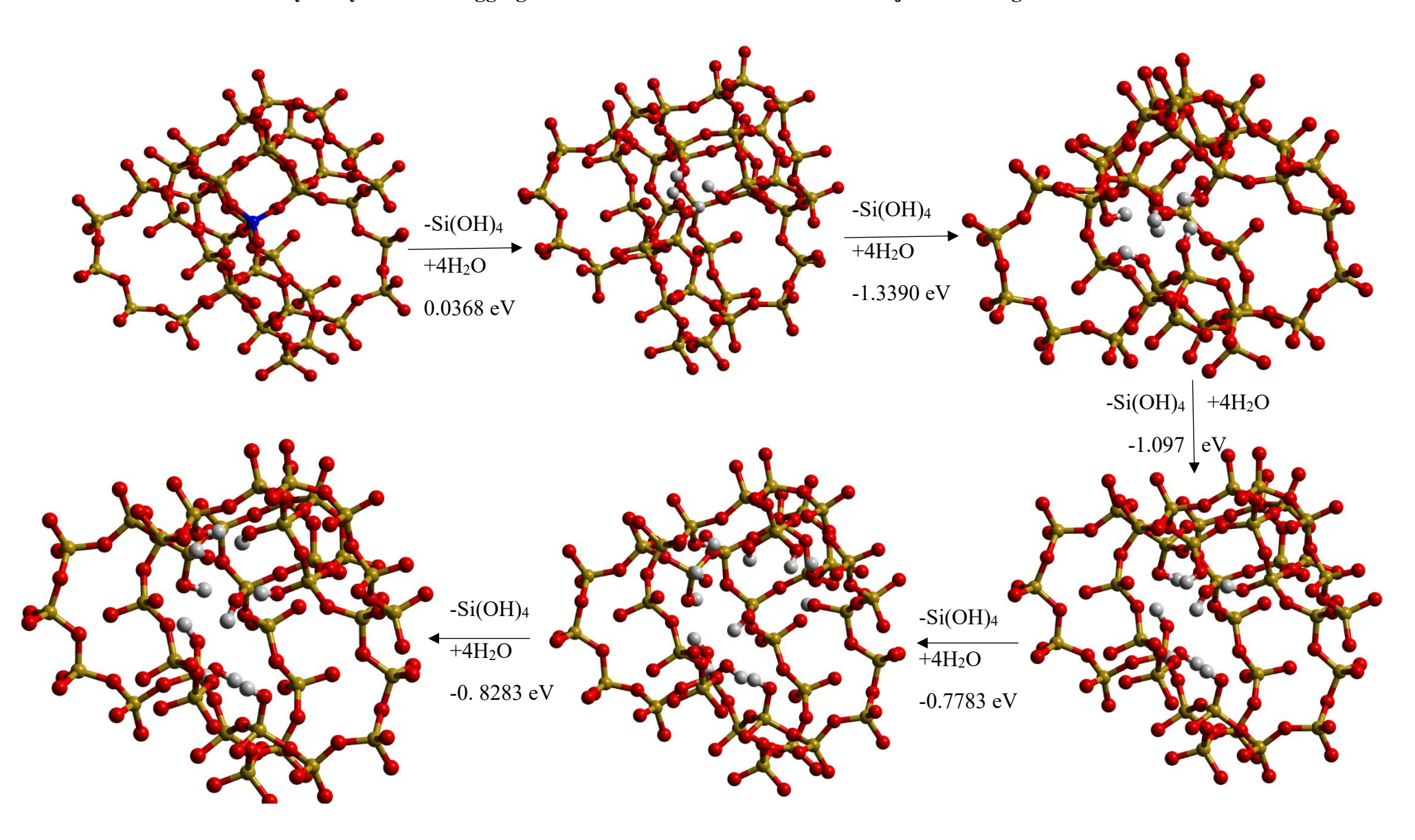


Table 15: The standard enthalpy of formation of Chabazite cluster in the adjacent configuration. ΔfH° calculated relative to previous results.

Chabazite cluster	Reactant (a.u.)	ΔH _f ° (eV)
Normal	-19823.4020	N/A
1 Hydroxyl nest	-19536.0709	0.03682546
2 Hydroxyl nest	-19172.3441	-1.33897308
3 Hydroxyl nest	-18808.6084	-1.09734542
4 Hydroxyl nest	-18444.8610	-0.77830070
5 Hydroxyl nest	-18081.1154	-0.82833702

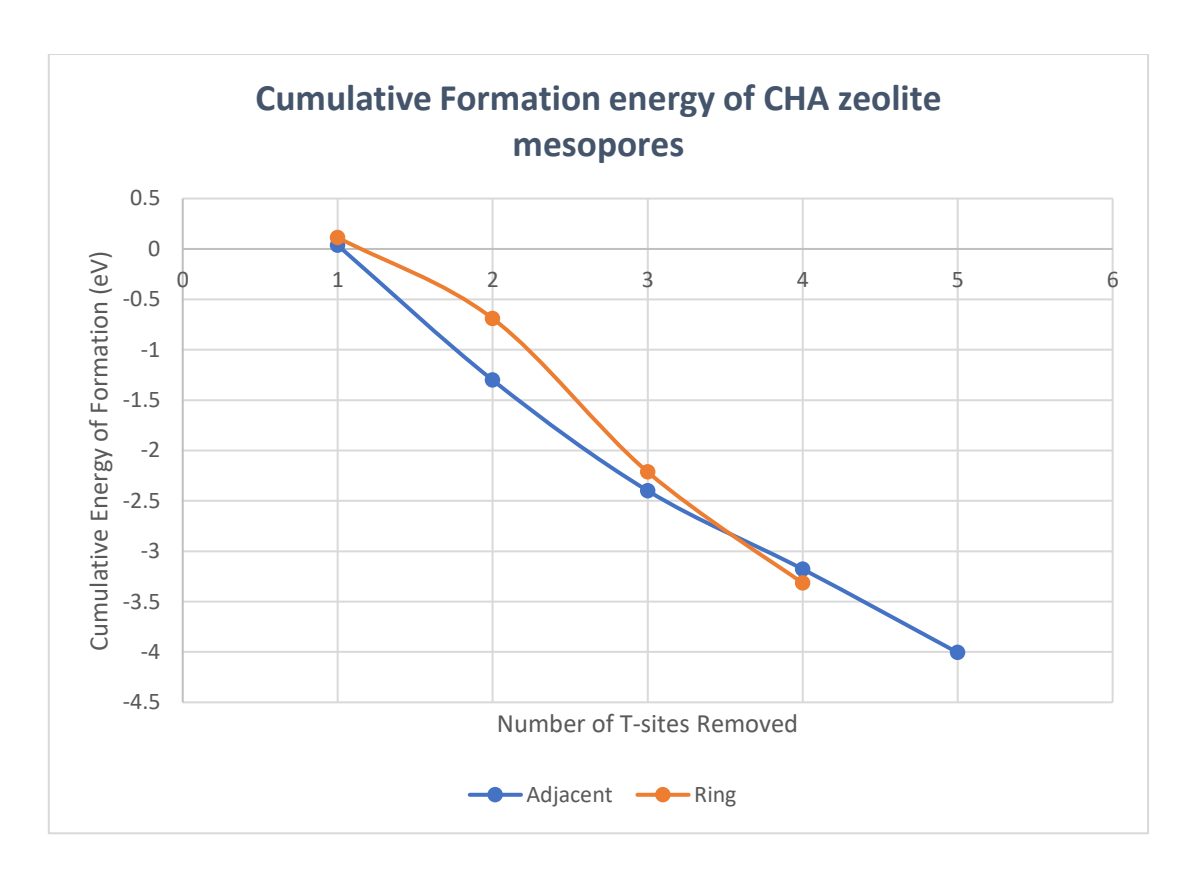


Figure 22: Cumulative formation energy of ZSM-5 mesopores with respect to the number of silicon T-sites remove to energy (eV) to remove an additional T-site. The blue line depicting the adjacent configuration and comparing to the ring configuration in orange.

Considering the change in the framework calculated, as discussed in Chapter 3.2 Chabazite forms a three membered Silanol ring within the nest with an additional hydrogen bond present opposite to the ring. This creates an oxygen atom where both lone pairs electrons on oxygen present now produce hydrogen bonding in the system to nearest neighbour hydrogen atoms. The three silanol groups within the ring show bond lengths between 0.961-1.002 Å and bond angle of 110.407-132.060°. The external silanol group show bond length of 0.958 and a bond angle of 125.709° as shown in Table16.

Table 16: The results from the optimisation of a singular hydroxyl nest in Chabazite showing the bond length (\mathring{A}) and bond angle $(^{\circ})$ of each individual silanol within the mesopore.

Singular Hydroxyl nest	Bond Length (Å)	Bond Angles (°)	Hydrogen Bond Length (Å)
Silanol A	1.002	122.374	2.056
Silanol B	0.968	132.060	1.781
Silanol C	0.961	111.407	1.782
Silanol D	0.958	125.709	2.581

When the hydroxyl nest expands to include two hydroxyl nest defects the shape does not match the results from the ZSM-5 adjacent cluster. The chabazite cluster form the expected double set of three silanol membered rings opposite from one another in the framework. The optimised structure of the Silanol rings are isomers of each other. Both form the rings discussed are forming hydrogen bonding around the framework with different rotation (clockwise and anticlockwise). This phenomenon will be discussed further in the next section on the ring chabazite cluster. The three Silanol groups within the ring have calculated bond lengths between 0.963-0.993 Å and bond angle of 106.629-126.683° as shown in Table 17.

Table 17: The results from the optimisation of two adjacent hydroxyl nest in Chabazite showing the bond length (\mathring{A}) and bond angle $(^{\circ})$ of each individual silanol within the mesopore.

Two Hydroxyl nest	Bond Length (Å)	Bond Angles (°)	Hydrogen Bond Length (Å)
Silanol Ring 1			
Silanol A	0.978	123.254	1.913
Silanol B	0.984	124.149	1.777
Silanol C	0.993	102.392	2.084
Silanol Ring 2			
Silanol A	0.994	122.029	1.725
Silanol B	0.963	106.629	2.178
Silanol C	0.972	126.680	1.757

Moving to the 3rd hydroxyl nest defect, the cluster take shape to form the two three silanol membered ring with a central pair of Silanol groups. The lone of silanol group have no adjacent silanol group in an attaching four membered ring (4MR) or six-membered rings (D6R) but does have a silanol group part of the eight-membered ring. Due to the formation of this cluster the pair of Silanol from a hydrogen bond between each other and the final hydrogen atom doesn't hydrogen bond to the silanol group part of the eight-membered ring due to the distance formed by this ring are far larger than those found within pentasil and 4MR. Unusually, the does not adopt the configuration with hydrogen bonding to the adjacent 4MR due to the preference of this isomer position for differing rotations of hydrogen bonds. The distance between the closest hydrogen bonding pair is 4.348 Å exceeding the hydrogen bonding range. The bond lengths of all the O-H bonding are between 0.948-0.989 Å and the Si-O-H bond angles are between 101.995-136.327° as shown in Table 18.

Table 18: The results from the optimisation of three adjacent hydroxyl nest in Chabazite showing the bond length (\mathring{A}) and bond angle $(^{\circ})$ of each individual silanol within the mesopore.

Three Hydroxyl nest	Bond Length (Å)	Bond Angles (°)	Hydrogen Bond Length (Å)
Silanol Ring 1			
Silanol A	0.983	124.452	1.944
Silanol B	0.978	124.246	2.163
Silanol C	0.995	101.995	1.837
Silanol Ring 2			
Silanol A	0.978	115.158	2.410
Silanol B	0.956	111.650	2.313
Silanol C	0.989	136.327	1.884
Silanol Pair			
Silanol A	0.970	112.809	1.812
Silanol B	0.948	121.527	3.992

The removal of the 4th hydroxyl nest defect from the cluster forms three Silanol ring and a lone silanol group around the defect site. The silanol rings are now too far apart from one another to have any strong interaction between one another. Therefore, no rotational difference of silanol ring was noticed. The now lone silanol group is forming a hydrogen bond with length 2.713 Å with an oxygen atom in the 4MR to which it belongs, even though the oxygen atom is part of a three silanol membered ring. The lack on any other free oxygen atom with an available lone pair of electrons is present therefore will not be able to hydrogen bond leading to a silanol hanging in the channels with no hydrogen bonding possible. The bond lengths of all the O-H bonding are between 0.934-1.005 Å and the Si-O-H bond angles are between 102.619-136.094° as shown in Table 19.

Table 19: The results from the optimisation of four adjacent hydroxyl nest in Chabazite showing the bond length (Å) and bond angle (°) of each individual silanol within the mesopore.

Four Hydroxyl nest	Bond Length (Å)	Bond Angles (°)	Hydrogen Bond Length (Å)
Silanol Ring 1			
Silanol A	0.984	124.271	1.984
Silanol B	0.981	124.449	1.790
Silanol C	0.992	102.619	1.996
Silanol Ring 2			
Silanol A	0.988	114.817	1.869
Silanol B	0.985	129.820	2.285
Silanol C	1.005	102.838	2.437
Silanol Ring 3			
Silanol A	0.956	111.561	2.556
Silanol B	0.985	136.094	1.885
Silanol C	0.981	114.122	1.810
Lone Silanol			
Silanol A	0.939	115.908	2.196

The 5th and final T-site abstraction removes all imperfections with the hydrogen bonding and leave a clear defect site with four three membered silanol rings. The defect site's hydroxyl nests are spaced out throughout multiple channels leaving a large area where catalytic meatal atoms can be seeded to form nanoclusters. The bond lengths of all the O-H bonding are between 0.958-0.975 Å and the Si-O-H bond angles are between 103.446-130.944 ° as shown in Table 20.

Table 20: The results from the optimisation of five adjacent hydroxyl nest in Chabazite showing the bond length (\mathring{A}) and bond angle $(^{\circ})$ of each individual silanol within the mesopore.

Five Hydroxyl nest	Bond Length (Å)	Bond Angles (°)	Hydrogen Bond Length (Å)
Silanol Ring 1			
Silanol A	0.968	119.367	1.902
Silanol B	0.974	116.163	1.794
Silanol C	0.965	112.699	2.517
Silanol Ring 2			
Silanol A	0.968	112.886	2.033
Silanol B	0.961	119.955	2.292
Silanol C	0.975	107.785	1.813
Silanol Ring 3			
Silanol A	0.975	124.639	1.868
Silanol B	0.963	112.054	2.287
Silanol C	0.959	123.060	2.441
Silanol Ring 4			
Silanol A	0.967	113.407	1.976
Silanol B	0.964	113.124	1.768
Silanol C	0.959	124.512	1.991

4.3.2 Mesopore Formation via T-site Removal in Ring Positions

In this section, we computationally model the formation of mesopores in chabazite by selectively removing an entire 4-membered silicon ring, rather than adjacent T-sites, to investigate its impact on pore expansion. The removal of such a ring offers a distinct pathway for mesopore generation, leading to structural changes that differ from the gradual T-site removal approach.

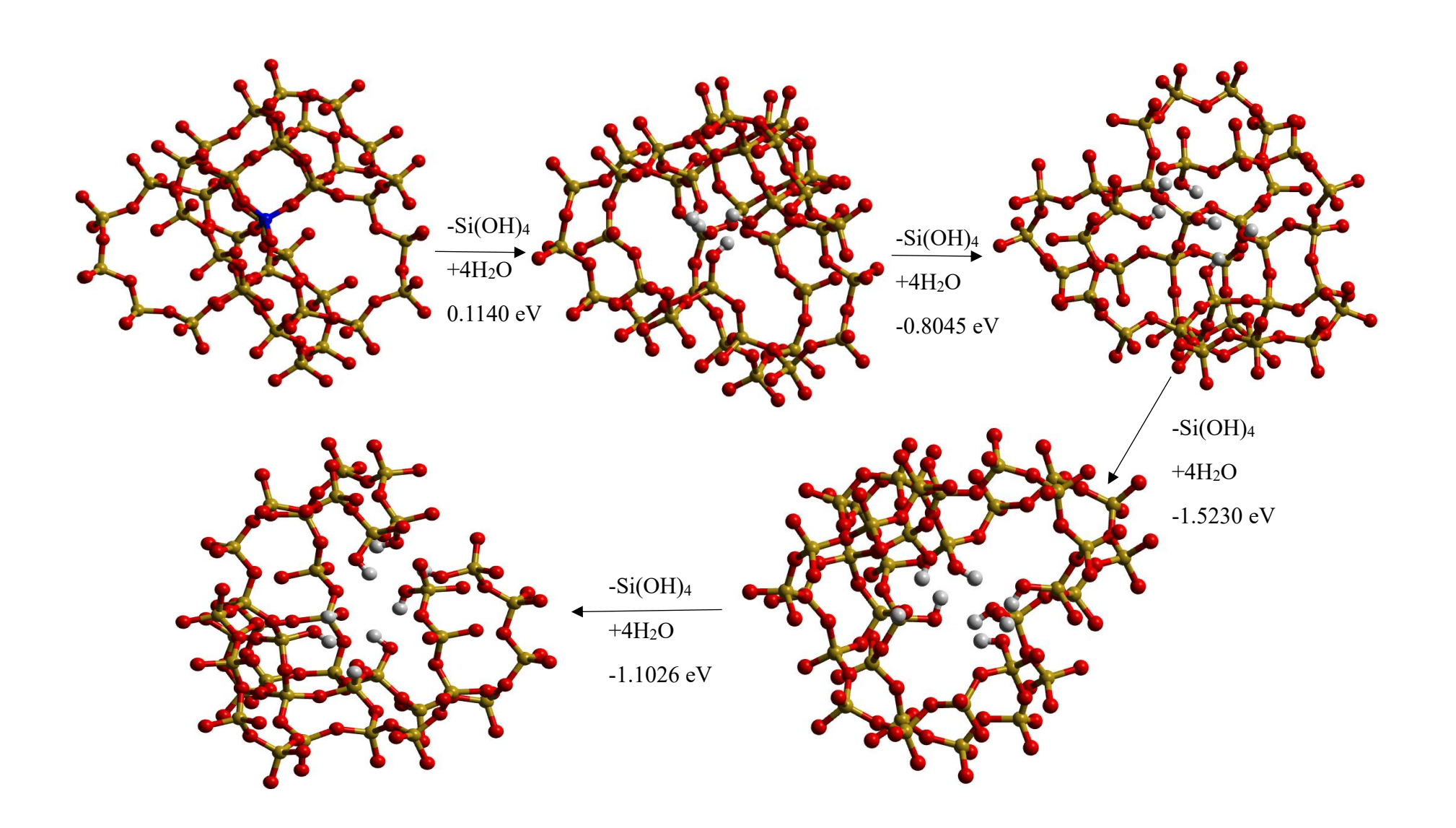
The results for the formation energy of mesopores of various size are given in Table 21. The same results are obtained for both ring and adjacent configurations of the systems when the first hydroxyl nest is removed being an endothermic process rather than the exothermic calculated with larger pore sizes. Subsequent abstractions are exothermic although the increase in the exothermicity becomes smaller after more than three nests are present in the framework.

As discussed in Chapter 4.3.1, chabazite form the three membered silanol ring with the fourth silanol hydrogen bonding to an oxygen atom within the ring during the formation of a singular hydroxyl nest. In both the adjacent and ring models the three membered silanol ring is formed showing that hydroxyl nest is different based on the zeolite types when compared with the 4 membered silanol ring found within ZSM-5 clusters. The endothermic energy for the formation of the first nest in the chabazite cluster shows that the more symmetrical chabazite resists breaking apart to form the hydroxyl nest. The bond length of O-H bonds are 0.933-0.972 Å and with bond angles between the range of 113.137-123.780° as shown in Table 22.

Table 21: The standard enthalpy of formation of Chabazite cluster in the ring configuration. ΔH_f° calculated relative to previous results.

Chabazite cluster	Reactant (a.u.)	ΔH _f ° (eV)
Normal	-19822.9292	N/A
1 Hydroxyl nest	-19535.5952	0.11402143
2 Hydroxyl nest	-19171.8488	-0.80450118
3 Hydroxyl nest	-18808.1287	-1.52301620
4 Hydroxyl nest	-18367.9470	-1.10257838

Hydroxyl Nest Site Aggregation Formation in Chabazite in the Ring Configuration



The introduction of the second hydroxyl nest results in both clusters being in the same rotation before optimisation, as the cluster at this stage is identical to the adjacent one apart from the positions of the protons in the rings. However, the change observed in energy compared with its adjacent counterpart is higher by ~0.5 eV. The cluster was formed this way to show that the position of protons in the opposite configuration (one of the silanol defects are changed so that the bounded proton is now parallel with the opposing silanol) has an effect on the overall energy of the system. The optimised cluster did not form the clear three membered silanol rings but two protons in the cluster are hydrogen bonding to a central oxygen atom and the third proton forced into the channel away from the defect site to accommodate this hydrogen bonding scheme. This form of the defect is the less favourable position of the double hydroxyl nest mesopore; however as discussed in Chapter 4 the rotation of protons around an oxygen requires a significant input of energy. Therefore, both the variation of the defect energy should be possible if during the second defect is in n mirror isomer configuration. The bond length of O-H bonds are 0.943-0.956 Å and with bond angles between the range of 112.910-123.761° as shown in Table 23.

Table 22: The results from the optimisation of a singular hydroxyl nest in Chabazite in the ring configuration showing the bond length (\mathring{A}) and bond angle $(^{\circ})$ of each individual silanol within the mesopore.

Singular Hydroxyl nest	Bond Length (Å)	Bond Angles (°)	Hydrogen Bond Length (Å)
Silanol A	0.972	123.780	1.925
Silanol B	0.957	123.026	1.847
Silanol C	0.967	113.137	2.019
Silanol D	0.953	122.380	1.895

Table 23: The results from the optimisation of two hydroxyl nest in Chabazite in the ring configuration showing the bond length (\mathring{A}) and bond angle $(^{\circ})$ of each individual silanol within the mesopore.

Two Hydroxyl nest	Bond Length (Å)	Bond Angles (°)	Hydrogen Bond Length (Å)
Silanol Ring 1			
Silanol A	0.964	110.080	2.351
Silanol B	0.955	113.169	2.713
Silanol C	0.964	116.677	1.935
Silanol Ring 2			
Silanol A	0.963	112.390	2.619
Silanol B	0.956	116.846	1.723
Silanol C	0.950	123.533	1.713

The removal of the third T-site results in the formation of the two more stable three membered silanol rings. The three adjacent silanol group retake the expected form for the mesopore with energy released growing to ~ 1.5 eV. The pair of silanol produced by cutting the cluster chain together to form a hydrogen between the 1st and 2nd silanol group with the secondary proton being pushed into the cluster's channel. The O-H bond lengths are between 0.940-0.995 Å and with bond angles between the range of $102.852-123.438^{\circ}$ as shown in Table 24.

Table 24: The results from the optimisation of three hydroxyl nest in Chabazite in the ring configuration showing the bond length (\mathring{A}) and bond angle $(^{\circ})$ of each individual silanol within the mesopore.

Three Hydroxyl nest	Bond Length (Å)	Bond Angles (°)	Hydrogen Bond Length (Å)
Silanol Ring 1			
Silanol A	0.965	116.393	2.434
Silanol B	0.967	116.234	2.225
Silanol C	0.974	105.264	1.727
Silanol Ring 2			
Silanol A	0.960	113.470	1.720
Silanol B	0.959	113.686	1.731
Silanol C	0.958	111.108	1.937
Silanol Pair			
Silanol A	0.966	110.404	1.814
Silanol B	0.957	115.757	4.224

The 4th T-site of the 4MR removed forms the configuration where no three membered silanol rings can be formed. The lack of three silanol with proximity of each other leads to the formation of four pairs of silanol groups. The hydrogen bonding found within this cluster is significantly reduced compared to its predecessors, limited to only one of these bonds formed between a pair of silanol group. A limitation is the formation of a single hydrogen bond between these two pairs of silanol groups with bond length of 2.937 Å. It would be expected that a similar bond would be observed in the along the same axis with identical pair opposite; however, the hydrogen bonded is not extended between the pair with it preferring a symmetrical structure extending into the cluster's channels. On the perpendicular axis of the lone pairs, of the cluster the bond distances between the closest oxygen to the proton for hydrogen bonding are 3.702 Å and 3.876 Å. The bond length of O-H bonds are between 0.956 -0.973 Å and with bond angles between the range of 107.462-119.246° as shown in Table 25.

Table 25: The results from the optimisation of four hydroxyl nest in Chabazite in the ring configuration showing the bond length (\mathring{A}) and bond angle $(^{\circ})$ of each individual silanol within the mesopore.

Four Hydroxyl nest	Bond Length (Å)	Bond Angles (°)	Hydrogen Bond Length (Å)
Silanol Pair 1			
Silanol A	0.967	107.462	3.518
Silanol B	0.969	119.246	1.866
Silanol Pair 2			
Silanol C	0.973	108.189	3.752
Silanol D	0.958	115.54	1.783
Silanol Pair 3			
Silanol A	0.963	116.866	3.783
Silanol B	0.957	116.829	1.787
Silanol Pair 4			
Silanol A	0.965	111.137	3.279
Silanol B	0.956	113.694	1.833

4.4 Mesopore Formation in Faujasite: A Computational Study

Following the investigation of mesopore generation in ZSM-5 and chabazite, we now turn our focus to Faujasite, another widely used zeolite with unique structural properties. Unlike the previous zeolites studies in this chapter, Faujasite's framework is characterized by a three-dimensional pore system with large super cages connected by 12-membered oxygen rings, providing a distinct pathway for mesopore creation. In this section, we computationally explore the removal of T-sites and entire rings within the Faujasite framework to generate mesopores and study their impact on the stability and reorganization of the structure. Using hybrid functionals with def2-TZVP and def2-SVP basis sets, we model distinct clusters centred around specific T-sites to investigate how the removal of framework components affects pore expansion. The results provide insight into the mechanisms underlying mesopore formation in Faujasite and its comparison with other zeolites discussed in this work.

4.4.1 Mesopore Formation via T-site Removal in Adjacent Positions

The results for the optimisation of Faujasite with different size mesopores are displayed in Table 26. The results from optimisation, the pattern that has previously been noted in other zeolites is present with formation of larger mesopores will lead to a more exothermic product. It displays that the hardest hurdle to overcome for the formation of mesopore in Faujasite are the removal of the first T-site.

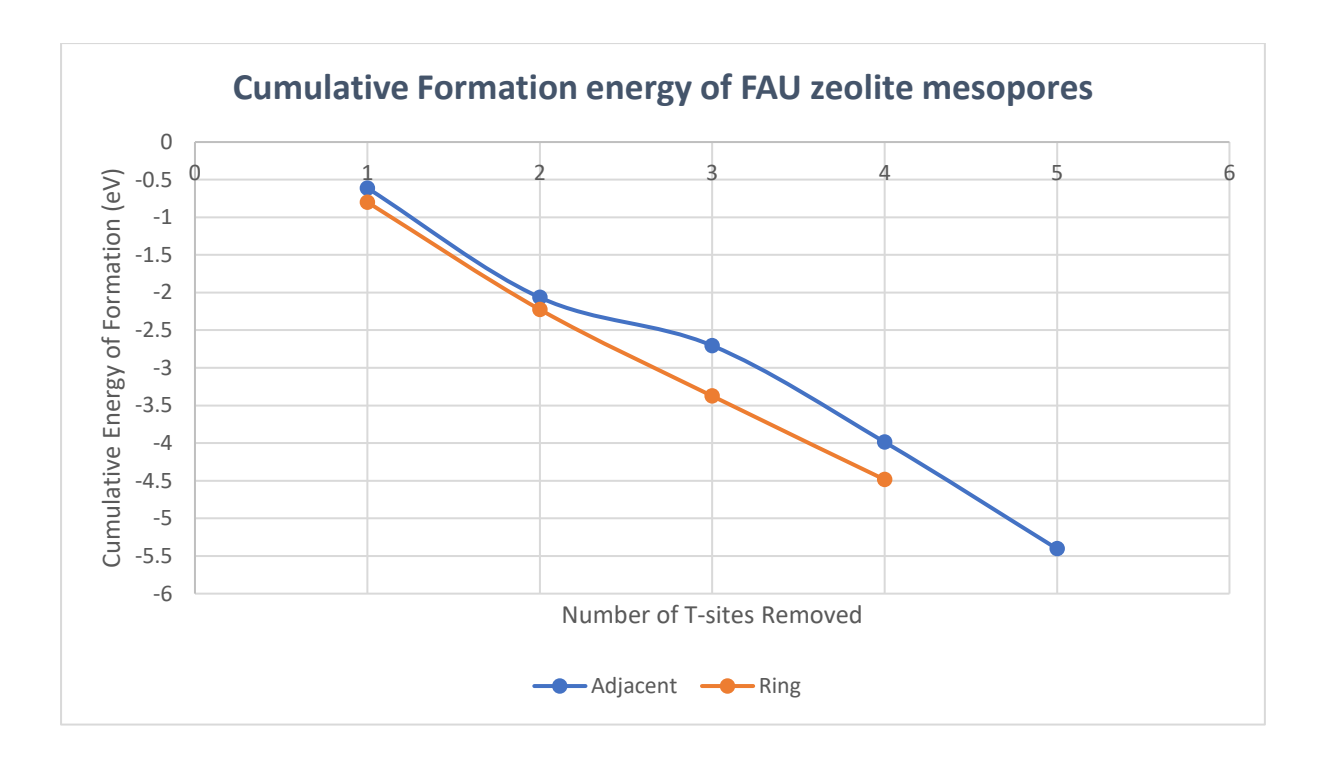


Figure 23: Cumulative formation energy of ZSM-5 mesopores with respect to the number of silicon T-sites remove to energy (eV) to remove an additional T-site. The blue line depicting the adjacent configuration and comparing to the ring configuration in orange.

Hydroxyl Nest Site Aggregation Formation in Faujasite in the Adjacent Configuration

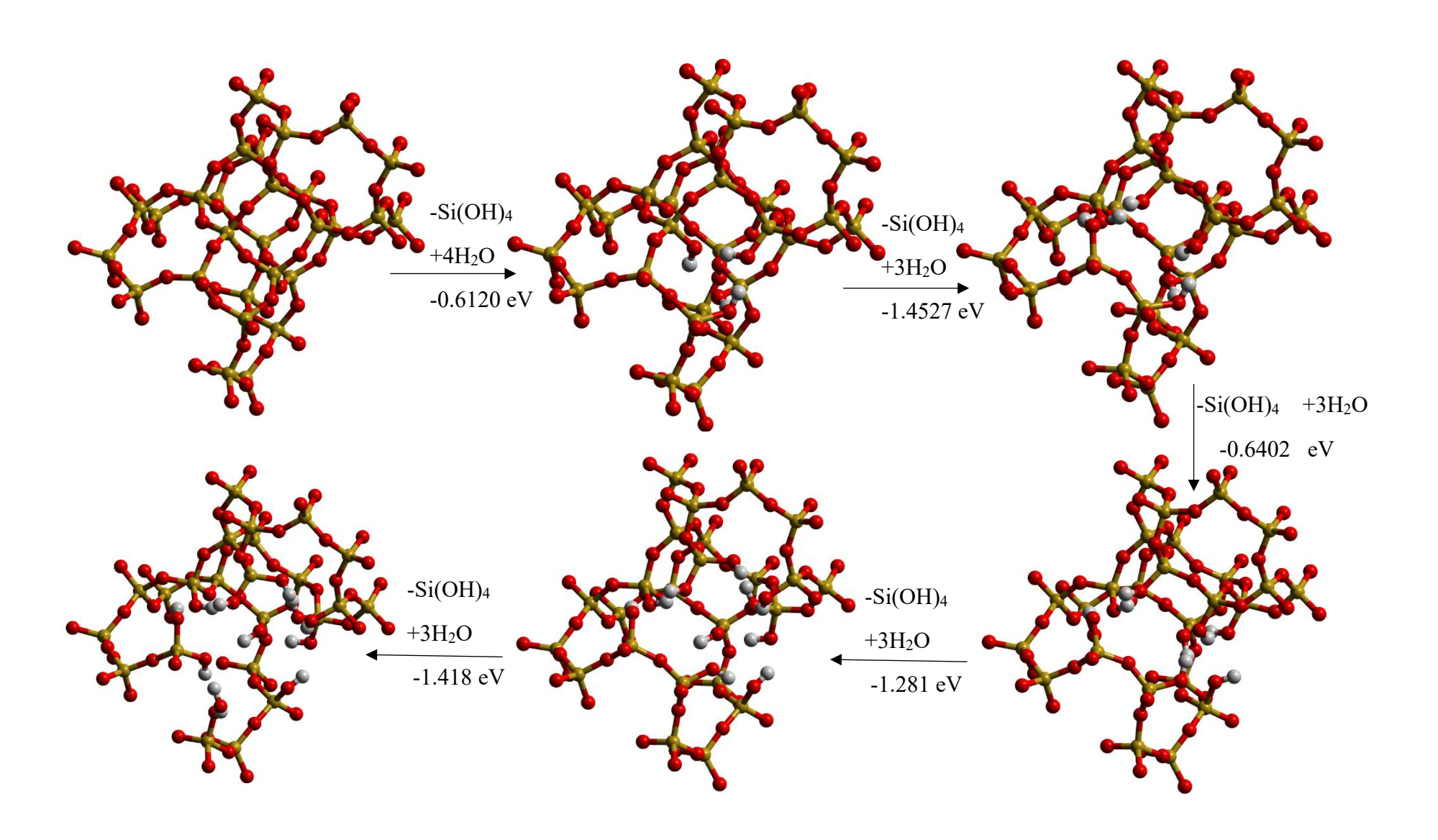


Table 26: The standard enthalpy of formation of Faujasite cluster in the adjacent configuration. ΔH_f° calculated relative to previous results.

Faujasite cluster	Reactant (a.u.)	ΔH _f ° (eV)
Pure	-15109.1569	N/A
1 Hydroxyl nest	-14821.8496	-0.61206563
2 Hydroxyl nest	-14458.1269	-1.45270307
3 Hydroxyl nest	-14094.3745	-0.64018103
4 Hydroxyl nest	-13730.6455	-1.28146136
5 Hydroxyl nest	-13366.9216	-1.41813090

Considering now the structure of hydroxyl nest mesopores, the initial hydroxyl nest forms four individual hydrogen bonds, yet does not establish the anticipated three-membered hydrogen-bonded silanol ring. The bond lengths and angles for these interactions are listed in Table 27, with values remaining consistent within the expected range for silanol bonds in zeolite frameworks.

Table 27: The results from the optimisation of a singular hydroxyl nest in Faujasite showing the bond length (\mathring{A}) and bond angle $(^{\circ})$ of each individual silanol within the mesopore.

Singular Hydroxyl nest	Bond Length (Å)	Bond Angles (°)	Hydrogen Bond Length (Å)
Silanol A	0.964	126.647	2.056
Silanol B	0.987	112.975	1.592
Silanol C	0.970	120.180	1.860
Silanol D	0.975	124.928	1.722

Examining the two-hydroxyl nest defect, we observe the formation of dual three-membered hydrogen-bonded silanol rings. The silanol groups in these rings exhibit distinct rotational orientations relative to each other. Notably, no hydrogen bonding occurs between the silanol rings, resulting in an open configuration that provides access to the internal cages within the Faujasite framework. Bond lengths and angles for these structures are provided in Table 28.

Table 28: The results from the optimisation of two adjacent hydroxyl nest in Faujasite showing the bond length (\mathring{A}) and bond angle $(^{\circ})$ of each individual silanol within the mesopore.

Two Hydroxyl nest	Bond Length (Å)	Bond Angles (°)	Hydrogen Bond Length (Å)
Silanol Ring Clockwise			
Silanol A	0.977	112.490	1.668
Silanol B	0.967	112.494	2.005
Silanol C	0.965	122.603	1.972
Silanol Ring Anticlockwise			
Silanol A	0.971	118.652	1.815
Silanol B	0.968	118.660	1.906
Silanol C	0.970	119.936	1.878

Considering the third hydroxyl nest, we encounter the familiar challenge posed by the absence of a silanol triplet, leading to the formation of two three-membered hydrogen-bonded silanol rings and a separate silanol pair. The three-membered hydrogen-bonded silanol rings are now positioned too far apart for their rotational orientation to significantly impact the system's energy. The silanol pair establishes a hydrogen-bonded chain, where the primary silanol bonds to its pair, while the secondary silanol forms a hydrogen bond with an oxygen atom shared within the same four-membered ring (4MR) and linked to a three-membered hydrogen-bonded silanol ring within the framework. This hydrogen bond measures 1.931 Å. Bond lengths and angles are presented in Table 29.

Table 29: The results from the optimisation of three adjacent hydroxyl nest in Faujasite showing the bond length (\mathring{A}) and bond angle $(^{\circ})$ of each individual silanol within the mesopore.

Three Hydroxyl nest	Bond Length (Å)	Bond Angles (°)	Hydrogen Bond Length (Å)
Silanol Ring 1			
Silanol A	0.966	124.352	1.964
Silanol B	0.978	113.872	1.659
Silanol C	0.967	111.363	2.058
Silanol Ring 2			
Silanol A	0.957	123.879	2.220
Silanol B	0.966	115.602	1.935
Silanol C	0.980	115.392	1.687
Silanol Pair			
Silanol A	0.968	119.550	1.802
Silanol B	0.970	111.180	1.931

For the fourth adjacent hydroxyl nest removed, the structure generates three distinct three-membered hydrogen-bonded silanol rings alongside a lone silanol group. This isolated silanol group does not belong to any small four-membered ring (4MR) that includes other silanol groups within the framework, thus it does not participate in additional hydrogen bonding. Consequently, this lone silanol extends into the large channel characteristic of Faujasite. Bond lengths and angles are measured and detailed in Table 30.

Table 30: The results from the optimisation of four adjacent hydroxyl nest in Faujasite showing the bond length (\mathring{A}) and bond angle $(^{\circ})$ of each individual silanol within the mesopore.

Four Hydroxyl nest	Bond Length (Å)	Bond Angles (°)	Hydrogen Bond Length (Å)
Silanol Ring 1			
Silanol A	0.973	115.946	1.808
Silanol B	0.971	111.916	1.862
Silanol C	0.966	118.488	2.105
Silanol Ring 2			
Silanol A	0.971	118.633	1.771
Silanol B	0.969	115.100	1.931
Silanol C	0.967	115.739	2.042
Silanol Ring 3			
Silanol A	0.967	120.853	1.753
Silanol B	0.974	109.022	1.776
Silanol C	0.958	121.108	2.774
Lone Silanol			
Silanol A	0.957	118.129	2.768

With the removal of the final T-site, all remaining possibilities for forming non-preferred structures are eliminated, leading exclusively to the formation of four three-membered hydrogen-bonded silanol rings. This configuration generates a substantial mesopore vacancy within the Faujasite framework. Bond lengths and bond angles are provided in Table 31.

Table 31: The results from the optimisation of five adjacent hydroxyl nest in Faujasite showing the bond length (\mathring{A}) and bond angle $(^{\circ})$ of each individual silanol within the mesopore.

Five Hydroxyl nest	Bond Length (Å)	Bond Angles (°)	Hydrogen Bond Length (Å)
Silanol Ring 1			
Silanol A	0.965	112.434	2.039
Silanol B	0.965	118.165	2.451
Silanol C	0.972	115.330	1.775
Silanol Ring 2			
Silanol A	0.967	111.399	2.028
Silanol B	0.969	118.316	1.891
Silanol C	0.963	117.736	2.259
Silanol Ring 3			
Silanol A	0.969	115.048	1.955
Silanol B	0.972	119.651	1.739
Silanol C	0.965	116.159	2.110
Silanol Ring 4			
Silanol A	0.975	108.570	1.751
Silanol B	0.957	120.642	2.626
Silanol C	0.966	121.201	1.756

The removal of the final T-site in Faujasite completes the formation of four stable three-membered hydrogen-bonded silanol rings, resulting in a large, stable mesopore within the framework. Bond lengths and angles are consistent with trends observed in prior models, though Faujasite's stability around large mesopores is notably robust, suggesting enhanced resistance to framework collapse similar to the Chabazite cluster for the adjacent variation.

4.4.2 Mesopore Formation via T-site Removal in Ring Positions

The formation energies for this clusters shows a similar trend to its adjacent counterpart with the first hydroxyl nest being formed being the less exothermic reaction. Due to the rings removed only having four T-sites, the pattern cannot be associated with the results from adjacent calculations as it would require removing a subsequent ring to goes beyond the scope

of this thesis. Examining Table 32, the energies of the system are all exothermic, taking note of the increase of \sim 80% more exothermic when going from one to two hydroxyl nests followed by a lowering of energies by \sim 0.3 eV for the subsequent hydroxyl nests. Looking at the energy difference between adjacent and ring calculations we can note that the formation a four T-site mesopore with the ring configuration is \sim 0.5 eV more exothermic as shown in Figure 23.

Table 32: The standard enthalpy of formation of Faujasite cluster in the ring configuration. $\Delta_l H^{\circ}$ calculated relative to previous results

Faujasite cluster	Reactant (a.u.)	ΔH _f ° (eV)
Pure	-15108.6843	N/A
1 Hydroxyl nest	-14821.3839	-0.79884743
2 Hydroxyl nest	-14457.6603	-1.42611513
3 Hydroxyl nest	-14093.9266	-1.14952717
4 Hydroxyl nest	-13653.7451	-1.11040774

For the removal of the first, second, and third T-sites, refer to the adjacent structure as these clusters remain identical with only minor differences in bond lengths and angles, as summarized in Table 33.

Hydroxyl Nest Site Aggregation Formation in Faujasite in the Ring Configuration

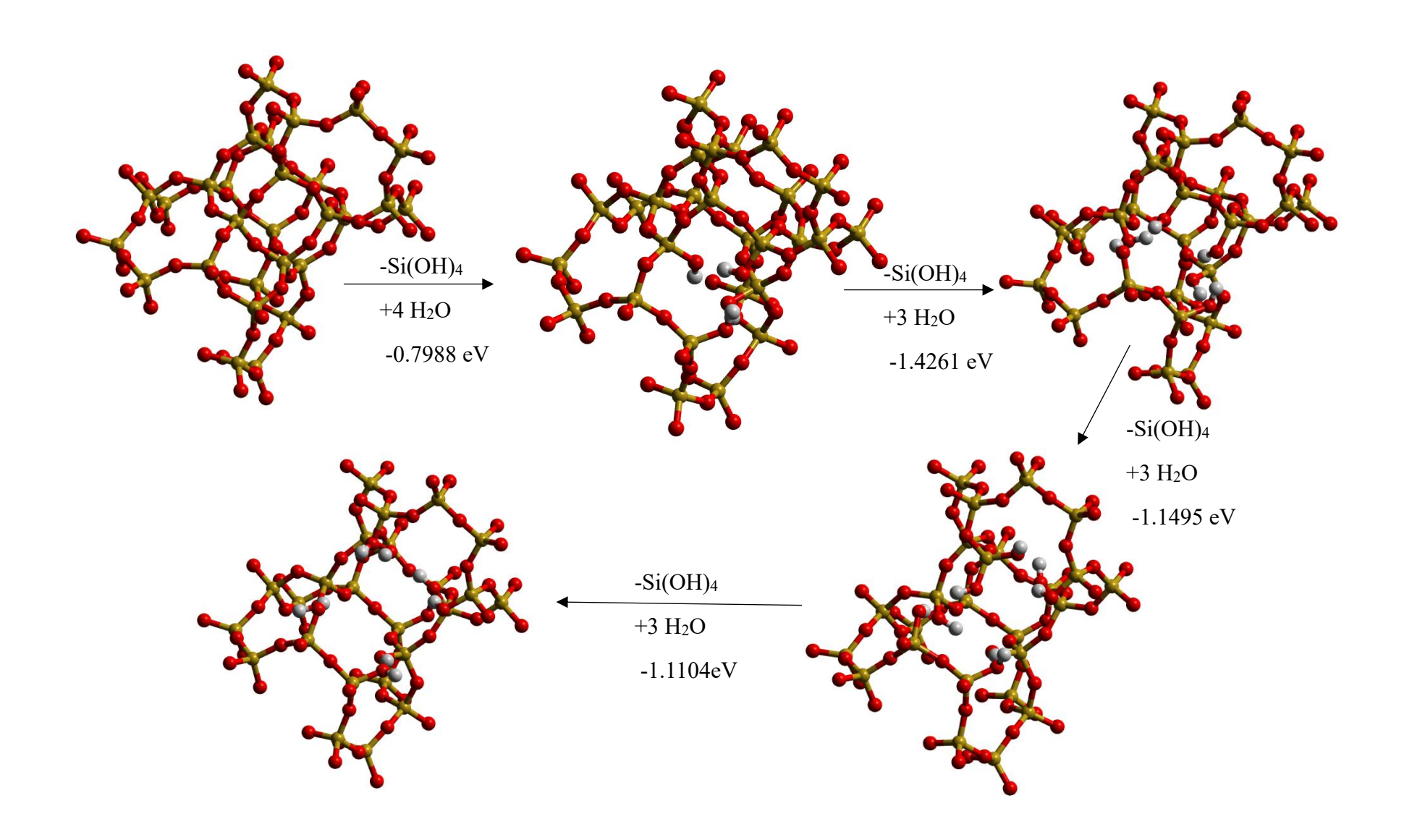


Table 33: The results from the optimisation of singular, two and three hydroxyl nests in Faujasite in the ring configuration showing the bond length (Å) and bond angle (°) of each individual silanol within the mesopore.

			Hydrogen	Bond	Length
Singular Hydroxyl nest	Bond Length (Å)	Bond Angles (°)	(Å)		
Silanol A	0.964	127.361	1.992		
Silanol B	0.987	113.953	1.574		
Silanol C	0.975	124.554	1.717		
Silanol D	0.973	118.242	1.840		
Two Hydroxyl nest					
Silanol Ring Clockwise					
Silanol A	0.971	112.061	1.808		
Silanol B	0.970	110.985	1.958		
Silanol C	0.940	124.390	1.987		
Silanol Ring					
Anticlockwise					
Silanol A	0.970	118.311	1.869		
Silanol B	0.970	117.869	1.846		
Silanol C	0.973	118.555	1.851		
Three Hydroxyl nest					
Silanol Ring 1					
Silanol A	0.978	108.066	1.755		
Silanol B	0.971	115.670	2.129		
Silanol C	0.964	121.394	2.064		
Silanol Ring 2					
Silanol A	0.958	119.792	2.287		
Silanol B	0.956	119.724	2.642		
Silanol C	0.966	110.717	2.053		
Silanol Pair					
Silanol A	0.971	115.629	1.830		
Silanol B	0.960	117.935	2.777		

Upon removal of the final T-site from the 4MR, the cluster contains four pairs of silanol groups. The silanol groups associated with the 6MR do not form discrete pairs but instead create an extended chain of hydrogen-bonded silanol groups. This chain formation is enabled by the structural arrangement of the oxygens; the closest distance between pairs reaches approximately 2.8 Å, allowing one of the silanol's hydrogen atoms to bridge across the 6MR

and establish a hydrogen bond. However, the silanol groups related to the 4MR do not exhibit hydrogen bonding due to the greater oxygen separation, which exceeds 4 Å. All bond lengths and angles are detailed in Table 34.

Table 34: The results from the optimisation of four hydroxyl nest in Faujasite in the ring configuration showing the bond length (\mathring{A}) and bond angle $(^{\circ})$ of each individual silanol within the mesopore.

Four Hydroxyl nest	Bond Length (Å)	Bond Angles (°)	Hydrogen Bond Length (Å)
Silanol Pair			
Silanol A	0.968	116.040	1.822
Silanol B	0.959	116.513	2.622
Silanol Pair			
Silanol A	0.967	112.837	1.914
Silanol B	0.962	113.507	2.428
Silanol Chain			
Silanol A	0.972	111.114	1.726
Silanol B	0.970	121.826	1.890
Silanol C	0.970	112.100	1.791
Silanol D	0.960	117.078	2.685

The mesopore formation in Faujasite shows that the clusters consistently form three-membered silanol rings, although deviations arise with increasing T-site removals, particularly in the fourand six-membered rings (4MR and 6MR). Larger distances between silanol oxygens prevent hydrogen bonding in certain cases, notably within the 4MR, while closer arrangements in the 6MR facilitate the formation of hydrogen-bonded silanol chains. These structural variations in Faujasite align with findings in other zeolites, where increased mesopore formation induces distinct bonding patterns depending on T-site coordination and spatial constraints within the framework.

4.5 Mesopore Formation in α-Quartz: A Computational Perspective

In addition to zeolites, mesopore formation in crystalline silicates such as α -quartz is of great interest due to its simpler, yet highly ordered, tetrahedral framework. α -Quartz, a polymorph of silicon dioxide, differs from zeolites as it lacks the extensive internal porosity of a zeolitic framework, but its stable and well-understood crystal structure provides a useful comparative model for understanding the behaviour of silicate frameworks under structural modification. In this section, we model the removal of silicon atoms (T-sites) from the α -quartz framework to simulate mesopore generation, using hybrid functionals with def2-TZVP and def2-SVP basis sets. These studies offer a baseline to explore how mesopore creation in non-porous crystalline structures contrasts with that in zeolites like ZSM-5 and Faujasite, shedding light on the structural response and stability of silicate frameworks during pore expansion.

All relevant components of the active site, including the neighbouring silicon atoms and the linking oxygen atoms in both the first and second coordination spheres, were incorporated into the quantum mechanical (QM) zone surrounding the central T-site. The cluster size was carefully calibrated to maintain a sufficient number of neighbouring T-sites around the mesopore, particularly after the removal of five T-sites or the 6 membered ring (6MR), ensuring a realistic representation of the framework's stability. The quantum mechanical region (QM1) of the cluster, comprising 17 (adjacent configuration) and 24 (ring configuration) atoms, was selected following the approach outlined in the computational methods section to balance computational efficiency with the accuracy required for capturing the effects of pore expansion on the structural and energetic properties of the α -quartz framework.

4.5.1 Mesopore Formation via T-site Removal in Adjacent Positions

The visualized atomic configurations of the optimised α -quartz cluster shown below illustrate the methods that will be explored during this section. Removal of five adjacent T-sites changes the structure of α -quartz from a closely packed SiO₄ linked in a continuous framework to form a large vacancy inside the framework. The results for the optimisation of chabazite with different sized mesopores are displayed in Table 35 with a side by side comparison of both models in Figure 24. The energy of clusters obtained after optimisation are exothermic, including for the first nest formation as calculated for several of the other zeolites previously studied. The first two hydroxyl nests removed from the system require ~0.3 eV to release Si(OH)₄; then we observe a jump to ~0.75 eV released. The energy suggests that after the first T-site is removed, the system will more favourably expand the clusters leading to the large mesopores.

Table 35: The standard enthalpy of formation of α -Quartz cluster in the adjacent configuration. ΔHf° calculated relative to previous results.

α-Quartz cluster	Reactant (a.u.)	$\Delta H_{\rm f}^{\circ}$ (eV)
Pure	-16175.9675	N/A
1 Hydroxyl nest	-15888.6455	-0.21283532
2 Hydroxyl nest	-15519.1108	-0.29708384
3 Hydroxyl nest	-15155.3622	-0.74455894
4 Hydroxyl nest	-14791.6131	-0.73274400
5 Hydroxyl nest	-14427.5446	-0.78734294

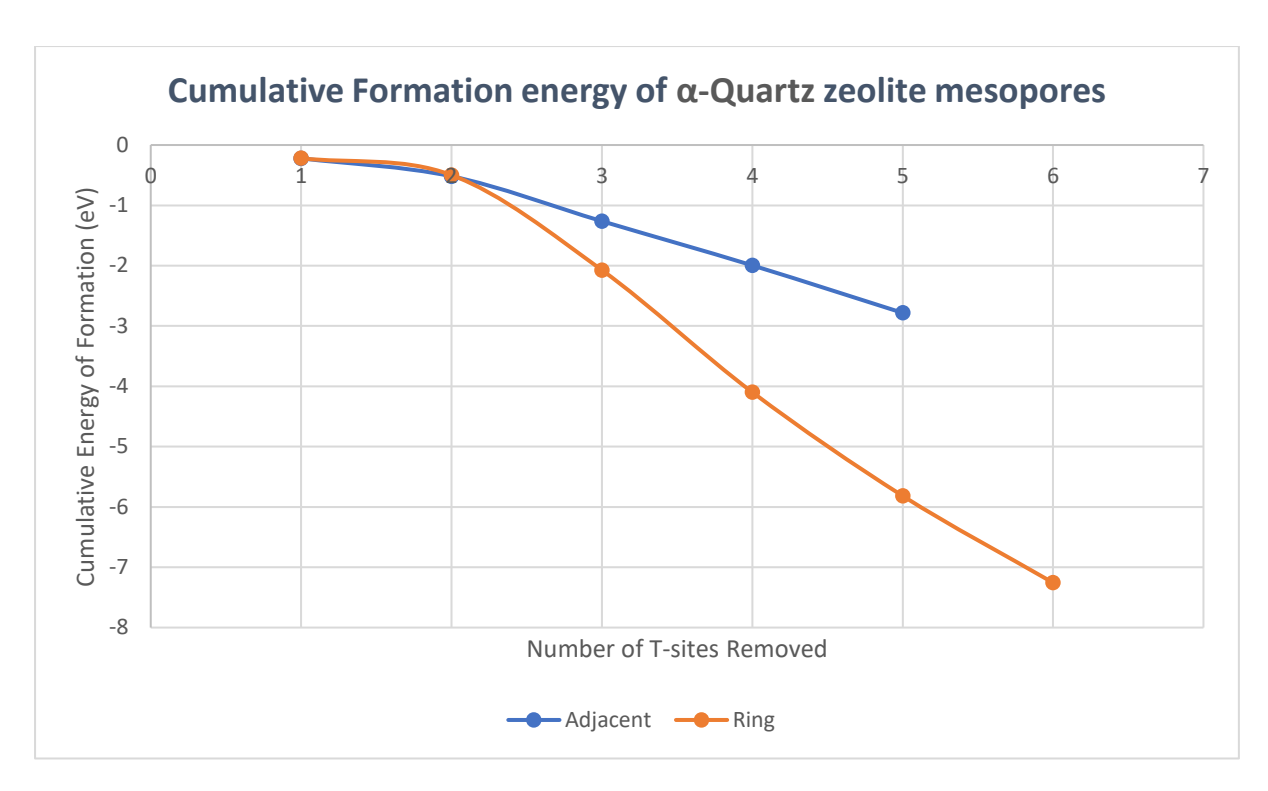
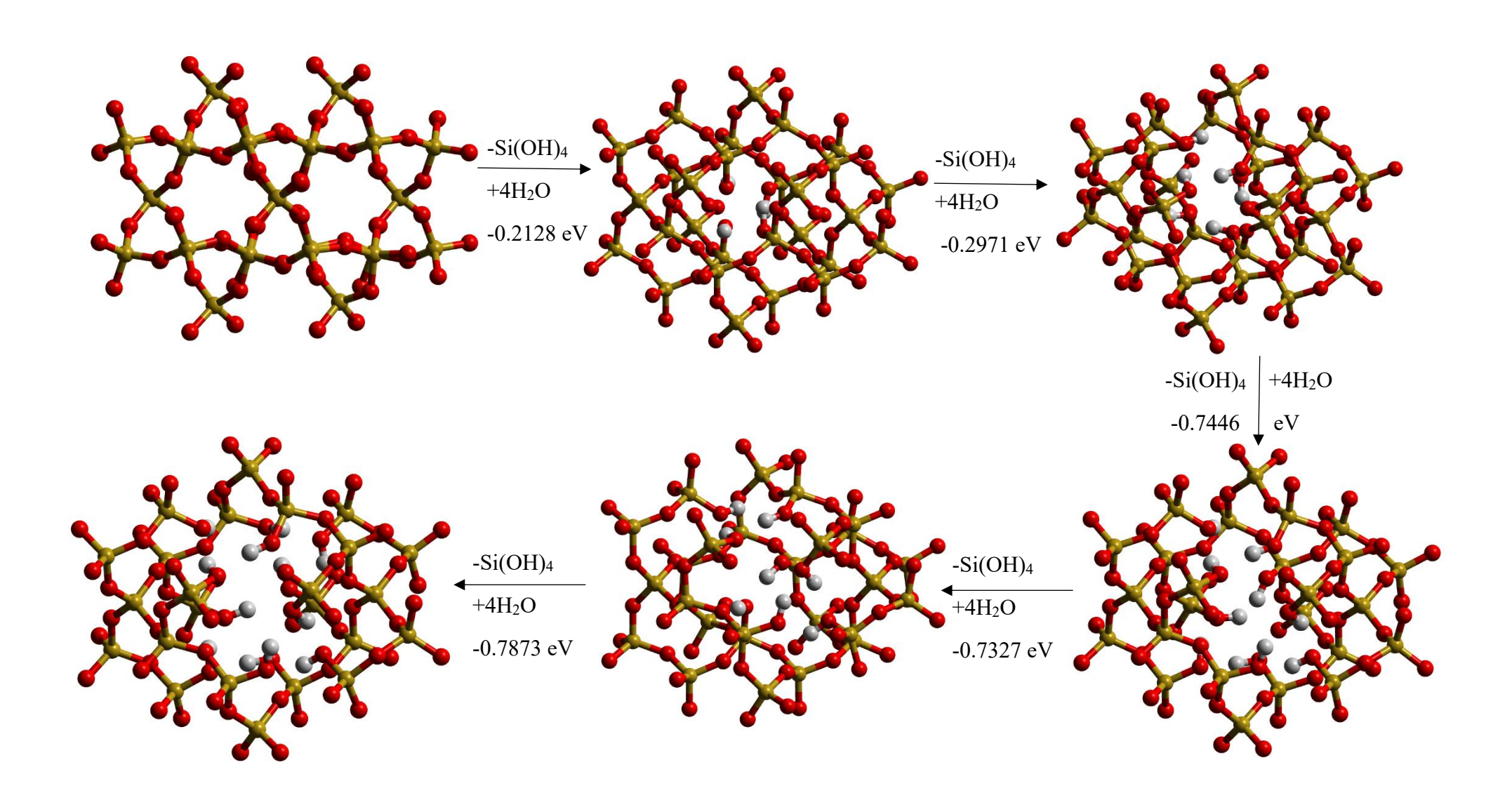


Figure 24: Cumulative formation energy of α -Quartz mesopores with respect to the number of silicon T-sites remove to energy (eV) to remove an additional T-site. The blue line depicting the adjacent configuration and comparing to the ring configuration in orange.

Hydroxyl Nest Site Aggregation Formation in α-quartz in the Adjacent Configuration



Examining the structures of these pores the single hydroxyl nest takes the form of the double hydrogen bonded four membered silanol cubic formation leading to a closely packed defect site. As the defect grows to include a secondary defect, the shape changes and does not produce any two three membered silanol rings but rather a chain of hydrogen bonded silanols. This chain, however, does not in the channels as previously observed in zeolites with channels but with hydrogen bonded to an oxygen that is covalently bonded with two silicon atoms as shown in Figure 25. The length of this extra hydrogen bond is greater than those observed between silanol group at \sim 1.75-2 Å rather than the \sim 1.6 Å. Due to the structure of α -quartz rather than the misaligned silanol group, we observe a staggered parallel rotating layer of chains, which is possible due to the hydrogen bonding occurring between the silanol chains with the distance between the hydrogens and the oxygens remain between 2.968-3.805 Å as shown in Table 36.

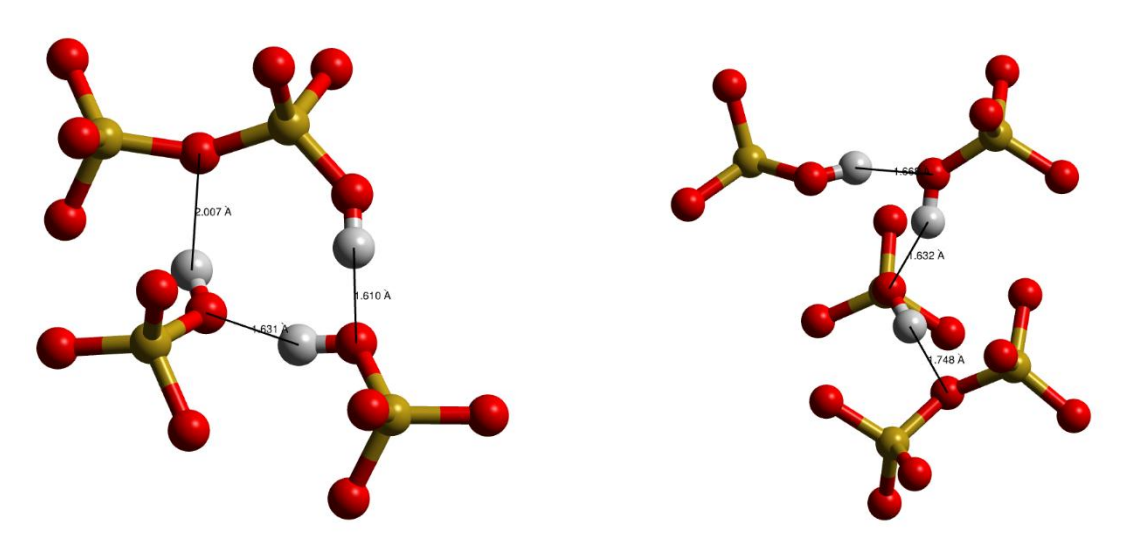


Figure 25: Structural diagram of the 2 different layers of silanol groups observed in α -quartz with the hydrogen bond lengths shown.

Table 36: The results from the optimisation of two adjacent hydroxyl nest in α -Quartz showing the bond length (Å) and bond angle (°) of each individual silanol within the mesopore.

Two Hydroxyl nest	Bond Length (Å)	Bond Angles (°)	Hydrogen Bond Length (Å)
Silanol Ring 1			
Silanol A	0.970	138.762	1.675
Silanol B	0.976	117.313	1.597
Silanol C	0.963	124.723	2.222
Silanol Ring 2			
Silanol A	0.971	115.341	1.736
Silanol B	0.976	124.984	1.610
Silanol C	0.972	121.747	1.671

The 3rd hydroxyl nest defect returns the cluster to the expected outcome seen in previous zeolites. A pair of two three membered silanol rings with a chain of two silanol groups between them. However, once again due to the lack of channels the pair of silanol group will hydrogen bond to an oxygen that is covalently bonded to two silicon atoms. Bond lengths and bond angles are provided in Table 37. The same pattern is observed when increasing to four removed T-sites, with three different three membered silanol rings generated with a lone silanol group. Unlike the 3 T-site mesopore, the cluster has now grown into a large vacant space inside the framework; therefore, rather than hydrogen bonding with an oxygen atom it remains in the vacancy with no forces interacting other than van der Waals. Bond lengths and bond angles are provided in Table 38. The final hydroxyl nest removed forms a series of four three membered silanol rings. The cluster is now a large void inside the centre of the cluster that is maintain with a layer of O-H bonds and hydrogen bonds preventing the cluster from collapsing into itself. Bond lengths and bond angles are provided in Table 39.

Table 37: The results from the optimisation of three adjacent hydroxyl nest in α -Quartz showing the bond length (Å) and bond angle (°) of each individual silanol within the mesopore.

Three Hydroxyl nest	Bond Length (Å)	Bond Angles (°)	Hydrogen Bond Length (Å)
Silanol Ring 1			
Silanol A	0.969	139.198	1.622
Silanol B	0.976	115.898	1.654
Silanol C	0.964	122.760	1.910
Silanol Ring 2			
Silanol A	0.975	114.296	1.806
Silanol B	0.962	113.109	2.164
Silanol C	0.974	122.606	1.727
Silanol Pair			
Silanol A	0.971	122.943	1.689
Silanol B	0.969	118.212	1.879

Table 38: The results from the optimisation of four adjacent hydroxyl nest in α -Quartz showing the bond length (Å) and bond angle (°) of each individual silanol within the mesopore.

Four Hydroxyl nest	Bond Length (Å)	Bond Angles (°)	Hydrogen Bond Length (Å)
Silanol Ring 1			
Silanol A	0.968	109.329	1.837
Silanol B	0.968	112.728	1.794
Silanol C	0.965	117.420	2.155
Silanol Ring 2			
Silanol A	0.977	112.931	1.747
Silanol B	0.973	120.980	1.746
Silanol C	0.964	113.375	2.065
Silanol Ring 3			
Silanol A	0.960	114.376	2.220
Silanol B	0.970	116.032	1.738
Silanol C	0.968	136.058	1.635
Lone Silanol			
Silanol A	0.955	117.923	3.830

Table 39: The results from the optimisation of five adjacent hydroxyl nest in α -Quartz showing the bond length (Å) and bond angle (°) of each individual silanol within the mesopore.

Five Hydroxyl nest	Bond Length (Å)	Bond Angles (°)	Hydrogen Bond Length (Å)
Silanol Ring 1			
Silanol A	0.962	114.889	2.077
Silanol B	0.969	117.892	2.276
Silanol C	0.964	115.437	1.885
Silanol Ring 2			
Silanol A	0.976	120.202	1.725
Silanol B	0.980	113.237	1.713
Silanol C	0.964	114.163	2.131
Silanol Ring 3			
Silanol A	0.962	118.330	2.295
Silanol B	0.981	123.746	1.673
Silanol C	0.973	118.511	1.753
Silanol Ring 4			
Silanol A	0.971	138.082	1.623
Silanol B	0.960	114.151	2.400
Silanol C	0.972	115.316	1.741

4.5.2 Mesopore Formation via T-site Removal in Ring Positions

In this section, we model the formation of mesopores in α -Quartz by selectively removing an entire 6-membered silicon ring (6MR), rather than adjacent T-sites, to investigate its impact on pore expansion. The removal of such a ring offers a distinct pathway for mesopore generation, leading to structural changes that differ from the gradual T-site removal approach.

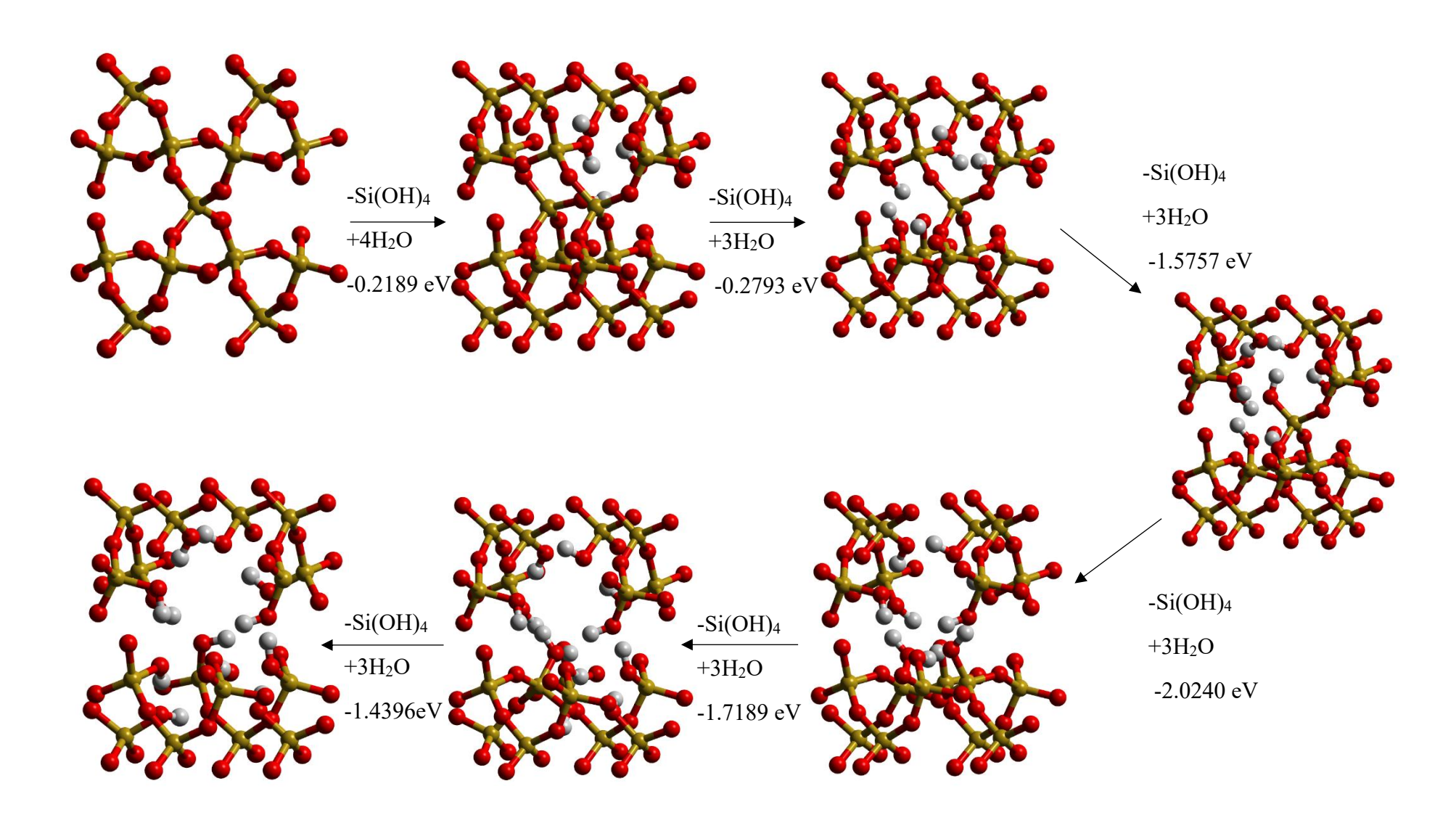
The formation energy for the ring configurations are considerably more exothermic than their adjacent counterparts. The total formation energy of the ring configuration is ~3 eV more exothermic than the adjacent configuration. They follow a similar pattern in that the first two T-sites removed are significantly less exothermic then all the following T-sites.

The results for the formation energy of mesopores of various size are given in Table 40.

Table 40: The standard enthalpy of formation of α -Quartz cluster in the adjacent configuration. ΔH_f° calculated relative to previous results.

α-Quartz cluster	Reactant (a.u.)	$\Delta H_{\rm f}^{\circ} ({\rm eV})$
Pure	-13100. 5014	N/A
1 Hydroxyl nest	-12813. 1796	-0.21887161
2 Hydroxyl nest	-12449.4139	-0.27929620
3 Hydroxyl nest	-12085.6862	-1.57572846
4 Hydroxyl nest	-11721.9500	-2.02397233
5 Hydroxyl nest	-11358.1950	-1.71887896
6 Hydroxyl nest	-10842.9662	-1.43964822

Hydroxyl Nest Site Aggregation Formation in α-quartz in the Ring Configuration



The change in structure and energy appear to be nearly identical for the first two hydroxyl nests as would be expected. However, once the cluster exceeds three T-sites removed the energies starts to deviate where a large decrease in energy is observed. The energy released is doubled going from 0.74~eV in adjacent to 1.6~eV for the ring configuration. The large increase in exothermicity shows that the ring configuration is the reaction pathway that would be most likely to occur within a pure α -quartz cluster.

The structure observed for the first three hydroxyl nest is identical to those observed for the adjacent configuration as discussed in the previous section. All the bond length and bond angles are recorded in Table 41.

Table 41: The results from the optimisation of singular, two and three hydroxyl nests in α -quartz in the ring configuration showing the bond length (Å) and bond angle (°) of each individual silanol within the mesopore.

Singular Hydroxyl nest	Bond Length (Å)	Bond Angles (°)	Hydrogen Bond Length (Å)
Silanol A	0.969	120.721	1.888
Silanol B	0.973	116.211	1.720
Silanol C	0.963	120.787	1.989
Silanol D	0.970	113.039	2.110
Two Hydroxyl nest			
Silanol Ring 1			
Silanol A	0.962	123.811	2.099
Silanol B	0.984	108.907	1.608
Silanol C	0.976	111.242	1.622
Silanol Ring 2			
Silanol A	0.970	121.420	1.829
Silanol B	0.976	116.804	1.757
Silanol C	0.975	123.810	1.695
Three Hydroxyl nest			
Silanol Ring 1			
Silanol A	0.974	118.311	1.741
Silanol B	0.970	120.960	1.772
Silanol C	0.976	122.792	1.726
Silanol Ring 2			
Silanol A	0.963	125.500	1.965
Silanol B	0.979	167.420	1.666
Silanol C	0.981	111.535	1.596
Silanol Pair			
Silanol A	0.969	118.858	1.765
Silanol B	0.963	113.953	2.241

However, moving to the fourth hydroxyl nest defect we observe the formation of two three membered silanol rings with a two pair of silanol groups. The silanol pairs once again trapped but the small pore size of α -quartz are forced to hydrogen bond with the nearest available lone pair of electrons to reduce the strain of the framework. Bond lengths and bond angles are provided in Table 42.

Table 42: The results from the optimisation of four hydroxyl nests in α -quartz in the ring configuration showing the bond length (Å) and bond angle (°) of each individual silanol within the mesopore.

Four Hydroxyl nest	Bond Length (Å)	Bond Angles (°)	Hydrogen Bond Length (Å)
Silanol Ring 1			
Silanol A	0.964	126.439	1.884
Silanol B	0.975	109.728	1.708
Silanol C	0.981	111.023	1.598
Silanol Ring 2			
Silanol A	0.978	119.619	1.670
Silanol B	0.968	118.608	1.794
Silanol C	0.971	119.502	1.889
Silanol Pair 1			
Silanol A	0.970	118.262	1.760
Silanol B	0.965	112.435	2.129
Silanol Pair 2			
Silanol A	0.970	119.832	1.702
Silanol B	0.962	116.778	2.318

Moving to the fifth T site removed the framework removes a lot of its structure; the lack of an adjacent silanol group prevents the formation of all but one three membered silanol ring. All other hydrogen atoms attempt to bond with the nearest lone pair leading to a wide range of single pairs and chains of hydrogen bonded silanol groups. It is expected that the configuration of this protons could be varied extensively in this cluster due to the proximity of protons to a wide range of neighbouring oxygen atoms. The energy obtained for these clusters are simply a local minimum for the formation of one of one possible isomer, and it is possible that lower energy proton configurations could occur, but it is unlikely that they will differ much in energy.

Moving to the final T site removed from the original 6MR, the structure of the cluster returns to some of the previously observed patterns seen in other zeolites as the pore within the framework has grown substantially. The silanol groups can now pair off with each other

forming six pairs (hydrogen bonding distance below 1.9 Å) that each end by hydrogen bonding to either another silanol group to form a longer chain (hydrogen bonding distance over 1.9 Å) or to an oxygen bonded to two silicon atoms. All the bond length are recorded in Table 43.

Table 43: The results from the optimisation of six hydroxyl nests in α -quartz in the ring configuration showing the bond length (Å) and bond angle (°) of each individual silanol within the mesopore.

Sixth Hydroxyl nest	Bond Length (Å)	Bond Angles (°)	Hydrogen Bond Length (Å)
Silanol Pair 1			
Silanol A	0.972	115.034	1.972
Silanol B	0.975	116.302	1.916
Silanol Pair 2			
Silanol A	0.971	115.441	1.786
Silanol B	0.964	112.773	2.109
Silanol Pair 3			
Silanol A	0.971	116.923	1.680
Silanol B	0.968	110.691	2.102
Silanol Pair 4			
Silanol A	0.972	119.116	1.720
Silanol B	0.971	114.065	1.979
Silanol Pair 5			
Silanol A	0.964	121.796	1.807
Silanol B	0.964	110.362	2.349
Silanol Pair 6			
Silanol A	0.976	116.183	1.775
Silanol B	0.968	113.29	2.166

4.6 Conclusion

The computational analysis across the four zeolites—ZSM-5, Chabazite, Faujasite, and α-Quartz—highlighted key structural transformations in response to mesopore formation via Tsite removals. Each framework demonstrated distinct hydrogen-bonding configurations, yet certain trends emerged. In ZSM-5, Chabazite and Faujasite, mesopore creation led to stable three-membered silanol rings, with bond lengths and angles mostly remaining within expected ranges as pores expanded. The ring configuration prevented the formation of the stable threemembered silanol rings when a ring was fully removed from the system; however, a high concentration of hydrogen bonding is still observed. In Faujasite, the removal of T-sites within both 4MR and 6MR rings revealed a more complex behaviour: some silanol groups formed extended chains due to closer interatomic distances, while others lacked hydrogen bonding due to spatial limitations. α-Quartz exhibited the least formation of stable silanol ring structures, reflecting its distinct crystalline properties. Across all zeolites, larger mesopore formation introduced structural strain, resulting in increased energy demands for further T-site removal, underscoring the role of zeolite framework geometry in stabilizing or destabilizing mesopore creation. All Silanol groups attempt to make a hydrogen bond with the nearest available lone pair of electrons in the order to stabilise the systems. As the size of the mesopore increase the number of long-range hydrogen bonds increase due to the removal of neighbouring oxygen and therefore weakening the structure of the zeolite frameworks. The silanol with no direct adjacent silanol are forced to create long range hydrogen bonding as they are pushed away from the closer silanol groups by the hydrogen bonding from the adjacent silanol to its oxygen atom, however we do not observe that this has a significant change in the energy of the system. Due to the formation of this defect all silanol are able to form a hydroxyl nest in either the short- or long-range hydrogen bonding interaction. This will cause the cluster to maintain some structural stability. The energies of the mesopore formation trends towards preferring the ring configuration with consistent more exothermic optimisation. The singular exception to this trend is the formation of Chabazite where for the first three T-sites removed the favour the adjacent configuration and then preferring the ring configuration for the fourth T-site. Together, these insights lay groundwork for understanding mesopore formation mechanisms and structural stability in zeolitic materials.

Chapter 5: Formation of Platinum cluster with

Genetic Algorithms

5.1 Introduction of Genetic Algorithms and Platinum clusters

This chapter explores the formation of platinum clusters using Genetic Algorithm (GA) methodologies [161] as implemented in the Knowledge Led Master Code (KLMC) [189] providing a robust approach to modelling and optimizing cluster configurations. KLMC calculations offer insights into the energetic landscape and atomic interactions, serving as a foundational step for identifying stable configurations. Building on these, GA techniques simulate an evolutionary process, refining and evolving candidate structures to achieve low-energy platinum clusters. GA in KLMC provides a complementary framework for predicting and understanding the structural dynamics and stability of platinum clusters at the atomic level.

5.1.1 Computational Approach

The structure prediction simulations on Pt clusters were carried out using the KLMC [161] software employing the GA [189] module. GA has proven to be a useful method to obtain geometry and energies for local (LM) and global (GM) minima on the MM energy landscape of Pt.

Genetic algorithms (GAs) offer an unbiased approach to structural optimization, initiating with a population of diverse configurations to explore the energy landscape comprehensively. The algorithm simulates Darwinian evolution, where successive generations of structures evolve by combining and refining features of "parent" structures. In this process, offspring structures are evaluated, with preference given to those exhibiting lower energy characteristics, allowing the algorithm to converge toward a set of low-energy, stable clusters over time. To diversify and refine the structural population, GAs utilises two primary mechanisms for generating new configurations:

- Crossover: This operation pairs distinct parent structures, combining their features to
 create offspring with characteristics derived from each parent. By integrating different
 structural characteristics (such a unique cluster or atom or structure database values),
 crossover enhances the likelihood of discovering novel low-energy arrangements
 within the population.
- 2. **Mutation**: To maintain diversity and introduce novel structural features, mutations are introduced into the population through a Monte Carlo approach. Mutation disrupts current structures, allowing the exploration of new configurations that may not emerge solely from crossover. This method prevents premature convergence and depletion of the population, ensuring continuous variation.

By balancing these operations, the GA effectively refines the population, selecting lowerenergy structures for further crossover while gradually eliminating high-energy candidates. In this study, the mutation rate was set to 0.8, with a self-cross ratio of 0.2, supporting both diversity and stability within the evolving population. Over successive iterations, the algorithm promotes low-energy configurations, improving the candidate structures and enhancing the probability of reaching optimal solutions. [190]

The first stage in the process is to perform a search on the interatomic potential energy surface within the GULP software. The KLMC calculations were used to obtain a base value for energy and force evaluations, and their respective local geometry optimizations. The interatomic

potentials used for the GA calculations were obtained from a mathematical equivalent (to that available in GULP) parameterization of Fabrizio Cleri and Vittorio Rosato [191] who have conducted thorough work on obtaining tight-binding potentials for transition metals such as platinum. The interatomic potentials provided consist of a repulsive Buckingham (Born-Mayer) potential and a many-body embedded atom method (EAM). The EAM includes the combination of a many-body attractive term E_a , and a repulsive two-body Born-Mayer IP E_r alluded above. The potentials are given in the form:

$$E_a = -\sum_{i} (\sum_{j} e^{-\beta \left(\frac{r_{ij}}{r_0} - 1\right)})^{\frac{1}{2}},$$

$$E_r = \sum_{i>j} B e^{-\rho r_{ij}},$$

$$E_{Buckingham} = Ae^{-R/\rho} - \frac{c}{R^6},$$

(Note the difference in the meaning or paramer ρ in the last two equations.) Parameters used in our GULP input are summarised in Table 44. The use of high-level interatomic potentials allows for a better chance of low-energy candidates being filtered out. This helps with further DFT analysis. However, interatomic potentials are those developed originally for the simulation of bulk materials, not of nanoclusters; therefore, new potentials were needed to provide more accurate results.

After the results for KLMC are collected, a subset of the lower energy results are selected for refinement using density functional theory (DFT). DFT is the most effective and widely used method in the study of transition metal clusters. The performed calculation for Pt_n was conducted within the generalized gradient approximation (GGA) to investigate the ground states by relaxing geometric structures starting from a large number of initial candidate

geometries collected from KLMC. The chosen clusters are then re-optimized utilizing: quantum mechanical theory, DFT level using the all-electron and full potential electronic structure code FHI-aims [192]. FHI-aims is a software that is a full-potential all-electron electronic structure theory package offering both DFT and "beyond-DFT" functionality. The relaxation calculation conducted in FHI-aims involved the PBEsol [193]exchange-correlation functional without including any spin polarization and a multi-step optimization procedure. The DFT calculation was conducted with the use of "light" basis sets.

Table 44:Parameters of the IP used for Pt-Pt interactions provided.

Buckingham potential					
A (eV)		ρ (Å)		C (eV Å ⁶))
24168.5173		0.261468	0.0		
Embedded A	tom Mod	lel			
EAM Function	tional EAM Density				
Туре	A	Type	A	В	r ₀
Square root	1	Baskes	7.263025	8.008	2.7747

The relative cluster energies were subsequently refined using the PBEsol0 exchange-correlation functional, which includes a 25% Hartree–Fock-like electron exchange, by performing single point energy calculations with the "tight" basis set. This change in functional allowed for the comparison between the different exchange-correlation functionals and their respective binding energies. Geometry optimization was achieved without imposing symmetry constraints.

The calculation was then placed through GULP code another time with the results obtained from FHI-aims. These new optimization calculations are used to determine whether the FHI-aims results return to the previous GULP geometries. The results from FHI-aims were consequently used in GA based fit to obtain a new set of potential parameters to be used to more accurately simulate the results obtained by FHI-aims. The calculation from the latter GA started from generating random parameter values between the bulk interatomic potentials of nickel and platinum (both group 10 metals). The sum of squares (the cost, or error function) calculations are conducted to achieve a realistic energy landscape. The second set of deterministic calculations were conducted to obtain the sum of the square by systematically varying parameters on a grid. However, only the value of A and ρ were selected as variables. The second set of calculations involved acquiring results for both a fixed cluster as well as a relaxed fit.

The GA, as discussed previously, generates a population of possible candidate structures at a stationary point on the energy landscape and proceed to move towards lower energy results. For each value of n, different structures (isomers) are discovered and recorded. The top candidates are selected by observing the energy of formation, E_f , and classified from lowest to highest in energy.

5.2 Results and Discussion

Here, results of GA simulations are split in three groups from the small nontrivial n=4 size up to n=10 before the parameter refinement is introduced.

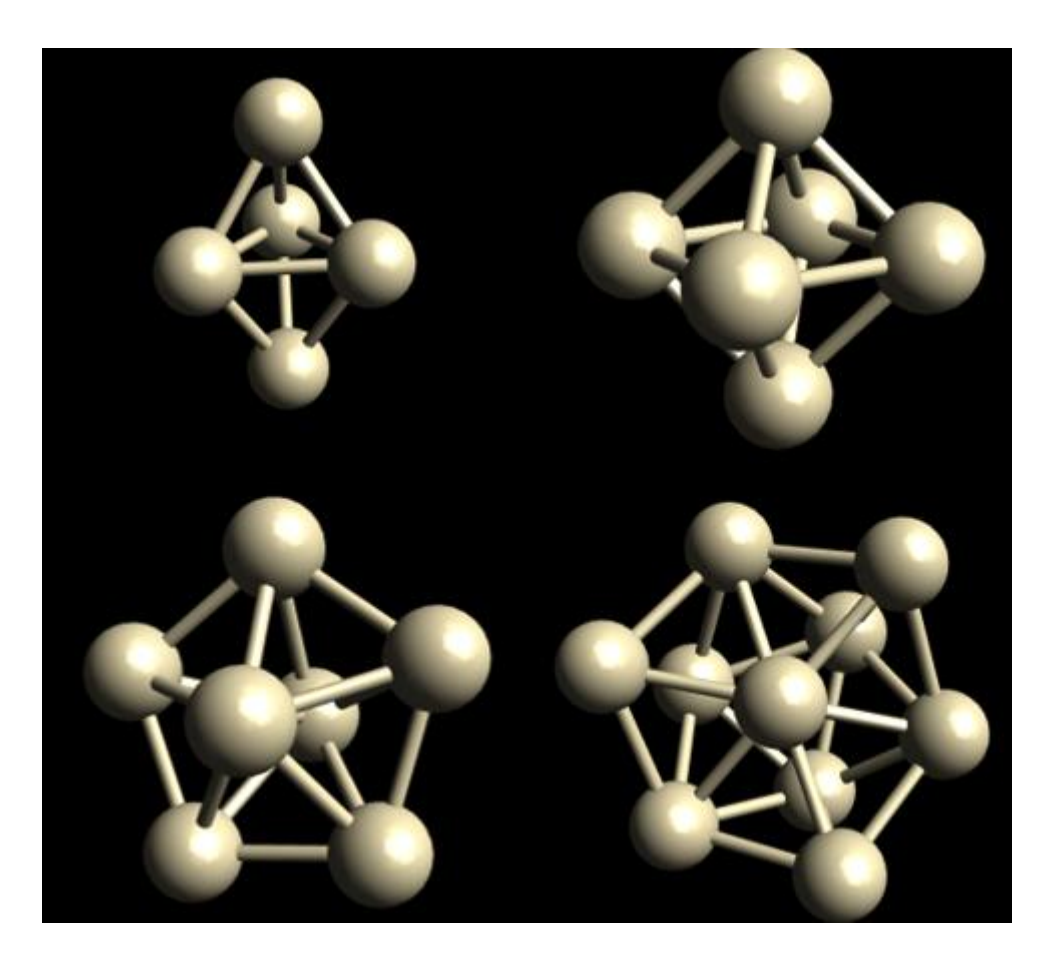


Figure 26: Lowest energy Platinum clusters generated from GULP with the help of Genetic Algorithms. Top left Pt5, top right Pt6, bottom left Pt7 and bottom right Pt10.

5.2.1 Pt₄₋₆ clusters

Using KLMC, global minima were identified for platinum clusters with n<7, revealing a unique energy structure for each size. This finding highlights the well-defined stability and geometries of small platinum clusters. For n=4, the only possible structure is a tetrahedron with a bond length of 2.4893 Å and E_f = -4.388 eV/Pt using KLMC (E_f is the binding energy per Pt atom in the cluster), consistent with its high symmetry and minimal strain. At n=5, the trigonal bipyramidal geometry emerges, as shown in Figure 26 top left, characterized by E_f = -4.540 eV/Pt and having a slightly longer bond length of 2.5087 Å, reflecting a balance between bonding interactions and spatial constraints. For n=6, the mono-capped trigonal bipyramidal structure is the global minimum, exhibiting bond lengths of 2.4968 Å and 2.5863 Å with E_f = -4.624 eV/Pt as shown in Figure 26 in the top right. These geometries and energy trends align well with previous studies that suggest small platinum clusters preferentially adopt compact, high-symmetry configurations to maximize cohesive energy while minimizing strain. The systematic increase in total energies with cluster size underscores the growing stability of larger clusters, consistent with theoretical predictions and experimental observations. These results provide foundational insights into the structural evolution of small platinum clusters, which are critical for understanding their catalytic properties. [191]

5.2.2 Pt₇ clusters

For n=7, four distinct minima structures were identified using KLMC with GA calculations, as summarized in Table 45. The lowest energy structure was found to be pentagonal bipyramidal, as shown in Figure 26 bottom left, characterized by $E_f = -4.682$ eV/Pt and bond lengths ranging from 2.5456 Å to 2.8050 Å.

Table 45: Energy ranking of a single Pt atom in Pt₇ per Pt clusters of KLMC and FHI-aims results as well as bond length of KLMC clusters. The energy rankings are calculated with respect to the lowest energy cluster produced by KLMC.

Ranking	KLMC results (eV)	FHI-AIMS results (eV)	Bond Length (Å)
1	0.0000	0.0000	2.5456-2.8050
2	0.0357	-0.0915	2.5238-2.6187
3	0.0711	-0.1116	2.4907-2.6604
4	0.0825	-0.0482	2.5189-2.6647

The remaining three clusters were variations formed by capping minimum-energy structures of smaller platinum clusters, highlighting a systematic growth pattern. Among these, the second and third-ranked structures were mono-capped bipyramids. However, after optimization using the quantum mechanical (QM) software FHI-aims, the third structure emerged as the global minimum, surpassing the original lowest-energy configuration. This shift in stability is attributed to structural modifications during the QM optimization process, which underscores the limitations of interatomic potentials in fully reproducing QM-level accuracy. These findings demonstrate that while the KLMC potentials provide a useful approximation, they require refinement to ensure consistency with QM results. Such insights are essential for developing more accurate potential models for platinum clusters and beyond.[191]

5.2.3 Pt₁₀ clusters

The clusters for n=10 are as shown by Table 46. Twenty-three different cluster configurations were determined by the KLMC software. The E_f ranged from -4.882 to -4.765 eV per Pt cluster. The top clusters generated by KLMC was a pentagonal bipyramid with the addition of 3 capping Pt atoms. Most low energy clusters have this pentagonal bipyramid backbone with a variety of different conformation

of capping atoms. The higher energy cluster have the trigonal bipyramid backbone that are stack together into various structures. The bond lengths are maintained from the lower energy clusters.

Table 46: Energy ranking of a single Pt atom in Pt₁₀ per Pt clusters of KLMC and FHI-aims results as well as bond length of KLMC clusters. The energy rankings are calculated with respect to the lowest energy cluster produced by KLMC.

FHI-AIMS results (eV) Bond Length (Å)

Ranking KLMC results (eV)

0.0604

1			
2	0.0000	0.0000	2.5252-2.8489
2	0.0296	0.0291	2.5217-2.7500
3	0.02,0	V.V 2 51	20217 207000
,	0.0331	-0.0637	2.4948-2.6802
4	0.0378	-0.0523	2.5095-2.8492
5	0.0378	-0.0323	2.3093-2.0492
	0.0383	0.0090	2.5272-2.7990
6			
7	0.0406	0.0240	2.5389-3.1888
/	0.0455	-0.0991	2.5074-2.8539
8			
	0.0471	-0.0566	2.5053-2.8699
0			

-0.0900

2.5197-2.8717

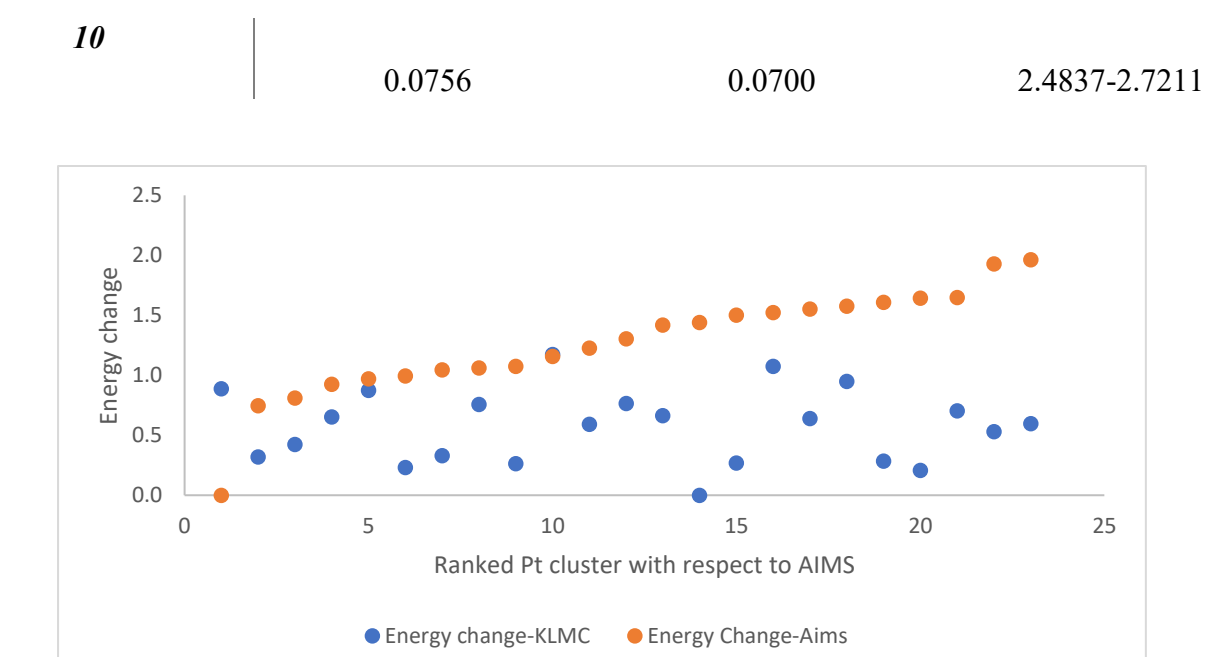


Figure 27: The energy difference between the lowest ranked cluster and higher Pt clusters energy cluster. Comparing the Pt₁₀ clusters difference between the KLMC and FHI-aims energies.

As shown in Figure 27, the energy change between the two sets of results do not sync up. The problem highlighted by this discovery is that the lowest energy structure of KLMC is only the fourteenth lowest energy structure for FHI-aims. This disparity also applies to the FHI-aims top structure which is the twentieth lowest energy structure in GULP. The fact that this energy does not show a parallel graph tells us that the results for the same geometries produce qualitatively different energies. Therefore, the potentials used by KLMC do not match those of FHI-aims calculations.

5.3.4 Pt₁₃ clusters

A total of 44 platinum clusters with n=13 were generated using the KLMC software, with the most stable structure for n=13 identified as an icosahedron. The E_f of this icosahedral cluster was calculated as -4.993 eV/Pt using KLMC. However, the most stable cluster according to the QM optimizer FHI-aims was the twenty-fourth-ranked cluster from the KLMC set, with an E_f of -518,142.361 eV. As cluster energy for KLMC increases, the difference is that the results for FHI-AIMS find cluster that are lower in energy than those found in KLMC, as shown in Figure 28 and Table 47. The lack of correlation between the energy and geometry rankings produced by KLMC and FHI-aims calculations indicates a significant disparity in results. This inconsistency underscores the limitations of the current potentials used in KLMC, which fail to reproduce QM-level accuracy in energy or geometry. Addressing this gap requires the development and application of a new set of interatomic potentials to reconcile these differences and improve the predictive reliability of KLMC for platinum clusters.

Table 47: Energy ranking of a single Pt atom in Pt₁₃ clusters of KLMC and FHI-aims results as well as bond length of KLMC clusters. The energy rankings are calculated with respect to the lowest energy cluster produced by KLMC.

Ranki	ing	KLMC results (eV)	FHI-AIMS results (eV)	Bond Length (Å)
1		0.0000	0.0000	2.5664-2.6985
2		0.0446	-0.1390	2.5443-2.7382
3		0.0453	-0.1156	2.5511-2.8225
4		0.0460	-0.1711	2.4891-2.9127
5		0.0471	-0.1084	2.5513-2.7197
6		0.0509	-0.1566	2.5073-2.8580
7		0.0526	-0.1506	2.5102-2.8730
8		0.0542	-0.0804	2.5280-2.7800
9		0.0580	-0.1088	2.5053-3.1168
10		0.0616	-0.1219	2.4997-2.8422
	3.0			
	2.5			
	Energy change 0.1 cor 0.2			•
	بِ 1.5	• • • •	•	
	(S) 1.0			
	迈 0.5			•
	0.0			
	0.0) 10	20 30	40 50
			Number of cylces	
		● Energy change	-KLMC • Energy Change-AIMS	

Figure 28: The energy difference between the lowest ranked cluster and higher energy Pt clusters. Comparing the Pt₁₃ clusters difference between the KLMC and FHI-aims energies.

5.4 New Potentials for Platinum Clusters

The final focus of this thesis is the development of a new set of potentials to more accurately replicate the results produced by FHI-aims. This approach involved employing additional GA methods to randomly modify the parameters A, ρ for the Buckingham potentials, as well as, EAM-A, EAM- β and EAM- η 0 for the EAM_density Baskes potentials. The objective was to minimize the sum of squares (or the cost function) differences across a wide range of potentials, comparing the target values for platinum, as previously stated, with the reference potentials for nickel. Nickel was chosen due to its similar electronic configuration, sharing the same number of outer d-electrons as platinum (both being group 10 elements). The sum of squares differences was used to quantify the geometric deviation from the FHI-aims results. A smaller sum of squares indicates a closer match in geometry between the new GULP potentials and the FHI-aims results. The optimized potentials obtained from the GA calculations are presented in Table 48.

Table 48: New potentials generated by GA calculations for platinum when observing sum of squares calculations.

Buckingham potential					
A (eV)		ρ (Å)		C (eV Å)	
25.7543926456		0.147216022894		0.0	
		Emb	edded Atom Mod	el	
EAM Functional		EAM Density			
Type	A	Type	A	β	r_0
Square root	1	Baskes	7.21422841582	4.84053683999	2.77444904817

The results indicate that the values of ρ and EAM β were significantly reduced, approximately halved compared to their original values. The lowest sum of squares was calculated to be -467.901173 using the previous potentials. This substantial reduction in the ρ factor significantly diminished the influence of the Buckingham potentials, thereby lowering the forces exerted on the Pt clusters. As a result, the atoms experienced increased mobility. However, this change caused a significant rise in the total energy of the system, with the icosahedral cluster reaching a value of -803.31210343 eV. Additionally, the bond lengths of the cluster expanded, ranging from 2.5874 Å to 2.73213 Å. This increase in bond length is inconsistent with the expected geometry of the simulated cluster. Consequently, the value of ρ was restored to its previous value from the original potentials, and the calculations were repeated to address this discrepancy.

Table 49: The energy difference between the lowest ranked cluster and higher energy cluster. Comparing the Pt₁₃ clusters difference between the KLMC, AIMS and a set of new potentials energies.

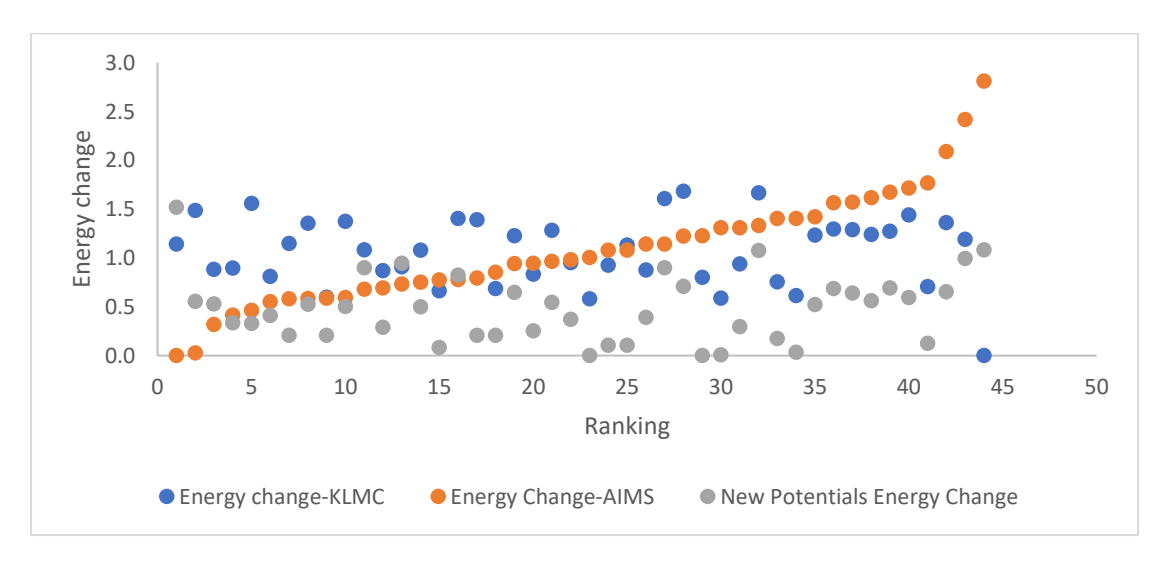


Table 49 compares the performance of the old and new potentials against the target results obtained from FHI-aims. The new potentials exhibit a smaller energy difference between

clusters compared to the previous KLMC values, indicating some improvement. However, the results still fail to replicate the continuous energy curve produced by the FHI-aims calculations. While the new potentials show better agreement for certain clusters, the most stable cluster according to FHI-aims remains equivalent to the least stable cluster in the new set, performing even worse than the previous potentials for this particular case. This highlights that the new potentials still fall short of the desired accuracy, necessitating further experimental and computational refinement to achieve a reliable set of parameters. Although the GA methods provided a promising starting point by estimating potential new values, they failed to consistently account for the energy variations in some systems. This underscores the need for additional methods and more comprehensive optimization approaches to refine the potentials further. The work so far has merely scratched the surface, and significant effort will be required to develop a robust and accurate set of potential values.

5.5 Summary and Conclusion

The clusters generated through KLMC did not yield notable improvements in the potentials, as the newly generated potential values, particularly ρ , were too low for further research applications. In contrast, the clusters optimized using FHI-aims showed promising results, aligning closely with those previously reported by other research groups. This indicates the potential reliability of FHI-aims in producing accurate cluster geometries. However, further work is necessary to develop a robust set of potentials for GULP that can effectively describe platinum clusters. Despite these challenges, the research has successfully established critical groundwork for fully characterizing the Pt cluster structures for the catalysis of propane into propene. Additionally, a series of platinum clusters of varying sizes have been generated and optimized using FHI-aims, providing a valuable foundation for future studies.

Chapter 6: Summary and Conclusion

This final chapter provides a summary of the work described in Chapters 3, 4 and 5, in addition to some comments on possible future extensions to the study.

6.1.1 Summary

In Chapter 3, we examined the formation of hydroxyl nest defects, or [4H]Si defects, in zeolite structures by removing a silicon atom and protonating the exposed oxygen atoms. The calculated formation energies of hydroxyl nests for various zeolites (e sodalite, Chabazite, ZSM-5, Mordenite) exhibit differences due to structural diversity, with energy values varying based on the framework's stability. Advanced NEB simulations reveal two proton movement mechanisms proton transfer and rotation at Brønsted acid sites within hydroxyl nest clusters, providing insights into the dynamic and catalytic behaviour of these zeolite frameworks. These findings are essential for understanding zeolite defect chemistry and optimizing zeolite materials for industrial applications.

In Chapter 4, we investigated the formation of mesopores in four zeolitic frameworks—ZSM-5, Chabazite, Faujasite, and α -Quartz by computationally removing T-sites in two different method (adjacent and ring) and analysing the resulting structural and energetic changes. Using hybrid QM/MM methods, we identified key stabilization structures of the three-membered hydrogen-bonded silanol rings, which appeared across all frameworks. ZSM-5 and Chabazite maintained stability through these silanol rings, while Faujasite and α -Quartz, favoured longer silanol chains, exhibiting distinctive hydrogen-bonding patterns due to spatial availability. α -Quartz displayed limited defect stability, emphasizing its structural rigidity due to this limited

spatial availability. As mesopores expanded, the formation energy becomes more exothermic until more than five T sites or more are removed revealing a threshold at which frameworks begin to destabilize and become less exothermic. These findings highlight how zeolite geometry and bonding patterns affect mesopore stability, offering insights into the design of porous materials for applications in catalysis and adsorption.

In Chapter 5, we discussed the formation of Pt clusters up to the size n=12 with the help of GA and optimised using two different techniques giving us a wide range of clusters to introduced to various zeolitic frameworks. The clusters generated through KLMC did not yield improved potentials, as the resulting values of ρ were too low for further research applications. However, the clusters produced using FHI-aims closely resemble those documented by other research groups and appear promising for continued study.

The main objective of developing Py-Chemshell for the use in studying in zeolites was a success. The ability to reproduce results from the much older TCL-Chemshell with the hope to overtake the capabilities of its predecessor are being developed. The work of previously accomplished in the field of hydroxyl nest has successfully replicated and now has been taking in a unique way with this thesis. The observation of the possibility of proton rotation in the hydroxyl nest could explain hydroxyl nest rearrangement with the defect sites for lower energy configurations. The subsequent work into the expansion of the defect site to generate mesopores has never been accomplished at this level of theory. We now have a better understanding of the structure and energies that these zeolites would take and their stability with exothermic reactions (in vacuum, solubility would produce reaction with higher energy demands). The observation that all zeolites exhibit the same hydrogen bonding and the trisilanol ring formation showing that when silicon is removed the newly formed O-H bond will align themselves in this configuration to reduce the energy of the system.

6.1.2 Future Work

The field of zeolitic studies is an ever-expanding area of interest for scientist, and as the field progresses the study of detailed catalytic processes within zeolite frameworks will be more of a focus. The study of catalysis effected b the Pt clusters in ZSM-5 will be of particular interest. The main obstacle for QM/MM Chemshell based zeolitic calculations is a lack of an advanced MD simulations driver to allow for the observation of the formation mechanism of the hydroxyl nest as well as the potential for the reorganization of the framework when pores aggregate. The use of spectroscopic techniques such as *in situ operando* DRIFTS, XANES, EPR, IR, RAMAN and DRUVS [194], can provide indirect evidence regarding the formation of the hydroxyl nest and incorporation of Pt clusters. Further work linking modelling to spectroscopic signatures and exploring dynamical effects will be of particular importance.

The next stage in this work would logically be to combine the hydroxyl nest study with the Pt cluster. A fundamental understanding for the formation of the Pt cluster in the framework via seeding ions or nanocluster binding with the hydroxyl nest could explain why zeolites make such excellent catalyst in industry. Additional work is necessary to develop a robust set of new potentials for GULP for platinum clusters. Overall, this study has successfully established insights needed to describe the catalytic reaction pathway for propane-to-propene conversion. A series of new and improved platinum clusters of varying sizes could be generated and optimized within FHI-aims, marking significant progress in this area and providing better results down the line. Understanding hydroxyl nest as a catalytic site in zeolites will be essential in gaining insight into how zeolite react with transition metal ions.

References

- 1. Parker, S. and A. Kombanal, *How Many Molecules Can Fit in a Zeolite Pore? Implications for the Hydrocarbon Pool Mechanism of the Methanol-to-Hydrocarbons Process.* Catalysts, 2021. **11**: p. 1204.
- 2. Downing, C.A., A.A. Sokol, and C.R.A. Catlow, *The reactivity of CO2 and H2 at trapped electron sites at an oxide surface.* Physical Chemistry Chemical Physics, 2014. **16**(39): p. 21153-21156.
- 3. Salahudeen, N., A Review on Zeolite: Application, Synthesis and Effect of Synthesis Parameters on Product Properties. Chemistry Africa, 2022. **5**(6): p. 1889-1906.
- 4. Marcilly, C.R., Where and how shape selectivity of molecular sieves operates in refining and petrochemistry catalytic processes. Topics in Catalysis, 2000. **13**(4): p. 357-366.
- 5. Corma, A., et al., *Preparation, characterisation and catalytic activity of ITQ-2, a delaminated zeolite.* Microporous and Mesoporous Materials, 2000. **38**(2): p. 301-309.
- 6. Primo, A. and H. Garcia, *Zeolites as catalysts in oil refining.* Chemical Society Reviews, 2014. **43**(22): p. 7548-7561.
- 7. Colella, C. and A.F. Gualtieri, *Cronstedt's zeolite*. Microporous and Mesoporous Materials, 2007. **105**(3): p. 213-221.
- 8. Barrer, R.M. and M.B. Makki, *MOLECULAR SIEVE SORBENTS FROM CLINOPTILOLITE*. Canadian Journal of Chemistry-Revue Canadienne De Chimie, 1964. **42**(6): p. 1481-&.
- 9. Robert J Argauer, G.R.L., *Crystalline zeolite zsm-5 and method of preparing the same*, M.O. Corp, Editor. 1969.
- 10. Demikhova, N.R., et al., *Isomerization of Xylenes (a Review)*. Petroleum Chemistry, 2021. **61**(11): p. 1158-1177.
- 11. E.M. Flanigen, J.C.J., Herman van Bekkum, *Introduction to Zeolite Science and Practice*. Vol. 58. 1991: Elsevier.
- 12. Wilson, S.T., et al., *Aluminophosphate molecular sieves: a new class of microporous crystalline inorganic solids.* Journal of the American Chemical Society, 1982. **104**(4): p. 1146-1147.
- 13. Weitkamp, J., Zeolites and catalysis. Solid State Ionics, 2000. 131(1–2): p. 175-188.
- 14. C. T. Kresge, M.E.L., W. J. Roth, J. C. Vartuli & J. S. Beck *Ordered mesoporous molecular sieves synthesized by a liquid-crystal template mechanism.* Nature, 1992. **359**: p. 710–712.
- 15. Corma, A., From Microporous to Mesoporous Molecular Sieve Materials and Their Use in Catalysis. Chemical Reviews, 1997. **97**(6): p. 2373-2420.
- 16. Svetlana, M., G. Julien, and V. Valentin, *Nanosized zeolites: Quo Vadis?* Comptes Rendus. Chimie, 2016. **19**(1-2): p. 183-191.
- 17. Lezcano-González, I., et al., Structure-Activity Relationships in Highly Active Platinum-Tin MFItype Zeolite Catalysts for Propane Dehydrogenation. ChemCatChem, 2022. **14**(7): p. e202101828.
- 18. Lu, Y., et al., *Open-Source, Python-Based Redevelopment of the ChemShell Multiscale QM/MM Environment.* Journal of Chemical Theory and Computation, 2019. **15**(2): p. 1317-1328.
- 19. Migues, A.N., et al., *On the Rational Design of Zeolite Clusters.* ACS Catalysis, 2015. **5**(5): p. 2859-2865.
- 20. Fermann, J.T., et al., *Modeling Proton Transfer in Zeolites: Convergence Behavior of Embedded and Constrained Cluster Calculations.* Journal of Chemical Theory and Computation, 2005. **1**(6): p. 1232-1239.
- 21. Paul Sherwood, A.H.d.V., Simon J. Collins, Stephen P. Greatbanks, Neil A. Burton, Mark A. Vincent and Ian H. Hillier, *Computer simulation of zeolite structure and reactivity using embedded cluster methods.* Faraday Discuss, 1997. **106**: p. 79-92.

- 22. Greatbanks, S.P., et al., ADSORPTION ENERGIES OF NH3 AND NH4+ IN ZEOLITES AN EMBEDDED-CLUSTER MODEL INCLUDING ELECTRON CORRELATION. Chemical Physics Letters, 1995. **234**(4-6): p. 367-372.
- 23. Sherwood, P., et al., *QUASI: A general purpose implementation of the QM/MM approach and its application to problems in catalysis.* Journal of Molecular Structure-Theochem, 2003. **632**: p. 1-28.
- 24. C. Baerlocher, W.H.M., D. H. Olson., *Atlas of zeolite framework types*. 6th ed. 2007: Structure Commnission of the International Zeolite Association.
- 25. Davis, M.E., *Ordered porous materials for emerging applications.* Nature, 2002. **417**(6891): p. 813-821.
- 26. Kianfar, E., *Synthesis and Characterization of AIPO4/ZSM-5 Catalyst for Methanol Conversion to Dimethyl Ether.* Russian Journal of Applied Chemistry, 2018. **91**(10): p. 1711-1720.
- 27. Ramesh, K. and D.D. Reddy, *Chapter Four Zeolites and Their Potential Uses in Agriculture*, in *Advances in Agronomy*, D.L. Sparks, Editor. 2011, Academic Press. p. 219-241.
- 28. de Magalhães, L.F., et al., *Zeolite Application in Wastewater Treatment*. Adsorption Science & Technology, 2022. **2022**: p. 4544104.
- 29. Souza, I.M.S., et al., *Zeolites as Ingredients of Medicinal Products*. Pharmaceutics, 2023. **15**(5).
- 30. Ch. Baerlocher, L.B.M., H. Gies and B. Marler, *Database of Disordered Zeolite Structures*:. 2024.
- 31. Townsend, R.P. and E.N. Coker, *Chapter 11 Ion exchange in zeolites*, in *Studies in Surface Science and Catalysis*, H. van Bekkum, et al., Editors. 2001, Elsevier. p. 467-524.
- 32. Weitkamp, J., Zeolites and catalysis. Solid State Ionics, 2000. 131(1): p. 175-188.
- 33. Kordala, N. and M. Wyszkowski, *Zeolite Properties, Methods of Synthesis, and Selected Applications*. Molecules, 2024. **29**(5).
- 34. Serrano, D.P., et al., *Synthesis and crystallization mechanism of zeolite TS-2 by microwave and conventional heating.* Microporous and Mesoporous Materials, 2004. **69**(3): p. 197-208.
- 35. Pérez-Botella, E., S. Valencia, and F. Rey, *Zeolites in Adsorption Processes: State of the Art and Future Prospects.* Chemical Reviews, 2022. **122**(24): p. 17647-17695.
- 36. A. A. Sokol, C.R.A.C., J. M. Garcés, A. Kuperman, *Transformation of hydroxyl nests in microporous aluminosilicates upon annealing.* Journal of Physics: Condensed Matter, 2004. **16**(27).
- 37. Veronique Van Speybroeck, K.H., Lennart Joos, Michel Waroquier, Robert G. Bellb, C. Richard A. Catlow, *Advances in theory and their application within the field of zeolite chemistry*. Chemical Society Reviews, 2015.
- 38. Minkee Choi, K.N., Jeongnam Kim, Yasuhiro Sakamoto, Osamu Terasaki & Ryong Ryoo, *Stable single-unit-cell nanosheets of zeolite MFI as active and long-lived catalysts*. Nature, 2009. **461**: p. 246–249.
- 39. Dong Zhai, Y.L., Huimin Zheng, Liang Zhao, Jinsen Gao, Chunming Xu, Baojian Shen *A first-principles evaluation of the stability, accessibility, and strength of Brønsted acid sites in zeolites.* Journal of Catalysis, 2017. **352**: p. 627-637.
- 40. Lee, S., Y. Park, and M. Choi, *Cooperative Interplay of Micropores/Mesopores of Hierarchical Zeolite in Chemical Production*. ACS Catalysis, 2024. **14**(3): p. 2031-2048.
- 41. Bai, R., et al., *Creating Hierarchical Pores in Zeolite Catalysts*. Trends in Chemistry, 2019. **1**(6): p. 601-611.
- 42. Usman, K., et al., *Utilizing Silica from Rice Hull for the Hydrothermal Synthesis of Zeolite Y.* 2018. **29**: p. 17-21.
- 43. Chen, N.Y., Shape Selective Catalysis in Industrial Applications. 1996: Boca Raton.
- 44. D Verboekend, J.P.-R., *Design of hierarchical zeolite catalysts by desilication*. Catal. Sci. Technol., 2011. **1**: p. 879-890.

- 45. Ogura, M., et al., *Alkali-treatment technique* new method for modification of structural and acid-catalytic properties of ZSM-5 zeolites. Applied Catalysis A: General, 2001. **219**(1): p. 33-43.
- 46. Johan C. Groen, J.A.M.a.J.P.-R., *Desilication: on the controlled generation of mesoporosity in MFI zeolites*. Journal of Materials Chemistry, 206. **16**(22): p. 2121-2131.
- 47. Csicsery, S.M., Shape-selective catalysis in zeolites. Zeolites, 1984. **4**(3): p. 202-213.
- 48. Schroeder, C. and M. Sanchez-Sanchez, *Unlocking the potential for pseudo-molecular catalysts via understanding the activity of transition metal ionic species in zeolites.* Chem Catalysis, 2024: p. 101130.
- 49. Haw, J.F., *Zeolite acid strength and reaction mechanisms in catalysis.* Physical Chemistry Chemical Physics, 2002. **4**(22): p. 5431-5441.
- 50. Charik, F.Z., et al., *In-depth exploration of defects in zeolite membranes: Typology, formation, characterization and healing.* Journal of Environmental Chemical Engineering, 2024. **12**(3): p. 112918.
- 51. Lin, C.C.H., K.A. Dambrowitz, and S.M. Kuznicki, *Evolving applications of zeolite molecular sieves*. The Canadian Journal of Chemical Engineering, 2012. **90**(2): p. 207-216.
- 52. Wang, Y. and D. Zhao, *Beyond Equilibrium: Metal–Organic Frameworks for Molecular Sieving and Kinetic Gas Separation*. Crystal Growth & Design, 2017. **17**(5): p. 2291-2308.
- 53. Auroux, A., et al., Study of the acidity of ZSM-5 zeolite by microcalorimetry and infrared spectroscopy. Journal of the Chemical Society, Faraday Transactions 1: Physical Chemistry in Condensed Phases, 1979. **75**(0): p. 2544-2555.
- 54. Roeffaers, M.B.J., et al., *Morphology of Large ZSM-5 Crystals Unraveled by Fluorescence Microscopy.* Journal of the American Chemical Society, 2008. **130**(17): p. 5763-5772.
- 55. Van Speybroeck, V., et al., *Advances in theory and their application within the field of zeolite chemistry.* Chemical Society Reviews, 2015. **44**(20): p. 7044-7111.
- 56. Catlow, R., et al., *Molecular Modelling in Zeolite Science*, in *Studies in surface science and catalysis*. 2007, Elsevier. p. 659-700.
- 57. Kohale, R.L., et al., *Chapter 1 Introduction to phosphate phosphors*, in *Optical Properties of Phosphate and Pyrophosphate Compounds*, R.L. Kohale, et al., Editors. 2021, Woodhead Publishing. p. 1-53.
- 58. Cejka, J. and H. van Bekkum, *Zeolites and Ordered Mesoporous Materials: Progress and Prospects: The 1st FEZA School on Zeolites, Prague, Czech Republic, August 20-21, 2005.* 2005: Elsevier Science.
- 59. Salian, A., et al., *A review on high entropy silicides and silicates: Fundamental aspects, synthesis, properties.* International Journal of Applied Ceramic Technology, 2023. **20**(5): p. 2635-2660.
- 60. Hao, S.-M., et al., Hollow Manganese Silicate Nanotubes with Tunable Secondary Nanostructures as Excellent Fenton-Type Catalysts for Dye Decomposition at Ambient Temperature. Advanced Functional Materials, 2016. **26**(40): p. 7334-7342.
- 61. Zhu, Z.-S., et al., *Preforming abundant surface cobalt hydroxyl groups on low crystalline* flowerlike Co3(Si2O5)2(OH)2 for enhancing catalytic degradation performances with a critical nonradical reaction. Applied Catalysis B: Environmental, 2020. **261**: p. 118238.
- 62. Hao, S.-M., et al., *Hierarchical mesoporous cobalt silicate architectures as high-performance sulfate-radical-based advanced oxidization catalysts.* Journal of Colloid and Interface Science, 2019. **545**: p. 128-137.
- 63. Egeblad, K., et al., *Templating Mesoporous Zeolites*. Chemistry of Materials, 2008. **20**(3): p. 946-960.
- 64. Szostak, R., *Molecular Sieves for Use in Catalysis*, in *Molecular Sieves: Principles of Synthesis and Identification*, R. Szostak, Editor. 1989, Springer Netherlands: Dordrecht. p. 1-50.

- 65. Xiao, X., et al., *Tuning the density of Brønsted acid sites on mesoporous ZSM-5 zeolite for enhancing light olefins selectivity in the catalytic cracking of n-octane.* Microporous and Mesoporous Materials, 2022. **330**: p. 111621.
- 66. Huang, X., et al., Catalyst Design Strategies towards Highly Shape-selective HZSM-5 for Paraxylene through Toluene Alkylation. Green Energy & Environment, 2020. **5**.
- 67. Mohamed, R., I. Ibrahim, and M. Mohamed, *Synthesis and modification of ZSM-5 with manganese and lanthanum and their effects on decolorization of indigo carmine dye.* Applied Catalysis A: General, 2006. **299**: p. 95-102.
- 68. Liu, W., et al., Adsorption Properties of ZSM-5 Molecular Sieve for Perfluoroisobutyronitrile Mixtures and Its Fluorocarbon Decomposition Products. Chemosensors, 2022. **10**(4): p. 121.
- 69. Aouaini, F., et al., Adsorption of CO2 on ZSM-5 Zeolite: Analytical Investigation via a Multilayer Statistical Physics Model. Applied Sciences, 2022. **12**(3): p. 1558.
- 70. Arik, I.C., J.F. Denayer, and G.V. Baron, *High-temperature adsorption of n-alkanes on ZSM-5 zeolites: influence of the Si/Al ratio and the synthesis method on the low-coverage adsorption properties.* Microporous and Mesoporous Materials, 2003. **60**(1): p. 111-124.
- 71. LLC, A.M., ZSM-5 Zeolite Socony Mobil—5. 2019: https://www.acsmaterial.com.
- 72. Dent, L. and J. Smith, *Crystal structure of chabazite, a molecular sieve.* Nature, 1958. **181**(4626): p. 1794-1796.
- 73. Thrush, K.A. and S.M. Kuznicki, *Characterization of chabazite and chabazite-like zeolites of unusual composition.* Journal of the Chemical Society, Faraday Transactions, 1991. **87**(7): p. 1031-1035.
- 74. Xiong, R., et al., Solvent-tuned hydrophobicity for faujasite-catalyzed cycloaddition of biomass-derived dimethylfuran for renewable p-xylene. Green Chemistry, 2014. **16**(9): p. 4086-4091.
- 75. Hriljac, J.A., et al., *Powder Neutron Diffraction and 29Si MAS NMR Studies of Siliceous Zeolite-* Y. Journal of Solid State Chemistry, 1993. **106**(1): p. 66-72.
- 76. Tempelman, C.H.L., et al., *Texture, acidity and fluid catalytic cracking performance of hierarchical faujasite zeolite prepared by an amphiphilic organosilane.* Fuel Processing Technology, 2015. **139**: p. 248-258.
- 77. Wilson, S.M.W. and F.H. Tezel, *Direct Dry Air Capture of CO2 Using VTSA with Faujasite Zeolites.* Industrial & Engineering Chemistry Research, 2020. **59**(18): p. 8783-8794.
- 78. Gallezot, P., *The State and Catalytic Properties of Platinum and Palladium in Faujasite-type Zeolites.* Catalysis Reviews, 1979. **20**(1): p. 121-154.
- 79. Fantini, R., et al., *Thermal behavior of high silica mordenite*. Microporous and Mesoporous Materials, 2020. **294**: p. 109882.
- 80. Barrer, R.M. and J. Klinowski, *Ion exchange in mordenite*. Journal of the Chemical Society, Faraday Transactions 1: Physical Chemistry in Condensed Phases, 1974. **70**(0): p. 2362-2367.
- 81. Niwa, M., N. Katada, and K. Okumura, *Characterization and Design of Zeolite Catalysts: Solid Acidity, Shape Selectivity and Loading Properties.* 2010: Springer Berlin Heidelberg.
- 82. Breck, D.W., Zeolite molecular sieves: structure, chemistry, and use. 1973: Wiley.
- 83. Hincapie, B.O., et al., *Synthesis of mordenite nanocrystals*. Microporous and Mesoporous Materials, 2004. **67**(1): p. 19-26.
- 84. d'Amour, H., W. Denner, and H. Schulz, *Structure determination of [alpha]-quartz up to 68 x* 108 Pa. Acta Crystallographica Section B, 1979. **35**(3): p. 550-555.
- 85. Gatta, G.D. and P. Lotti, *Chapter 1 Systematics, crystal structures, and occurrences of zeolites*, in *Modified Clay and Zeolite Nanocomposite Materials*, M. Mercurio, B. Sarkar, and A. Langella, Editors. 2019, Elsevier. p. 1-25.
- 86. Schroeder, C., et al., *Disentangling Brønsted Acid Sites and Hydrogen-Bonded Silanol Groups in High-Silica Zeolite H-ZSM-5*. The Journal of Physical Chemistry C, 2020. **124**(42): p. 23380-23386.

- 87. Schroeder, C., et al., *Hydrogen Bond Formation of Brønsted Acid Sites in Zeolites.* Chemistry of Materials, 2020. **32**(4): p. 1564-1574.
- 88. Llewellyn, P.L. and G. Maurin, *Chapter 17 Gas Adsorption in Zeolites and Related Materials*, in *Studies in Surface Science and Catalysis*, J. Čejka, et al., Editors. 2007, Elsevier. p. 555-XVI.
- 89. Reeve, P.J. and H.J. Fallowfield, *Natural and surfactant modified zeolites: A review of their applications for water remediation with a focus on surfactant desorption and toxicity towards microorganisms*. Journal of Environmental Management, 2018. **205**: p. 253-261.
- 90. Fruijtier-Pölloth, C., *The safety of synthetic zeolites used in detergents*. Archives of Toxicology, 2009. **83**(1): p. 23-35.
- 91. Sunil Kumar, M., et al., *A review of comparison between the traditional catalyst and zeolite catalyst for ammonia-selective catalytic reduction of NOx.* Fuel, 2023. **344**: p. 128125.
- 92. Qazi, U.Y., et al., A Comprehensive Review on Zeolite Chemistry for Catalytic Conversion of Biomass/Waste into Green Fuels. Molecules, 2022. **27**(23).
- 93. Li, Y., L. Li, and J. Yu, *Applications of Zeolites in Sustainable Chemistry*. Chem, 2017. **3**(6): p. 928-949.
- 94. Xu, B., et al., Catalytic activity of Brønsted acid sites in zeolites: Intrinsic activity, rate-limiting step, and influence of the local structure of the acid sites. Journal of Catalysis, 2006. **244**(2): p. 163-168.
- 95. Palčić, A. and V. Valtchev, *Analysis and control of acid sites in zeolites.* Applied Catalysis A: General, 2020. **606**: p. 117795.
- 96. Schröder, K.-P., et al., Siting of AI and bridging hydroxyl groups in ZSM-5: A computer simulation study. Zeolites, 1992. **12**(1): p. 20-23.
- 97. Sauer, J. and R. Zahradník, *Quantum chemical studies on zeolites and silica*. International Journal of Quantum Chemistry, 1984. **26**(5): p. 793-822.
- 98. Catlow, C.R.A., et al., *Modelling of structure and reactivity in zeolites*, in *Studies in Surface Science and Catalysis*, L. Bonneviot and S. Kaliaguine, Editors. 1995, Elsevier. p. 87-100.
- 99. Senderov, E., I. Halasz, and D.H. Olson, *On existence of hydroxyl nests in acid dealuminated zeolite Y.* Microporous and Mesoporous Materials, 2014. **186**: p. 94-100.
- 100. Barrer, R.M., Zeolites and clay minerals as sorbents and molecular sieves. 1978.
- 101. Kerr, G.T., Chemistry of crystalline aluminosilicates. V. Preparation of aluminum-deficient faujasites. The Journal of Physical Chemistry, 1968. **72**(7): p. 2594-2596.
- 102. Kerr, G.T., Chemistry of crystalline aluminosilicates. VI. Preparation and properties of ultrastable hydrogen zeolite Y. The Journal of Physical Chemistry, 1969. **73**(8): p. 2780-2782.
- 103. Lee, E.F.T. and L.V.C. Rees, *Dealumination of sodium Y zeolite with hydrochloric acid.* Journal of the Chemical Society, Faraday Transactions 1: Physical Chemistry in Condensed Phases, 1987. **83**(5): p. 1531-1537.
- 104. Capasso, S., et al., *Removal of Humic Substances from Water by Means of Calcium-Ion-Enriched Natural Zeolites*. Water Environment Research, 2007. **79**(3): p. 305-309.
- 105. Terdkiatburana, T., S. Wang, and M.O. Tadé, *Competition and complexation of heavy metal ions and humic acid on zeolitic MCM-22 and activated carbon.* Chemical Engineering Journal, 2008. **139**(3): p. 437-444.
- 106. Wright, K., R. Freer, and C.R.A. Catlow, *The energetics and structure of the hydrogarnet defect in grossular: A computer simulation study.* Physics and Chemistry of Minerals, 1994. **20**(7): p. 500-503.
- 107. Holzinger, J., et al., *Distribution of Aluminum over the Tetrahedral Sites in ZSM-5 Zeolites and Their Evolution after Steam Treatment.* The Journal of Physical Chemistry C, 2018. **122**(27): p. 15595-15613.
- 108. Resasco, D.E., et al., *Interaction of water with zeolites: a review.* Catalysis Reviews, 2021. **63**(2): p. 302-362.
- 109. Kerr, G.T., Chemistry of crystalline aluminosilicates: VII. Thermal decomposition products of ammonium zeolite Y. Journal of Catalysis, 1969. **15**(2): p. 200-204.

- 110. Blasco, T., et al., *The state of Ti in titanoaluminosilicates isomorphous with zeolite .beta.* Journal of the American Chemical Society, 1993. **115**(25): p. 11806-11813.
- 111. Scarano, D., et al., Fourier-transform infrared and Raman spectra of pure and Al-, B-, Ti- and Fe-substituted silicalites: stretching-mode region. Journal of the Chemical Society, Faraday Transactions, 1993. **89**(22): p. 4123-4130.
- 112. Nagy, J.B., Z. Gabelica, and E.G. Derouane, A CROSS-POLARIZATION MAGIC-ANGLE-SPINNING 29Si-n.m.r. IDENTIFICATION OF THE SILANOL GROUP RESONANCE IN ZSM 5 ZEOLITES. Chemistry Letters, 1982. **11**(7): p. 1105-1108.
- 113. Freude, D., et al., *NMR studies concerning the dehydroxylation of zeolites HY.* Chemical Physics Letters, 1983. **98**(3): p. 263-266.
- 114. Sayed, M.B., R.A. Kydd, and R.P. Cooney, *A Fourier-transform infrared spectral study of H-ZSM-5 surface sites and reactivity sequences in methanol conversion*. Journal of Catalysis, 1984. **88**(1): p. 137-149.
- 115. Fejes, P., I. Hannus, and I. Kiricsi, *Dealumination of zeolites with phosgene*. Zeolites, 1984. **4**(1): p. 73-76.
- 116. Woolery, G.L., et al., *Spectroscopic evidence for the presence of internal silanols in highly siliceous ZSM-5.* Zeolites, 1986. **6**(1): p. 14-16.
- 117. Dessau, R., On the presence of internal silanol groups in ZSM-5 and the annealing of these sites by steaming. Journal of Catalysis, 1987. **104**(2): p. 484-489.
- 118. Yamagishi, K., S. Namba, and T. Yashima, *Defect sites in highly siliceous HZSM-5 zeolites: a study performed by alumination and IR spectroscopy.* The Journal of Physical Chemistry, 1991. **95**(2): p. 872-877.
- 119. Brunauer, S., P.H. Emmett, and E. Teller, *Adsorption of Gases in Multimolecular Layers*. Journal of the American Chemical Society, 1938. **60**(2): p. 309-319.
- 120. Sinha, P., et al., *Surface Area Determination of Porous Materials Using the Brunauer–Emmett–Teller (BET) Method: Limitations and Improvements.* The Journal of Physical Chemistry C, 2019. **123**(33): p. 20195-20209.
- 121. Qin, Z., et al., *Opening the Cages of Faujasite-Type Zeolite.* Journal of the American Chemical Society, 2017. **139**(48): p. 17273-17276.
- 122. Wang, Y., et al., Effects of Dealumination and Desilication of Beta Zeolite on Catalytic Performance in n-Hexane Cracking. Catalysts, 2016. **6**(1): p. 8.
- 123. Bernasconi, S., *Liquid phase nitration of toluene and 2-nitrotoluene using acetyl nitrate: Zolite BEA as para-selective catalyst.* 2003, ETH Zurich.
- 124. Tišler, Z., et al., *Acid and Thermal Treatment of Alkali-Activated Zeolite Foams*. Minerals, 2019. **9**(12): p. 719.
- 125. Chen, N.Y. and F.A. Smith, *Preparation of dealuminized mordenite*. Inorganic Chemistry, 1976. **15**(2): p. 295-297.
- 126. Nagy, J.B., et al., *Aluminium distribution and cation location in various M-ZSM-5-type zeolites* (M Li, Na, K, Rb, Cs, NH4). Zeolites, 1988. **8**(3): p. 209-220.
- 127. Kraushaar, B., et al., *Clusters of Terminal Groups in ZSM-5: A Study Performed by Silylation and 29Si CP MAS NMR*, in *Studies in Surface Science and Catalysis*, P.J. Grobet, et al., Editors. 1988, Elsevier. p. 167-174.
- 128. Van Geem, P., et al., Study of the transformation of small-port into large-port mordenite by magic-angle spinning NMR and infrared spectroscopy. The Journal of Physical Chemistry, 1988. **92**(6): p. 1585-1589.
- 129. Barras, J., J. Klinowski, and D.W. McComb, *27Al and 29Si solid-state NMR studies of dealuminated mordenite*. Journal of the Chemical Society, Faraday Transactions, 1994. **90**(24): p. 3719-3723.
- 130. Siantar, D.P., W.S. Millman, and J.J. Fripiat, *Structural defects and cation exchange capacity in dealuminated Y zeolites*. Zeolites, 1995. **15**(6): p. 556-560.

- 131. Beyerlein, R.A., et al., *Effect of steaming on the defect structure and acid catalysis of protonated zeolites.* Topics in Catalysis, 1997. **4**(1): p. 27-42.
- 132. Artioli, G., C. Lamberti, and G.L. Marra, *Neutron powder diffraction study of orthorhombic and monoclinic defective silicalite.* Acta Crystallographica Section B, 2000. **56**(1): p. 2-10.
- 133. Zukal, A., V. Patzelová, and U. Lohse, *Secondary porous structure of dealuminated Y zeolites*. Zeolites, 1986. **6**(2): p. 133-136.
- 134. Burnett, R.L. and T.R. Hughes, *Mechanism and poisoning of the molecular redistribution reaction of alkanes with a dual-functional catalyst system.* Journal of Catalysis, 1973. **31**(1): p. 55-64.
- 135. Dobereiner, G.E. and R.H. Crabtree, *Dehydrogenation as a Substrate-Activating Strategy in Homogeneous Transition-Metal Catalysis*. Chemical Reviews, 2010. **110**(2): p. 681-703.
- 136. Fickel, D.W., et al., *INOR 79-Dehydrogenation of hydroxyl nest groups in silicalite-1.* Abstracts of Papers of the American Chemical Society, 2008. **236**: p. 1.
- 137. Isakov, D.R., G.M. Khrapkovskii, and A.G. Shamov, *Quantum-chemical study of methane dehydrogenation on neutral, cationic, and anionic clusters Pt2-5 by DFT method.* Russian Journal of General Chemistry, 2011. **81**(4): p. 781-782.
- 138. Fricke, C., et al., *Propane Dehydrogenation on Platinum Catalysts: Identifying the Active Sites through Bayesian Analysis*. ACS Catalysis, 2022. **12**(4): p. 2487-2498.
- 139. Chen, S., et al., *Propane dehydrogenation: catalyst development, new chemistry, and emerging technologies.* Chemical Society Reviews, 2021. **50**(5): p. 3315-3354.
- 140. Yang, F., et al., *Advanced design and development of catalysts in propane dehydrogenation.* Nanoscale, 2022. **14**(28): p. 9963-9988.
- 141. Boudart, M., et al., *On the selectivity of platinum catalysts.* Journal of Catalysis, 1968. **11**(1): p. 35-45.
- 142. Yang, Y., et al., *Carbon deposits during catalytic combustion of toluene on Pd–Pt-based catalysts*. Catalysis Science & Technology, 2020. **10**(8): p. 2452-2461.
- 143. Grasselli, R.K., *Advances and future trends in selective oxidation and ammoxidation catalysis.* Catalysis Today, 1999. **49**(1): p. 141-153.
- 144. Lin, Z., et al., Experimental and Theoretical Insights into the Active Sites on WOx/Pt(111) Surfaces for Dehydrogenation and Dehydration Reactions. ACS Catalysis, 2021. **11**(13): p. 8023-8032.
- 145. Paál, Z., Hydrocarbon product selectivity: a tool for characterizing the active state of platinum catalysts. Catalysis Today, 1988. **2**(5): p. 595-604.
- 146. Neugebauer, J. and T. Hickel, *Density functional theory in materials science*. WIREs Computational Molecular Science, 2013. **3**(5): p. 438-448.
- 147. Elbaz, Y., D. Furman, and M. Caspary Toroker, *Modeling Diffusion in Functional Materials:* From Density Functional Theory to Artificial Intelligence. Advanced Functional Materials, 2020. **30**(18): p. 1900778.
- 148. Senn, H.M. and W. Thiel, *QM/MM Methods for Biomolecular Systems*. Angewandte Chemie International Edition, 2009. **48**(7): p. 1198-1229.
- 149. Metz, S., et al., *ChemShell—a modular software package for QM/MM simulations.* WIREs Computational Molecular Science, 2014. **4**(2): p. 101-110.
- 150. Morzan, U.N., et al., *Spectroscopy in Complex Environments from QM–MM Simulations*. Chemical Reviews, 2018. **118**(7): p. 4071-4113.
- 151. Sherwood, P., et al., *QUASI: A general purpose implementation of the QM/MM approach and its application to problems in catalysis.* Journal of Molecular Structure: THEOCHEM, 2003. **632**(1): p. 1-28.
- 152. Nagy, B. and F. Jensen, *Basis Sets in Quantum Chemistry*, in *Reviews in Computational Chemistry*. 2017. p. 93-149.

- 153. Weigend, F. and R. Ahlrichs, *Balanced basis sets of split valence, triple zeta valence and quadruple zeta valence quality for H to Rn: Design and assessment of accuracy.* Physical Chemistry Chemical Physics, 2005. **7**(18): p. 3297-3305.
- 154. Kohn, W. and L. Sham. *Density functional theory*. in *Conference Proceedings-Italian Physical Society*. 1996. Editrice Compositori.
- 155. Becke, A.D., *A new mixing of Hartree–Fock and local density-functional theories.* The Journal of Chemical Physics, 1993. **98**(2): p. 1372-1377.
- 156. Mackerell Jr, A.D., *Empirical force fields for biological macromolecules: Overview and issues.* Journal of Computational Chemistry, 2004. **25**(13): p. 1584-1604.
- 157. Rappe, A.K., et al., *UFF, a full periodic table force field for molecular mechanics and molecular dynamics simulations.* Journal of the American Chemical Society, 1992. **114**(25): p. 10024-10035.
- 158. Harrison, R.L., *Introduction To Monte Carlo Simulation*. (0094-243X (Print)).
- 159. Hill, J.R. and J. Sauer, *MOLECULAR MECHANICS POTENTIAL FOR SILICA AND ZEOLITE CATALYSTS BASED ON AB-INITIO CALCULATIONS .2. ALUMINOSILICATES.* Journal of Physical Chemistry, 1995. **99**(23): p. 9536-9550.
- 160. Boulfelfel, S.E., et al., *Improved Hill–Sauer Force Field for Accurate Description of Pores in 8-Ring Zeolites*. The Journal of Physical Chemistry C, 2016. **120**(26): p. 14140-14148.
- 161. Woodley, S.M., Knowledge led master code search for atomic and electronic structures of LaF3 nanoclusters on hybrid rigid ion—shell model—DFT landscapes. The Journal of Physical Chemistry C, 2013. **117**(45): p. 24003-24014.
- 162. Sherwood, P., et al., *Computer simulation of zeolite structure and reactivity using embedded cluster methods.* Faraday Discussions, 1997. **106**(0): p. 79-92.
- 163. Gale, J.D. and A.L. Rohl, *The General Utility Lattice Program (GULP)*. Molecular Simulation, 2003. **29**(5): p. 291-341.
- 164. Hill, J.R. and J. Sauer, *Molecular mechanics potential for silica and zeolite catalysts based on ab initio calculations. 1. Dense and microporous silica.* The Journal of Physical Chemistry, 1994. **98**(4): p. 1238-1244.
- 165. Hill, J.-R. and J. Sauer, *Molecular Mechanics Potential for Silica and Zeolite Catalysts Based on ab Initio Calculations. 2. Aluminosilicates.* The Journal of Physical Chemistry, 1995. **99**(23): p. 9536-9550.
- 166. Broyden, C.G., *The Convergence of a Class of Double-rank Minimization Algorithms 1. General Considerations.* IMA Journal of Applied Mathematics, 1970. **6**(1): p. 76-90.
- 167. Fletcher, R., *A new approach to variable metric algorithms*. The Computer Journal, 1970. **13**(3): p. 317-322.
- 168. Goldfarb, D., *A family of variable-metric methods derived by variational means*. Mathematics of Computation, 1970. **94**(351): p. 23-26.
- 169. Shanno, D.F., *Conditioning of quasi-Newton methods for function minimization*. Mathematics of computation, 1970. **24**(111): p. 647-656.
- 170. Kästner, J., et al., Exploiting QM/MM Capabilities in Geometry Optimization: A Microiterative Approach Using Electrostatic Embedding. Journal of Chemical Theory and Computation, 2007. **3**(3): p. 1064-1072.
- 171. Kästner, J., et al., *DL-FIND: An Open-Source Geometry Optimizer for Atomistic Simulations*. The Journal of Physical Chemistry A, 2009. **113**(43): p. 11856-11865.
- 172. Smith, W., C.W. Yong, and P.M. Rodger, *DL_POLY: Application to molecular simulation*. Molecular Simulation, 2002. **28**(5): p. 385-471.
- 173. Valiev, M., et al., *NWChem: A comprehensive and scalable open-source solution for large scale molecular simulations.* Computer Physics Communications, 2010. **181**(9): p. 1477-1489.
- 174. Guest *, M.F., et al., *The GAMESS-UK electronic structure package: algorithms, developments and applications.* Molecular Physics, 2005. **103**(6-8): p. 719-747.

- 175. DeTar, D.F., *Molmec, a general approach to molecular mechanics computations.* Computers & Chemistry, 1977. **1**(3): p. 141-144.
- 176. Becke, A.D., *Density-functional thermochemistry. V. Systematic optimization of exchange-correlation functionals.* The Journal of Chemical Physics, 1997. **107**(20): p. 8554-8560.
- 177. Barrer, R.M. and M.B. Makki, *MOLECULAR SIEVE SORBENTS FROM CLINOPTILOLITE*. Canadian Journal of Chemistry, 1964. **42**(6): p. 1481-1487.
- 178. KLINOWSKI, J., *Solid-State NMR Studies of Molecular Sieve Catalysts.* Chemical reviews, 1991. **91**: p. 1459-1479.
- 179. Lin, J.S., et al., *Ab initio calculations on (OH)4 defects in* α -quartz. Physics and Chemistry of Minerals, 1994. **21**(3): p. 150-155.
- 180. Sokol, A.A., et al., Local States in Microporous Silica and Aluminum Silicate Materials. 1. Modeling Structure, Formation, and Transformation of Common Hydrogen Containing Defects. The Journal of Physical Chemistry B, 2002. **106**(24): p. 6163-6177.
- 181. Wang, Y. and J.P. Perdew, *Spin scaling of the electron-gas correlation energy in the high-density limit.* Physical Review B, 1991. **43**(11): p. 8911-8916.
- Sokol, A.A., et al., *Transformation of hydroxyl nests in microporous aluminosilicates upon annealing*. Journal of Physics-Condensed Matter, 2004. **16**(27): p. S2781-S2794.
- 183. Purton, J., et al., LDF pseudopotential calculations of the α -quartz structure and hydrogarnet defect. Physics and Chemistry of Minerals, 1992. **18**(6): p. 389-392.
- 184. Ryder, J.A., A.K. Chakraborty, and A.T. Bell, *Density Functional Theory Study of Proton Mobility in Zeolites: Proton Migration and Hydrogen Exchange in ZSM-5.* The Journal of Physical Chemistry B, 2000. **104**(30): p. 6998-7011.
- 185. Henkelman, G., B.P. Uberuaga, and H. Jónsson, *A climbing image nudged elastic band method for finding saddle points and minimum energy paths*. The Journal of Chemical Physics, 2000. **113**(22): p. 9901-9904.
- 186. Abdul Nasir, J., et al., *Influence of Solvent on Selective Catalytic Reduction of Nitrogen Oxides with Ammonia over Cu-CHA Zeolite*. Journal of the American Chemical Society, 2023. **145**(1): p. 247-259.
- 187. Nastase, S.A.F., et al., *Computational QM/MM investigation of the adsorption of MTH active species in H-Y and H-ZSM-5*. Physical Chemistry Chemical Physics, 2019. **21**(5): p. 2639-2650.
- 188. Choi, M., et al., *Stable single-unit-cell nanosheets of zeolite MFI as active and long-lived catalysts*. Nature, 2009. **461**(7261): p. 246-U120.
- 189. Lazauskas, T., A.A. Sokol, and S.M. Woodley, *An efficient genetic algorithm for structure prediction at the nanoscale*. Nanoscale, 2017. **9**(11): p. 3850-3864.
- 190. Woodley, S.M. and R. Catlow, *Crystal structure prediction from first principles*. Nature Materials, 2008. **7**(12): p. 937-946.
- 191. Cleri, F. and V. Rosato, *Tight-binding potentials for transition metals and alloys*. Physical Review B, 1993. **48**(1): p. 22-33.
- 192. Blum, V., et al., *Ab initio molecular simulations with numeric atom-centered orbitals.* Computer Physics Communications, 2009. **180**(11): p. 2175-2196.
- 193. Perdew, J.P., et al., *Restoring the density-gradient expansion for exchange in solids and surfaces.* Physical review letters, 2008. **100**(13): p. 136406.
- 194. Day, A.K.C.a.P., Solid State Chemistry. Vol. 1. 1990, A Clarendon Press Publication.

Appendices

This section presents the appendices, which compile supplementary materials to support and enhance the understanding of the thesis. These include details on resource requirements, job calculations, experimental analyses, computational inputs, and other relevant information that complements the main body of work

A.1 Resource Requirements

Table A1: ARCHER CU calculated cost per job

Job Type	No. of Cores	Wallclock time (hours)	No. of jobs	CU per Job
Single point	124	1	~60	4
Geom. Opt.	248	48	~200	96

Table A2. Estimated total ARCHER2 CU calculated cost.

Type of Calculations	Average CU cost	Materials
Single Points	4	ZSSM-5/CHA/FAU/α-Quartz
Geometry Optimisations	96	ZSSM-5/CHA/FAU/α-Quartz
NEB calculations	17280	ZSSM-5/CHA/FAU/α-Quartz
Vibrational Calculations	56	ZSSM-5/CHA/FAU/α-Quartz

Table A3. Estimated total ARCHER2 MU calculated cost.

Type of Calculations	MAU cost	Materials
Geometry Optimisations	20	ZSSM-5/CHA/FAU/α-Quartz
Vibrational Calculations	15	ZSSM-5/CHA/FAU/α-Quartz
Nudge Elastic Band Calculations	45	ZSSM-5/CHA/FAU/α-Quartz

Job Data

Table A4. Memory requirements for various jobs on ARCHER2 machine.

Description	Largest Job	Typical Job	Smallest Job
Total memory required (per job)	1536 GiB	768 GiB	256 GiB
Total time for these jobs (hours)	960	1200	40

The disk space is typically contained within \sim 1-4 GB per single job, and we expect to require about 1000 GB of the workspace. With NEB calculations running a far larger disk space at 10+ GB per job.

A.2 Computational Input files

All Files can be obtained on Nomad with the following links:

ZSM5: fLtSoEMBQiie15RRsdk2ow

CHA: 0xCSOtd2Qmm2 yT8BL8UZQ

Alpha-quartz: tT0Hk8NXT1yLVeaycgg8ZQ

Python ChemShell with NWCHEM with GULP

Example for ZSM-5 cluster

from chemsh import *
from chemsh.utils import testutils
HEAP=1000
STACK=1000
GLOBAL=2000

inputfrag = Fragment(coords='ring_HN_2.pun', connect_mode='covalent')

```
#silicate modifiers = {('Si','O1'):0.3, ('Si','O11'):0.3}T
active_atoms = inputfrag.getRegion()
print("Active Atoms: ", active atoms)
radius active = 36.0
origin = [1.61462365734421e+01, 2.36244745756702e+00, 1.74013684568988e+01]
active_region = inputfrag.selectByRadius(radius_active,centre=origin)
qm region = inputfrag.getRegion(1, 11)
print("QM region is: ", qm_region)
qm_charge = int(inputfrag.totalcharge)
print("QM charge is: ", qm charge)
qm_theory = NWChem(method
                               = 'dft',
       functional = 'becke97-2',
       memory = 4000,
       basis
               = 'basis',
               = 1,
       mult
       scftype = 'uhf',
       charge = qm_charge,
       harmonic = True,
       direct = True,
       maxiter = 999,
       tol energy = 1.E-6,
       tol_density = 1.E-5,
       tol gradient = 1.E-5,
       restart=True)
mm theory = GULP(ff ='zeolite.ff',
       molecule = True)
gmmm = QMMM(gm=gm theory,
       mm=mm_theory,
       frag=inputfrag,
       coupling='covalent',
       embedding='electrostatic',
       bond_modifiers=silicate_modifiers,
       dipole adjust=True,
       qm_region=qm_region)
opt = Opt(theory=qmmm,
       algorithm="lbfgs",
       maxcycle=500,
       maxene=500,
       dump=1,
       active=active_region,
```

Gamess-UK with DL-POLY (TCL-Chemshell)

Example of CHA cluster

```
#write_xyz coords=Cha_QMMM_TCS.pun file=Cha_sp_in.xyz
set conv {
{newscf}
{maxcyc 150}
{print full}
{Phase 1}
{ Level 10.0 10.0 }
{ DIIS }
{# Switch to phase 2}
{ next 2}
{ Tester below 0.01}
{Phase 2}
{ Level 0.5 0.5 }
{ DIIS }
{# Switch to phase 3}
{ next 3}
{ Tester below 0.001}
{Phase 3}
{ Level 0.0 0.0 }
{ DIIS }
{ next 0}
{# Converge calculation}
{ Tester below 0.000001}
{# Absolute energy change}
{ dEabs below 0.0000001 }
{end}
}
set dl_poly_args " mm_defs= zeolite.ff mxexcl=200 "
set gamess_args " basisfile= basis \
            functional=b97-2 \
            harmonic=yes \
            unique_listing=no \
            scf_keywords = [ list $conv ] \
```

```
direct=yes \
            echo input=no print bqs=no \
            symmetry=off \
            charge=0 \
            scftype=uhf \
            mult=1 \
            memory=99000000 "
             restart=yes "
             guessfile=guess.txt "
#
             scf_thresh=5 \
set hybrid args "qm region={ atom list} \
          mm_theory = dl_poly : [ list $dl_poly_args ] \
          qm_theory = gamess : [list $gamess_args ] \
          coupling=shift \
          dipole_adjust=yes "
#eandg energy=e \
    coords=cha_1T.pun \
    theory=hybrid : [ list $hybrid_args ]
dl-find coords=cha_1T.pun \
   maxcycle=500 \
   theory=hybrid : [ list $hybrid_args ] \
   dump=1 \
   result=cha_1T_opt.pun \
   active_atoms= { atom_list } \
   tolerance=0.001
   restart=yes
#write_xyz coords=silica_sp.pun file=silica_sp_out.xyz
```

QM/MM basis set

The dual basis set is based on the Def2-TZVP and Def2-SVP basis sets (see Chapter 2.3.1).

```
basis spherical
#BASIS SET: (5s,1p) -> [3s,1p]
H11 S
34.0613410 0.60251978E-02
5.1235746 0.45021094E-01
1.1646626 0.20189726
H11 S
0.32723041 1.0000000
H11 S
```

0.10307241 1.0000000 H11 P 0.8000000 1.0000000 #BASIS SET: (11s,6p,2d,1f) -> [5s,3p,2d,1f] 011 S 27032.3826310 0.21726302465E-03 4052.3871392 0.16838662199E-02 922.32722710 0.87395616265E-02 261.24070989 0.35239968808E-01 85.354641351 0.11153519115 31.035035245 0.25588953961 O11 S 12.260860728 0.39768730901 4.9987076005 0.24627849430 011 S 1.1703108158 1.0000000 011 S 0.46474740994 1.0000000 011 S 0.18504536357 1.0000000 O11 P 63.274954801 0.60685103418E-02 14.627049379 0.41912575824E-01 4.4501223456 0.16153841088 1.5275799647 0.35706951311 O11 P 0.52935117943 .44794207502 011 P 0.17478421270 .24446069663 011 D 2.31400000 1.0000000 011 D 0.64500000 1.0000000 011 F 1.42800000 1.0000000 #BASIS SET: (14s,9p,3d,1f) -> [5s,5p,2d,1f] Si11 S 44773.3580780 0.55914765868E-03 6717.1992104 0.43206040189E-02 1528.8960325 0.22187096460E-01 432.54746585 0.86489249116E-01 140.61505226 0.24939889716 49.857636724 0.46017197366 18.434974885 0.34250236575 Si11 S 86.533886111 0.21300063007E-01 26.624606846 0.94676139318E-01

4.4953057159

-0.32616264859

```
Si11 S
  2.1035045710
                    1.3980803850
  1.0106094922
                    0.63865786699
Si11 S
  0.23701751489
                    1.0000000
Si11 S
  0.85703405362E-01
                      1.0000000
Si11 P
 394.47503628
                    0.26285693959E-02
  93.137683104
                    0.20556257749E-01
  29.519608742
                    0.92070262801E-01
  10.781663791
                    0.25565889739
  4.1626574778
                    0.42111707185
Si11 P
  1.6247972989
                    .34401746318
Si11 P
  0.54306660493
                    1.0000000
Si11 P
  0.20582073956
                    1.0000000
Si11 P
  0.70053487306E-01
                      1.0000000
Si11 D
  2.30300000
                   0.20000000
  0.476000000
                   1.00000000
Si11 D
  0.160000000
                   1.0000000
Si11 F
  0.336000000
                   1.0000000
#BASIS SET: (4s,1p) -> [2s,1p]
H1 S
  13.0107010
                   0.19682158E-01
  1.9622572
                  0.13796524
  0.44453796
                   0.47831935
H1 S
  0.12194962
                   1.0000000
H1 P
  0.8000000
                  1.0000000
#BASIS SET: (7s,4p,1d) -> [3s,2p,1d]
01 S
 2266.1767785
                   -0.53431809926E-02
 340.87010191
                   -0.39890039230E-01
                   -0.17853911985
  77.363135167
  21.479644940
                   -0.46427684959
                   -0.44309745172
  6.6589433124
01 S
  0.80975975668
                    1.0000000
O1 S
  0.25530772234
```

1.0000000

```
01 P
  17.721504317
                    0.43394573193E-01
  3.8635505440
                    0.23094120765
  1.0480920883
                    0.51375311064
01 P
  0.27641544411
                     1.0000000
01 D
   1.2000000
                  1.0000000
#BASIS SET: (10s,7p,1d) -> [4s,3p,1d]
Si1 S
 6903.7118686
                    0.13373962995E-02
 1038.4346419
                    0.99966546241E-02
 235.87581480
                    0.44910165101E-01
  66.069385169
                    0.11463638540
  20.247945761
                    0.10280063858
Si1 S
  34.353481730
                    0.70837285010E-01
  3.6370788192
                    -0.43028836252
  1.4002048599
                    -0.41382774969
Si1 S
  0.20484414805
                     1.0000000
Si1 S
  0.77994095468E-01
                       1.0000000
Si1 P
  179.83907373
                    0.61916656462E-02
  41.907258846
                    0.43399431982E-01
  12.955294367
                    0.15632019351
  4.4383267393
                    0.29419996982
  1.5462247904
                    0.23536823814
Si1 P
  0.35607612302
                     1.0000000
Si1 P
  0.10008513762
                     1.0000000
Si1 D
  0.3500000
                  1.0000000
END
```

QM/MM forcefield for Py-ChemShell

The FF in this file was implemented by Sophia Proud and Samuel Watts, under the guidance of Andrew Logsdail, in 2018.

We are grateful to both the Cardiff University CUROP scheme and a CCP5 Summer Bursary for their support

#Modification to FF in this file was implemented by Alec Desmoutier, under the guidance to Richard Catlow and Alexey Sokol, in 2021.

We are grateful to UCL and the MCC consortium for their support.

The FF was taken from the work of Hill and Sauer, J. Phys. Chem. 99 (1995) 9536-9550

#

```
keyword molmec
rtol 1.1
element
covalent 90
harmonic k3 k4 bond kcal
# Two-body harmonic term. Input structure: k2 k3 k4 r0 coul rmin rmax
# k2 is calculated as: 459.0786*2
# k3 is calculated as:-672.4445*6
# k4 is calculated as: 443.3651*24
Si O 918.1572 -4034.6670 10640.7624 1.6104
three k3 k4 bond kcal
# Three-body term. Input structure: k2 k3 k4 theta0 rmax(1-2) rmax(1-3) rmax(2-3)
# k2(H2) is calculated as 81.9691*2
# k3(H3) is calculated as -36.5814*6
# k4 (H4) is calculated as 116.9558*24
Si O O 163.9382 -219.4884 2806.9392 112.0200
O Si Si 41.4030 165.3036 263.8320 173.7651
bacross bond kcal
# Bond-angle cross term. Input structure: k1 k2 r1 r2 theta0 rmax12 rmax13 rmax23
according to online GULP help manual
# In the 1995 paper, and from DL Poly documentation, there are two constants, Fba and Fba'.
# As pointed out by Jingcheng Guan (UCL), these are to ensure environmental symmetry in
the bonding species
#
Si O O 78.1239 78.1239 1.6104 1.6104 112.0200
O Si Si 9.2390 9.2390 1.6104 1.6104 173.7651
bcross bond kcal
# Bond-bond cross term (3-body). Input structure: K r1 r2 rmax12 rmax13 rmax23
Si O O 0.0000 1.6104 1.6104
# assumed for K in above line of O-Si-O to be equal to zero as not mentioned in the 1995
O Si Si 151.8742 1.6104 1.6104
uff4 bond kcal
# Torisonal UFF potential. Input structure: k n rmax(1-2) rmax(2-3) rmax(3-4) rmax(4-1)
```

```
# Whilst implemented in the original FF, this term seems to have no effect in DL_POLY and
# so is disabled here for directly compatibility with the previous DL POLY implementation of
FF.
#
## k calculated as: 2*0.0306(V1)
Si O Si O 0.0612 1.0000
## k calculated as: 2*-0.0105(V2)
Si O Si O -0.0210 2.0000
## k calculated as: 2*0.0804(V3)
Si O Si O 0.1608 3.0000
xangleangle bond kcal
# Angle-angle cross potential. Input structure A B C D k(213/4) k(312/4) k(412/3) theta0(213)
theta0(214) theta0(314) rmax(1-2) rmax(1-3) rmax(1-4)
Si O O O -6.3030 -6.3030 -6.3030 112.0200 112.0200 112.0200
torangle bond kcal
# Torsional-angle cross term. Input structure: A B C D K theta0 theta0' rmax(1-2) rmax(2-3)
rmax(3-4)
O Si O Si -4.5150 112.0200 173.7651
lennard 9 6 x13 kcal
# Lennard-Jones long-range VDW-type interaction. Input Structure: A B rmin rmax
# Represents second term in equation stated in the research paper
# A calculated as A(Si)*A(O): 432.3320*239.6090
#
Si O 103590.638188 0.0 0.0000 60.0000
Si Si 186910.958224 0.0 0.0000 60.0000
O O 57412.472881 0.0 0.0000 60.0000
```

Example input for genetic algorithm calculations

```
#
#Keywords
#
opti conp
#
title
Pt Clusters
end
#
#Option words
```

Н

######## Pt-Pt potentials
buckingham
atom1 atom2 2*(A*e^p) 1/(p/r0) C
Pt core Pt core 24168.51729 0.2408774043 0.0 0.0 12.0 0 0 0
manybody
atom1 atom2 rmin rmax
Pt core Cu core 0.0 12.0
eam_functional square_root
Pt core 1
eam_density baskes
atom1 atom2 zeta^2 2q r0

Pt core Pt core 7.263025 8.008 2.5561910139893693 0 0 0